

Measurements of Higgs boson properties in proton-proton collisions at $\sqrt{s}=7, 8$ and 13 TeV at the CERN Large Hadron Collider

by

Ulascan Sarica

**A dissertation submitted to The Johns Hopkins University
in conformity with the requirements for the degree of
Doctor of Philosophy**

Baltimore, Maryland

October, 2018

© 2018 by Ulascan Sarica

All rights reserved



Abstract

Studies of production and decay of the spin-0 Higgs boson are described. In particular, anomalous couplings of the Higgs boson to two electroweak gauge bosons are studied from on-shell Higgs boson production with decay to 4ℓ and $WW \rightarrow \ell\nu\ell\nu$ using the Run 1 data collected by the CMS detector. The constraints and techniques are improved in the Run 2 on-shell analysis of the 4ℓ decay channel. Events from Run 1 are also analyzed for the 4ℓ vertex information to constrain the Higgs boson lifetime from above and thereby the Higgs boson total width from below. The width is constrained further by employing the off-shell technique in the 4ℓ decay channel. These constraints are placed using events from both Run 1 and Run 2 datasets. Assumptions on the tensor structure of the resonance and the invariant mass lineshape are relaxed by placing joint constraints with different anomalous couplings. The SM-like total width analysis is also used to place approximate joint constraints on the Higgs boson mass and width, and preliminary constraints on the value of Higgs boson mass with the value of the total width unconstrained in the fit. No significant deviation from the Standard Model is found in the analyzed anomalous couplings or in the total width, and a preliminary value of Higgs boson mass from the combined Run 1 and Run 2 dataset is provided.

Thesis Committee

Andrei V. Gritsan (Advisor)

Professor

Department of Physics and Astronomy

Johns Hopkins Zanvyl Krieger School of Arts and Sciences

Morris Swartz

Professor

Department of Physics and Astronomy

Johns Hopkins Zanvyl Krieger School of Arts and Sciences

Ibrahima Bah

Assistant Professor

Department of Physics and Astronomy

Johns Hopkins Zanvyl Krieger School of Arts and Sciences

W. Stephen Wilson

Professor

Department of Mathematics

Johns Hopkins Zanvyl Krieger School of Arts and Sciences

Tamas Budavari

Assistant Professor

Department of Applied Mathematics and Statistics

Johns Hopkins Whiting School of Engineering

Acknowledgments

This thesis has used results from the CMS Experiment at the LHC, so I thank all the LHC personnel for maintaining and improving the collider, and many known, and unknown, scientists in CMS who make the different details leading to my analyses possible.

The thesis has been the culmination of work done over more than six years to ensure top quality Higgs properties measurements and has been built on the expertise developed by previous Ph.D. students and postdoctoral fellows. Therefore, I thank Markus Schulze, Yanyan Gao, Sara Bolognesi, Nhan Tran, Andrew Whitbeck and Ian Anderson, whose enormous effort is felt at every step from the JHUGEN simulation to actual CMS data analysis. In this context, I also thank Kirill Melnikov for assisting the writing of this simulation that remains as a very useful tool several years after its original conception.

The computational work on this thesis would not have been possible without the computing centers and personnel of the Worldwide LHC Computing Grid, and the Maryland Advanced Research Computing Center (MARCC). I also thank the National Science Foundation (NSF) for providing their continuous financial support, and to Dr. William Gardner for their enthusiastic support of my research in the spring and summer of 2015.

Special thanks to the Physics and Astronomy administration, Kelley Key, Pamela McCullough, Norma Berry and Brian Schriver, who have played key roles in organization to ensure efficient operation; to Nicholas (Nick) Emnizer, whose dedication to teaching has truly fascinated me; to Kimberly (Kim) Berghaus, whose curiosity in and excitement for new physics has been inspiring, and to Meng Xiao, whose intelligence and practicality in physics analyses are admirable. Many thanks to the members of my thesis committee for the time they spent in ensuring that the thesis material is solid and thorough, especially to Morris Swartz, who helped me understand some of the interesting challenges in the tracker as an expert in addition to being a member of my committee.

To my colleagues in the CMS Joint Four-Lepton Study Team, the analyses presented here would not have been possible without your continuous attention on the analysis framework and the physics objects. To Jeffrey (Heshy) Roskes, there is no way many of these results would be possible if we had not complemented each other in making our projects a reality; it has been a pleasure to work with you. To my supervisor, Andrei V. Gritsan, you are a phenomenal advisor; the differences of opinion we may have had about or outside of physics cannot change this fact.

Table of Contents

Table of Contents	vi
List of Tables	ix
List of Figures	xi
1 The Standard Model and the Higgs Boson at the LHC	1
1.1 Fundamental interactions in the Electroweak Theory	2
1.2 Fundamental interactions in Quantum Chromodynamics . . .	8
1.3 Spontaneous symmetry breaking and the Higgs mechanism .	10
1.4 The Yukawa mechanism for fermion masses	12
2 The CERN Large Hadron Collider and the Compact Muon Solenoid Detector	14
2.1 Design and specifications of the LHC	15
2.2 Design and specifications of the CMS detector	17
2.2.1 The inner tracker	19
2.2.1.1 Phase-0 pixel detector	22

2.2.1.2	Phase-1 pixel detector	26
2.2.1.3	Strip detector	28
2.2.2	Alignment of the tracker	28
2.2.3	The electromagnetic calorimeter and the preshower . .	41
2.2.4	The hadronic calorimeter	43
2.2.5	The muon system	44
2.3	The trigger system	46
2.4	Identification of particles and $H \rightarrow 4\ell$ event candidates	49
2.4.1	Identification of physics objects using the particle-flow algorithm	49
2.4.2	$H \rightarrow 4\ell$ candidate selection	53
3	The Phenomenology of the Higgs Boson at the LHC	60
3.1	The couplings of a spin-0 resonance	62
3.2	Standard Model Higgs boson production and decay at the LHC	66
3.3	Simulation and analysis tools for the Higgs boson	70
3.3.1	Simulation tools	71
3.3.2	Kinematic discriminants	74
3.4	The off-shell technique to measure the width and anomalous couplings	78
4	Analysis of the Higgs boson properties during Run I and Run II of the LHC	84

4.1	Analysis of anomalous HVV couplings from on-shell Higgs boson production	84
4.1.1	Run 1 analysis strategy	85
4.1.2	Run 2 analysis strategy	86
4.1.3	Results from the combined Run 1 and Run 2 analysis .	93
4.1.4	Additional results using only Run 1 events	96
4.2	Lifetime analysis from on-shell Higgs boson production	102
4.3	Width and spin-parity analysis combining off-shell events . .	109
4.3.1	On-shell parameterization in the combined width and spin-parity analysis	109
4.3.2	Off-shell parameterization in the combined width and spin-parity analysis	114
4.3.3	Results of the Run 1 analysis	117
4.3.4	Results of the Run 2 analysis	119
4.4	Width and spin-parity projections for the HL-LHC	125
4.5	Joint constraints on the mass and width of the Higgs boson . .	127
5	Summary and outlook	132

List of Tables

2.1	Comparison of ROC specifications in the Phase-0 and Phase-1 pixel detectors	26
3.1	Cross section ratios of anomalous HVV contributions for on-shell $H \rightarrow 2e2\mu$ events	66
4.1	Observables used in Run 1 anomalous HVV couplings analysis	89
4.2	Observables used in the on-shell region for the Run 2 width and anomalous HVV couplings analysis	91
4.3	Summary of anomalous HVV couplings constraints from on-shell Higgs boson production in Run 1 and Run 2	93
4.4	Summary of anomalous HVV coupling constraints from on-shell Higgs boson production obtained only from Run 1	96
4.5	Observables used in the off-shell region for the Run 2 width and anomalous HVV couplings analysis	115
4.6	Summary of $f_{ai} \cos(\phi_{ai})$ constraints from the combined Run 1 and Run 2 off-shell width analysis	119

4.7	Summary of constraints on Γ_H from the combined Run 1 and Run 2 off-shell analysis	122
4.8	Summary of constraints on $\mu_i^{\text{off-shell}}$ from the combined Run 1 and Run 2 off-shell width analysis	123
4.9	Summary of constraints on $f_{a3} \cos(\phi_{a3})$ and Γ_H predicted for HL-LHC runs	126

List of Figures

2.1	The LHC complex	16
2.2	Representation of the CMS detector during Run 1	18
2.3	CMS tracker during Phase-0 and Phase-1	21
2.4	Phase-0 BPIX support structures	22
2.5	Phase-0 FPIX support structures	24
2.6	Hit efficiency of the Phase-0 pixel detector	25
2.7	General overview of tracker alignment workflow	30
2.8	Typical track-hit residuals applied in tracker alignment	31
2.9	Misalignment of the tracker in 2016	34
2.10	Distribution of the median of residuals for the pixel barrel and strip endcaps	36
2.11	Distributions of cosmic muon momentum coordinates	36
2.12	Validation of track parameters using data from cosmics	37
2.13	Primary vertex validation of tracker alignment in 2016	38
2.14	Validation of tracker alignment from $Z \rightarrow \mu\mu$ events in 2017	40
2.15	Time dependence of ECAL relative energy response	42

2.16	CMS L1 trigger scheme	47
2.17	$m_{4\ell}$ distributions of observed 4ℓ events in Run 1 and Run 2 . .	54
3.1	Dominant H boson production mechanisms	67
3.2	H boson production cross sections at $\sqrt{s} = 8$ and 13 TeV . . .	68
3.3	ggH NLO and NNLO QCD K factors for $\sqrt{s} = 8$ TeV and 13 TeV	69
3.4	H boson total decay width and branching ratios	70
3.5	QCD and EW K factors for the $q\bar{q} \rightarrow ZZ$ process at 13 TeV . .	74
3.6	Kinematic diagrams of $H \rightarrow VV \rightarrow 4f$ processes	75
3.7	Kinematic variables in $H \rightarrow VV \rightarrow 4f$ processes	76
3.8	Off-shell $gg \rightarrow 2l2l'$ lineshape with different HZZ couplings .	81
3.9	Off-shell $gg \rightarrow 2l2l'$ lineshape with different ggH couplings .	83
4.1	Distributions of $ZZ \rightarrow 4\ell$ observables in the Run 1 anomalous couplings analysis	87
4.2	Distributions of $WW \rightarrow 2\ell 2\nu$ observables in the Run 1 anoma- lous couplings analysis	88
4.3	Distributions of 4ℓ observables in the Run 2 on-shell anomalous HVV couplings analysis	92
4.4	Anomalous HVV coupling constraints from on-shell Higgs bo- son production in Run 1 and Run 2	95
4.5	Anomalous $HZ\gamma$ and $H\gamma\gamma$ coupling constraints from on-shell 4ℓ events from Run 1	98

4.6	One-parameter likelihood scans in $f_{ai} \cos(\phi_{ai})$ conditional on R_{ai} from Run 1 on-shell Higgs boson production events	99
4.7	Run 1 anomalous HVV coupling constraints from on-shell ZZ and WW events	100
4.8	Likelihood scans of f_{ai} with ϕ_{ai} unconstrained from Run 1 on-shell Higgs boson production events	100
4.9	Two-parameter likelihood scans in terms of two different $f_{ai} \cos(\phi_{ai})$ from Run 1 on-shell Higgs boson production events	101
4.10	Higgs boson lifetime measurement observables	105
4.11	Constraints on the lifetime of the Higgs boson	107
4.12	Extreme variations of Higgs boson observed lifetime resolution	108
4.13	Scale and resolution uncertainties derived from dilepton resonances	112
4.14	Comparison of predicted and measured relative per-event mass errors in $Z \rightarrow 2\ell$ decay	113
4.15	Distributions of 4ℓ observables in the Run 2 off-shell analyses	116
4.16	Two-parameter constraints on Γ_H and $f_{\Lambda Q} \cos \phi_{\Lambda Q}$ from the Run 1 off-shell width analysis	118
4.17	One-parameter constraints on Γ_H or $f_{\Lambda Q} \cos \phi_{\Lambda Q}$ from the Run 1 off-shell width analysis	118
4.18	Constraints on $f_{ai} \cos(\phi_{ai})$ under different Γ_H assumptions from the combined Run 1 and Run 2 off-shell analysis	121

4.19 Constraints on Γ_H from the combined Run 1 and Run 2 off-shell analysis	122
4.20 Constraints on $\mu_i^{\text{off-shell}}$ from the combined Run 1 and Run 2 off-shell analysis	124
4.21 HL-LHC projections on $f_{a3} \cos(\phi_{a3})$ and Γ_H from 2016 simulation at 13 TeV	126
4.22 Joint constraints on m_H and Γ_H using on-shell events in the 2016 dataset	128
4.23 Preliminary joint constraints on m_H and Γ_H using on-shell and off-shell events from the combined Run 1 and Run 2 dataset .	130
4.24 Preliminary constraints on m_H from the combined Run 1 and Run 2 dataset	131

Chapter 1

The Standard Model and the Higgs Boson at the LHC

Particle physics is the branch of physics that studies the different fundamental particles in nature and how one type interacts with another. There are two classes of these particles based on their spin: Fermions and bosons. Fermions have an odd-integer multiple of $\frac{1}{2}$ spin and obey Fermi-Dirac statistics, and by the Fermi Exclusion Principle, two different fermions cannot occupy the same quantum state. Almost all of the ordinary objects with which humans interact are composed of fermions. Ignoring finer distinctions for the moment, only 12 elementary fermions are known, 6 leptons and 6 quarks, each of which can be subdivided into 3 generations with similar properties. Bosons, on the other hand, have an even-integer spin and obey Bose-Einstein statistics. Elementary bosons act as mediators between fermions and are the main carriers of force in interaction, which could be either strong, weak, electromagnetic or gravitational.

The Standard Model (SM) of particle physics [1–5] is a theory of strong,

weak and electromagnetic interactions with an underlying gauge symmetry group $SU(3)_C \otimes SU(2)_L \otimes U(1)_Y$. The $SU(2)_L \otimes U(1)_Y$ stands for the electroweak interactions mediated by the massive bosons W , Z , and electromagnetic interactions mediated by the massless photon, γ , described by Quantum Electrodynamics (QED). The $SU(3)_C$ component stands for the symmetry structure governing strong interactions mediated by massless gluons of 8 different color charges described by Quantum Chromodynamics (QCD). We give a more detailed discussion of the electroweak interactions in Section 1.1 followed by a discussion of the QCD interactions in Section 1.2. In the SM, the massive electroweak mediators, W^+ , W^- and Z bosons, acquire their mass through the mechanism of Electroweak Spontaneous Symmetry Breaking (EWSB) [6–12]. This essential mechanism introduces a complex scalar field with four degrees of freedom, three of which lead to the W^\pm and Z bosons acquiring mass while the fourth gives rise to a physical particle, the scalar Higgs boson H . We discuss the mechanism of spontaneous symmetry breaking in more detail in Section 1.3. We also discuss for completeness in Section 1.4 the Yukawa mechanism for how fermions acquire their masses through the scalar Higgs field [13, 14].

1.1 Fundamental interactions in the Electroweak Theory

As mentioned earlier, Quantum Electrodynamics is the theory of interactions under electromagnetic forces, and its discussion is pedagogically useful before digesting the full electroweak theory. In order to describe the interactions in

detail, we start with the Dirac equation for a free fermion of spin $\frac{1}{2}$

$$(i\gamma^\mu\partial_\mu - m)\psi(\mathbf{x}) = 0, \quad (1.1)$$

where $\psi(\mathbf{x})$ is a spinor with 4 components, γ^μ are the Dirac matrices corresponding to space-time coordinates x^μ ($\mu = 0, 1, 2, 3$), and m is the mass of the fermion, understood to be multiplied by a 4×4 unit matrix in Eqn. 1.1. The Lagrangian that corresponds to the free Dirac particle can be written as

$$\mathcal{L}_D = \bar{\psi}(\mathbf{x}) (i\gamma^\mu\partial_\mu - m)\psi(\mathbf{x}). \quad (1.2)$$

Before writing the full Lagrangian for the electromagnetic interactions, we also write Maxwell's equations under no external currents,

$$\partial^\mu F_{\mu\nu} = 0 \quad (1.3)$$

where $F_{\mu\nu} = \partial_\mu A_\nu - \partial_\nu A_\mu$ is the antisymmetric field tensor for the electromagnetic field $A^\mu(\mathbf{x})$. The free field Lagrangian that corresponds to Eqn. 1.3 is

$$\mathcal{L}_A = -\frac{1}{4}F^{\mu\nu}F_{\mu\nu}. \quad (1.4)$$

The Lagrangians 1.2 and 1.4 obey local $U(1)$ symmetry when $\psi(\mathbf{x}) \rightarrow e^{iqe\theta(\mathbf{x})}\psi(\mathbf{x})$, $A_\mu \rightarrow A_\mu - \frac{1}{qe}\partial_\mu\theta(\mathbf{x})$, and the derivative operator ∂_μ in Eqn. 1.2 is replaced with the covariant derivative $\partial_\mu \rightarrow \nabla_\mu = \partial_\mu - iqeA_\mu$. The replacement of the partial derivative with the covariant derivative in general introduces interaction terms in a Lagrangian between the different fields, and in this case, the additional term added by this replacement gives the

electromagnetic interaction Lagrangian

$$\mathcal{L}_{EM} = qe\bar{\psi}(\mathbf{x})A_\mu\gamma^\mu\psi(\mathbf{x}). \quad (1.5)$$

The scalar q is interpreted as the signed charge of the fermion in units of electron charge magnitude e (e.g. the charge of an electron is $q_e = -1 \cdot e$).

The decay of second and third generation leptons, or any other interaction that involves an electromagnetic charge exchange proceeds via weak interactions. These interactions may not behave in the same way under the inversion of charge-parity (CP), or parity alone (P). One manifestation of the parity violation is that experimentally, right-handed neutrinos have not been observed [15]. Taking the experimental input into account, we group each left-handed neutrino and lepton, or an up and down quark within a single generation into a doublet, and the different right-handed charged leptons and quarks into singlets:

$$\psi_L = \begin{pmatrix} \nu \\ l^- \end{pmatrix}_L, \begin{pmatrix} q_u \\ q_d \end{pmatrix}_L \quad (1.6)$$

$$\psi_R = l_R^-, q_{u,R}, q_{d,R} \quad (1.7)$$

The free particle Lagrangian takes a similar form to Eqn. 1.2:

$$\mathcal{L}_{D,W} = i\bar{\psi}_R\gamma^\mu\partial_\mu\psi_R + i\bar{\psi}_L\gamma^\mu\partial_\mu\psi_L - m(\bar{\psi}_R\psi_L + \bar{\psi}_L\psi_R). \quad (1.8)$$

This Lagrangian is not invariant under an $SU(2)$ transformation. Therefore, by analogy to electromagnetic interactions, we introduce a single field B_μ for the abelian $U(1)$ group and 3 more fields $\vec{W}_\mu = (W_\mu^1, W_\mu^2, W_\mu^3)$ for the non-abelian $SU(2)$ group. We also define g to be a coupling strength corresponding

to interactions via \vec{W} , and g' to be a coupling strength corresponding to interactions via B . The resultant field Lagrangian becomes

$$\mathcal{L}_{B,W} = -\frac{1}{4}B^{\mu\nu}B_{\mu\nu} - \frac{1}{4}W^{i,\mu\nu}W_{\mu\nu}^i, \quad (1.9)$$

where summation $B_{\mu\nu}$ has the same form as $F_{\mu\nu}$ before, $W_{\mu\nu}^i = \partial_\mu W_\nu^i - \partial_\nu W_\mu^i - g\epsilon_{ijk}W_\mu^j W_\nu^k$ is the non-abelian counterpart with the anti-symmetric Levi-Civita tensor ϵ_{ijk} , and summation over the indices j and k is implied. We note here that Eqn. 1.9 features product terms that scale with $g\epsilon_{ijk}$, which implies all three W^i interact in a 3- or 4-boson vertices.

If the free particle Lagrangian 1.8 is invariant under an $SU(2)_L \otimes U(1)_Y$ transformation, the Lagrangian should have the same form under $\psi_L \rightarrow e^{ig'\frac{Y_L}{2}\theta + ig\vec{\alpha}\cdot\vec{\tau}}\psi_L$ for some $U(1)_L$ hypercharge Y_L , and $\psi_R \rightarrow e^{ig'\frac{Y_R}{2}\theta}\psi_R$ for some $U(1)_R$ hypercharge Y_R . $\vec{\tau} = (\frac{\sigma_1}{2}, \frac{\sigma_2}{2}, \frac{\sigma_3}{2})$ are the generators of $SU(2)$ in terms of the Pauli matrices. In such a transformation, the fields in Lagrangian 1.9 would remain invariant under $B_\mu \rightarrow B_\mu - \frac{2}{g'Y_{L,R}}\partial_\mu\theta$ and $W_\mu^i\tau^i \rightarrow e^{ig\vec{\alpha}\cdot\vec{\tau}}W_\mu^i\tau^i e^{-ig^*\vec{\alpha}\cdot\vec{\tau}} - \frac{1}{g}\partial_\mu e^{ig\vec{\alpha}\cdot\vec{\tau}}e^{-ig^*\vec{\alpha}\cdot\vec{\tau}}$. The invariance of Eqn. 1.8 can be achieved if the covariant derivatives are defined as $\nabla_L^\mu = \partial_L^\mu - igW^{i,\mu}\tau^i - ig'\frac{Y_L}{2}B^\mu$ for the ϕ_L terms in Eqn. 1.8 and $\nabla_R^\mu = \partial_R^\mu - ig'\frac{Y_R}{2}B^\mu$ for the ϕ_R terms.

The interaction terms between the different bosons and fermions is subtle in the present form of Eqn. 1.8, after the covariant derivative replacement. It is however possible to make transformations between the gauge fields to

elucidate the interactions:

$$\begin{aligned}
W_\mu^\pm &= (W_\mu^1 \mp iW_\mu^2) / \sqrt{2} \\
Z_\mu &= (W_\mu^3 \cos \theta_W - B_\mu \sin \theta_W) \\
A_\mu &= (W_\mu^3 \sin \theta_W + B_\mu \cos \theta_W).
\end{aligned} \tag{1.10}$$

Here, θ_W is the Weinberg angle, where $\cos \theta_W = \frac{g}{\sqrt{g^2 + g'^2}}$ and $\sin \theta_W = \frac{g'Y}{\sqrt{g^2 + g'^2}}$. We will see in Section 1.3 that at leading order (LO) perturbation theory, $\cos^2 \theta_W = m_W^2 / m_Z^2$, and corrections starting at next-to-leading order (NLO) perturbation theory change this identity and make it scale-dependent. The measured value $\sin^2 \theta_W$ at the Z boson mass is $\sin^2 \theta_W(m_Z) \approx 0.23122$ [16].

Before quoting the final interaction Lagrangian, we can now make some observations on Y , Y_L and Y_R in the theory. For neutrinos, the relevant interaction Lagrangian term to photons scales with $-\frac{igg'}{\sqrt{g^2 + g'^2}} \cdot \left[\frac{Y}{2} + \frac{Y_L}{2} \right]$. We know however that neutrinos have no charge, so they do not couple to photons, so $Y_L = -Y$. For charged leptons, the strength of coupling to the electromagnetic field is $-\frac{gg'}{\sqrt{g^2 + g'^2}} \cdot \left[-\frac{Y}{2} + \frac{Y_L}{2} \right]$ for left-handed electrons and $-\frac{gg'}{\sqrt{g^2 + g'^2}} \cdot \left[\frac{Y_R}{2} \right]$ for right-handed ones. Since left- and right-handed leptons should couple with the same strength $-e$ to photons, $Y_R = 2Y_L$. The more general relationship that holds for any particle is $Q = \tau_{L,R}^3 + \frac{Y_{L,R}}{2}$, where $\tau_{L,R}^3$ is the weak isospin eigenstate of the left- or right-handed fermion under the $SU(2)$ generator τ^3 (i.e. $+\frac{1}{2}$ for ν and q_u , and $-\frac{1}{2}$ for ℓ^- and q_d).

With this information, the neutral current Lagrangian reads as a summation over the helicity indices as

$$\begin{aligned}\mathcal{L}_{NC} = & - \sum_{j=L,R} \bar{\psi}_j \gamma^\mu \left[A_\mu \left(g \sin \theta_W \tau^3 + g' \cos \theta_W Y_j \right) \right. \\ & \left. + Z_\mu \left(g \cos \theta_W \tau^3 - g' \sin \theta_W Y_j \right) \right] \psi_j.\end{aligned}\quad (1.11)$$

In terms of more conventional variables, Eqn. 1.11 can be re-written as a summation over fermions as

$$\begin{aligned}\mathcal{L}_{NC} = & - \sum_f \bar{f} \gamma^\mu \left[A_\mu Q_f e \right. \\ & \left. + Z_\mu \frac{e}{\sin 2\theta_W} \left(g_V^f - g_A^f \gamma_5 \right) \right] f,\end{aligned}\quad (1.12)$$

where $g_V^f = \tau_f^3 (1 - 4Q_f \sin^2 \theta_W)$ and $g_A^f = \tau_f^3$ are the vector and axial couplings of each fermion f to the Z boson.

The charged current Lagrangian for interactions with the W^\pm bosons has a simpler form, such that the coupling strength of each fermion flavor pair is the same, and the bosons only couple to left-handed fermion currents:

$$\begin{aligned}\mathcal{L}_{CC} = & - \frac{g}{2\sqrt{2}} \sum_q \left[\bar{q}_u W_\mu^- \gamma^\mu (1 - \gamma_5) q_d + h.c. \right] \\ & - \frac{g}{2\sqrt{2}} \sum_l \left[\bar{\nu}_l W_\mu^- \gamma^\mu (1 - \gamma_5) e + h.c. \right].\end{aligned}\quad (1.13)$$

Lagrangian 1.13 omits the fact that pairs of up- and down-type quarks from different generations may couple to the W boson for simplicity. The vector of down-type states q_d is rotated by the unitary Cabibbo-Kobayashi-Maskawa

(CKM) matrix [17, 18], which can be parameterized by three mixing angles and the CP-violating KM phase. A conventional choice has been the following form [16, 19]:

$$\begin{aligned}
V_{CKM} &= \begin{pmatrix} V_{ud} & V_{us} & V_{ub} \\ V_{cd} & V_{cs} & V_{cb} \\ V_{td} & V_{ts} & V_{tb} \end{pmatrix} \\
&= \begin{pmatrix} 1 & 0 & 0 \\ 0 & c_{23} & s_{23} \\ 0 & -s_{23} & c_{23} \end{pmatrix} \begin{pmatrix} c_{13} & 0 & s_{13}e^{-i\delta_{13}} \\ 0 & 1 & 0 \\ -s_{13}e^{i\delta_{13}} & 0 & c_{13} \end{pmatrix} \begin{pmatrix} c_{13} & s_{13} & 0 \\ -s_{13} & c_{13} & 0 \\ 0 & 0 & 1 \end{pmatrix},
\end{aligned} \tag{1.14}$$

where $c_{ij} = \cos \theta_{ij}$ and $s_{ij} = \sin \theta_{ij}$ refer to the three phases, and δ_{13} is the CP-violating phase. Experimental measurements indicate $|V_{ud}| = 0.97400 \pm 0.00021$, $|V_{us}| = 0.2243 \pm 0.0005$, $|V_{cd}| = 0.218 \pm 0.004$, $|V_{cs}| = 0.997 \pm 0.017$, $|V_{cb}| = (42.2 \pm 0.8) \times 10^{-3}$, $|V_{ub}| = (3.94 \pm 0.36) \times 10^{-3}$, $|V_{td}| = (8.1 \pm 0.5) \times 10^{-3}$, $|V_{ts}| = (39.4 \pm 2.3) \times 10^{-3}$, and $|V_{tb}| = 1.019 \pm 0.025$ [16].

1.2 Fundamental interactions in Quantum Chromodynamics

The theory of Quantum Chromodynamics describes how quarks interact with each other via the strong force mediators, gluons. The theory constructed is similar to the Electroweak Theory described in Section 1.1, but it is based on $SU(3)_C$ color symmetry.

A quark in this field is denoted by a triplet of arbitrarily-named red, green and blue color charges:

$$q_{u,d} = \begin{pmatrix} q_{u,d}^r \\ q_{u,d}^g \\ q_{u,d}^b \end{pmatrix}. \tag{1.15}$$

The field Lagrangian can be written in a similar way to Eqn. 1.9 as

$$\mathcal{L}_G = -\frac{1}{4}G^{a,\mu\nu}G_{\mu\nu}^a - \frac{\theta g_s^2}{32\pi^2}G^{a,\mu\nu}\tilde{G}_{\mu\nu}^a, \quad (1.16)$$

where $G_{\mu\nu}^a = \partial_\mu G_\nu^a - \partial_\nu G_\mu^a - g_s f_{abc} G_\mu^b G_\nu^c$ is the antisymmetric field tensor for the gluon field $G_\mu^a = G_\mu t^a$. $t^a = \frac{\lambda^a}{2}$ are the eight 3×3 generators of $SU(3)$ composed of the Gell-Mann matrices λ^a , and $f_{abc} = \pm 1$ are the structure constants of $SU(3)$ satisfying $[t^a, t^b] = if_{abc}t^c$ commutation relationship. The constant g_s is the strong coupling constant, and summation over the eight generators is implied in the double a index. The summation implies tri- and tetra-gluon interaction vertices. The second term proportional to $G^{a,\mu\nu}\tilde{G}_{\mu\nu}^a$ violates CP. In this term, $\tilde{G}_{\mu\nu}^a = \frac{1}{2}\epsilon_{\mu\nu\alpha\beta}G^{a,\alpha\beta}$ is the dual gluon field tensor, and θ is the CP violation contribution. Experimental limits on neutron electric dipole moment constrain $|\theta| \lesssim 10^{-10}$ [16, 20], so we do not consider this contribution further.

The free quark Lagrangian for each color, or helicity, is in a similar form to the Lagrangian 1.2

$$\mathcal{L}_Q = \bar{q}_{u,d}^a (i\gamma^\mu \partial_\mu - m) q_{u,d}^a. \quad (1.17)$$

The argument of symmetry in Section 1.1 can also be followed for this non-abelian group to replace the partial derivative with the covariant derivative $\partial_\mu \rightarrow \nabla_\mu = \partial_\mu - ig_s G_\mu$ to obtain the interaction term between a gluon and a $q\bar{q}$ pair.

Quarks have never been observed as free particles. Instead, they are observed as constituents of mesons (bound state of a $q\bar{q}'$ pair), baryons (bound state of three quarks) or more exotic states with more than three bound quarks.

The top quark is exceptionally massive and decays before it has time to be part of a bound state. The absence of free quarks makes it difficult to define the mass of a quark when the mass of a fermion is usually defined as its observed invariant mass in a free state. A perturbatively defined prescription is the pole mass, which corresponds to the position of the divergence of the quark propagator. This corresponds to the usual definition of mass but suffers from non-perturbative ambiguities. An alternative is the \overline{MS} mass, $\bar{m}_q(\mu_R^2)$, which depends on the renormalization scale μ_R . The scale is usually chosen as the approximate invariant mass of the quark in the interaction (i.e. ≈ 2 GeV). In the computations of scattering matrix elements involving the H boson, this scale is very small compared to the typical invariant masses of the processes, so the quark masses (as well as lepton masses) are typically neglected.

1.3 Spontaneous symmetry breaking and the Higgs mechanism

The mechanism of EWSB provides an approach to give the W and Z bosons their masses without modifying their high energy behavior. In this mechanism, the Higgs field is a doublet under $SU(2)_L$ with $Q = \tau^3 + \frac{Y}{2}$,

$$\Phi = \frac{1}{\sqrt{2}} \begin{pmatrix} \phi_1^+ + i\phi_2^+ \\ \phi_3^0 + i\phi_4^0 \end{pmatrix}. \quad (1.18)$$

The free Higgs field Lagrangian is simply

$$\mathcal{L}_H = (\partial_\mu \Phi)^\dagger (\partial^\mu \Phi). \quad (1.19)$$

The Lagrangian 1.19 is required to be invariant under $SU(2)$ and $U(1)$ transformations. The field transforms as $\Phi \rightarrow e^{-ig\vec{\alpha}\cdot\vec{\tau}}\Phi$ under $SU(2)$ and as $\Phi \rightarrow e^{-ig'\frac{Y}{2}\alpha}\Phi$ under $U(1)$, so the partial derivatives are replaced with $\nabla^\mu = \partial^\mu - igW^{i,\mu}\tau^i - ig'\frac{Y}{2}B^\mu$. Here, Y is the hypercharge of the H boson.

In the EWSB mechanism, the Higgs potential takes the form

$$\Delta\mathcal{L} = -\frac{1}{2}\lambda^2\left(\Phi^\dagger\Phi - \frac{v^2}{2}\right)^2 \quad (1.20)$$

such that the potential has a minimum at $|\Phi| = \frac{v}{\sqrt{2}}$. For this reason, we reduce the 4 degrees of freedom in the original Higgs doublet 1.18 to a real field and the vacuum expectation value:

$$\Phi = \frac{1}{\sqrt{2}}\begin{pmatrix} 0 \\ v + h(\mathbf{x}) \end{pmatrix}. \quad (1.21)$$

At the vacuum energy (i.e. $h(\mathbf{x}) \rightarrow 0$), the interaction terms in the Lagrangian 1.19 take the form

$$\begin{aligned} \mathcal{L}_{mV} &= \frac{v^2 g^2}{8} \left(W_\mu^{1\dagger} W^{1,\mu} + W_\mu^{2\dagger} W^{2,\mu} \right) \\ &+ \frac{v^2}{2} \left(\frac{g}{2} W^{3,\mu} - \frac{g'Y}{2} B^\mu \right)^2 \end{aligned} \quad (1.22)$$

With the rotation for Z and W^\pm fields shown in Eqn. 1.11 in mind, the first term in Eqn. 1.22 corresponds to $m_W^2 = \frac{v^2 g^2}{4}$, and the second term corresponds to $m_Z^2 = \frac{v^2 g^2}{4 \cos^2 \theta_W} = \frac{m_W^2}{\cos^2 \theta_W}$. Notice that the number of extra degrees of freedom (Goldstone bosons [21–23]) in the Higgs doublet 1.18 corresponds exactly to the appearance of three mass terms. Notice also that the photon field A^μ does not receive mass as expected.

The full interaction Lagrangian between the Higgs field (i.e. $v + h(\mathbf{x})$), the W and Z bosons and itself is interpreted from Eqns. 1.19 and 1.20 as

$$\begin{aligned}\mathcal{L}_{H\text{int}} = & \left(1 + \frac{h}{v}\right)^2 \left(\frac{m_Z^2}{2} Z_\mu Z^\mu + m_W^2 W_\mu^+ W^{-,\mu} \right) \\ & + \frac{3m_H^2}{v^2} \left(\frac{vh^3}{3!} + \frac{h^4}{4!} \right).\end{aligned}\tag{1.23}$$

This Lagrangian gives rise to tri-boson HZZ, HWW, HHH and tetra-boson HHZZ, HHWW and HHHH interactions at tree-level.

From the Higgs potential in Eqn. 1.20, one also reads the mass of the H boson to be $m_H^2 = \lambda v^2$. The most precise value measured experimentally comes from ATLAS and CMS collaborations to be $m_H = 125.09 \pm 0.21$ (stat.) ± 0.11 (syst.) GeV [24]. This value of m_H implies that the H boson self-coupling remains perturbative at the Planck scale [16, 25, 26], but the measured value also indicates that the self-coupling can become negative at an energy scale $\Lambda = \mathcal{O}(10^{10} - 10^{12})$ GeV due to its perturbative evolution. If the energy of interactions exceed this Λ scale, or if enough time passes to allow quantum fluctuations to happen at this scale, the SM Higgs potential may no longer remain stable [27, 28]. The metastability of the Higgs vacuum, if not the case in reality, requires new physics below the scale Λ .

1.4 The Yukawa mechanism for fermion masses

A mass term in the Dirac fermion Lagrangian 1.2 would mix left- and right-handed fermions, and because these fermions have different $SU(2)_L \otimes U(1)_Y$ charges, such a term would violate gauge invariance. The Yukawa interaction

provides a method for the fermions to acquire their mass with the interaction between Ψ_L, f_R and the Higgs doublet Φ .

For each fermion generation, the Yukawa Lagrangian is

$$\mathcal{L}_Y = g_f (\bar{\Psi}_L \Phi f_R + \text{h.c.}), \quad (1.24)$$

where the coupling g_f is the coupling strength of the fermions to the Higgs doublet. After rotating the Higgs doublet as in Eqn. 1.21, the Lagrangian becomes

$$\begin{aligned} \mathcal{L}_Y &= \frac{g_f v}{\sqrt{2}} (\bar{f}_L f_R + \bar{f}_R f_L) \\ &+ \frac{g_f h}{\sqrt{2}} (\bar{f}_L f_R + \bar{f}_R f_L). \end{aligned} \quad (1.25)$$

It is seen from the Lagrangian 1.25 that the mass of the fermion is $m_f = \frac{g_f v}{\sqrt{2}}$, and the interaction strength of the fermion to the H boson is $\frac{m_f}{v}$, proportional to the mass of the fermion. The Lagrangian also implies that the H boson does not interact with neutrinos unless right-handed neutrinos exist and neutrinos are massive. If the masses of neutrinos are non-zero, oscillations between different flavors is expected via the Pontecorvo-Maki-Nakagawa-Sakata (PMNS) matrix [29, 30]. Experimentally, right-handed neutrinos have not been found, but flavor oscillations have been observed, first by the SNO Experiment [31] in solar neutrinos and later by other atmospheric [32], reactor [33–35] and beam [36, 37] neutrino experiments. The mechanism of how neutrino masses are acquired and whether they interact with the H boson are still open questions in the SM to this day.

Chapter 2

The CERN Large Hadron Collider and the Compact Muon Solenoid Detector

The conventional method for studying the interactions between fundamental particles at a desired energy has been to use a particle accelerator to accelerate a chosen particle to this energy, and then to either aim it at a fixed solid, liquid or gaseous target or collide it with another accelerated particle. In fixed-target experiments, the energy available in the collision grows with the square-root of the incident beam energy, whereas in colliders, the collision energy grows linearly with the energy of the incident beam. The accelerated particles in both cases are typically protons or electrons, which are stable and easy to produce in abundance. In the case of electrons, the energy of the beam can be tuned precisely to make observations at a very narrow energy range. The proton is composed of valence and sea quarks and gluons, so even though the energy of the proton beam can still be tuned equally well, the energy of interaction between two constituent partons covers a wider range. The CERN Large

Hadron Collider (LHC) is constructed as a circular proton-proton collider for this purpose, to be able to measure the properties of SM particles and search for physics beyond the SM (BSM physics) at a wide, high energy spectrum.

Four different experiments, CMS, ATLAS, ALICE and LHCb, are situated on the perimeter of the LHC. CMS and ATLAS detectors are for general purposes using proton-proton, proton-heavy ion and heavy ion-heavy ion collisions. They target measurements ranging from precision measurements of different SM processes, searches for BSM physics, and heavy flavor physics. ALICE and LHCb detectors are more specialized for heavy flavor physics and for using heavy ion collisions in place of protons. We begin our discussion in this chapter with a more detailed description of the LHC in Section 2.1. We then proceed in Section 2.2 with a discussion of the CMS detector, which is the source of the data used in the results presented by this thesis. We finally discuss in Section 2.4 how the different particles (i.e. muons, electrons and hadronic jets) are triggered, reconstructed and identified. Because many of the results in this work use $H \rightarrow 4\ell$ events, we also describe in Section 2.4 how these event candidates are identified. We defer the discussion of how these candidates can be analyzed to probe BSM physics to Chapter 3.

2.1 Design and specifications of the LHC

The LHC complex is shown in Fig. 2.1. It is built around a 27-kilometer circular tunnel with two concentric rings and a mean depth of 100 m. The tunnel was originally used for LEP to collide electrons and positrons. Protons or heavy ions can be accelerated in the tunnel without substantial loss in their energy

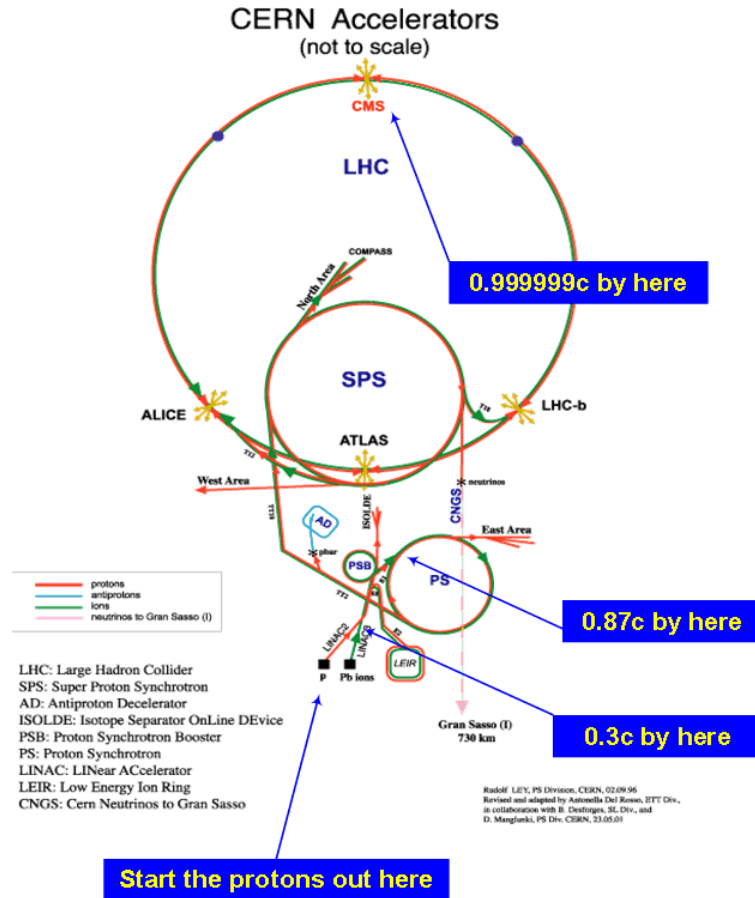


Figure 2.1: The different rings and components contributing to the acceleration of protons at the LHC [38].

per turn through synchrotron radiation, and collisions at a center of mass energy of 7, 8 or 13 TeV are achieved in the case of proton-proton collisions. The first stage of preparing the protons for such high energy collisions is to accelerate them in LINAC 2 to 50 MeV in energy. These protons are then fed into the Proton Synchrotron booster, where they are accelerated up to 1.4 GeV. They are subsequently injected into the Proton Synchrotron, which increases their energy to 26 GeV. Finally, the Super Proton Synchrotron accelerates the protons to 450 GeV for injection into the main tunnel. Once reaching the LHC,

a series of 1232 superconducting dipole magnets with radio-frequency cavities keep the protons along the ring and increase their energy over a period of 5 to 24 hours to half of the desired collision center-of-mass energy. As the proton bunches accelerate, the protons may diffuse. Therefore, additional quadrupole magnets in alternating configurations are installed to focus the beam. Each bunch of protons contains $\mathcal{O}(10^{11})$ protons and every run contains 2808 bunches. Collisions of bunches are timed to occur either 50 or 25 ns apart.

The luminosity can be defined in terms of the accelerator's parameters in units of inverse area as

$$\mathcal{L} = \frac{\gamma \nu N_B N_p^2}{4\pi \epsilon_n \beta^*} \mathcal{F} \quad (2.1)$$

where $\gamma = \frac{1}{\sqrt{1-\beta^2}}$ is the relativistic Lorentz factor, ν the frequency at which bunches revolve around the rings, N_B the number of bunches, and N_p the number of protons in a bunch. ϵ_n , the normalized transverse emittance, and β^* , the betatron function at the point of interaction, both quantify the physical size of the beam. \mathcal{F} is a geometrical reduction factor caused by the crossing angle of the beams, which is planned to be increased in the near future by reducing the crossing angle of the beams by inserting crab cavities near the interaction points. The number of events for a generic particle to be produced depends on its probability, expressed in units of area as a cross section (σ), and the luminosity as $\sigma \times \mathcal{L}$.

2.2 Design and specifications of the CMS detector

An enlarged view of the CMS detector is given in Fig. 2.2. The central feature of the CMS apparatus is a superconducting solenoid of 6 m internal diameter,

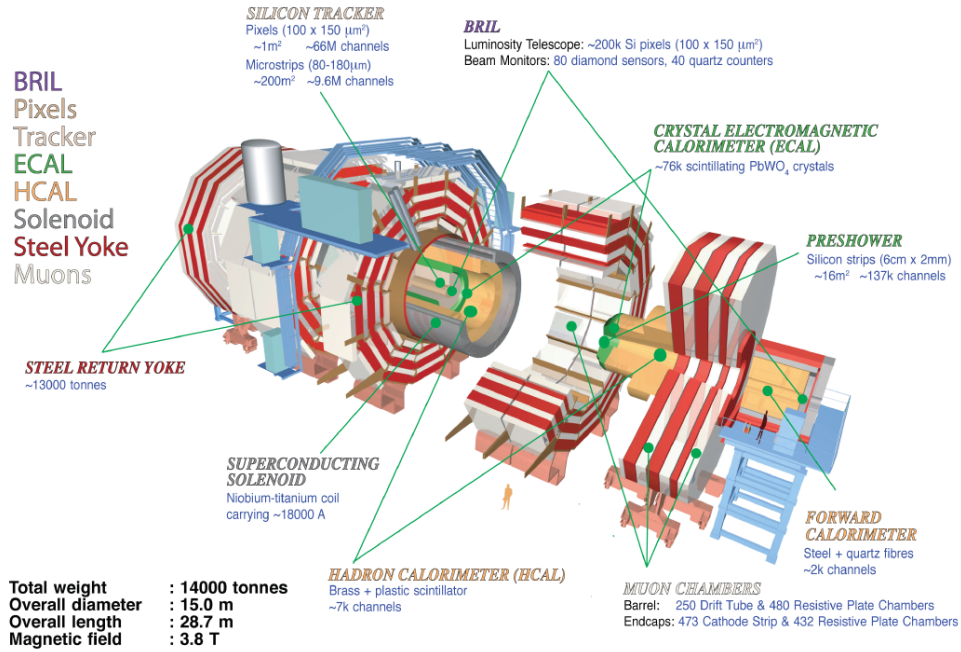


Figure 2.2: Shown are the different components of the CMS detector. At the center are the silicon pixel and strip trackers. Surrounding the tracker components are the preshower, and barrel and endcap electromagnetic hadronic calorimeters. The barrel hadronic calorimeter is separated into HB (inner) and HO (outer) regions by the superconducting solenoid, and the hadronic calorimeter endcaps are organized as HE (near) and HF (far) components to provide better coverage of jets at larger pseudorapidity. The muon chambers and the steel return yoke are located at the outermost layers of the detector. [39].

providing a magnetic field of 3.8 T. Most muons are detected in aluminum drift tubes (DT) in the barrel region or cathode strip chambers (CSCs) in the endcap region, embedded in the steel flux-return yoke outside the solenoid. Each muon system is complemented by resistive plate chambers (RPCs) embedded in the steel flux-return yoke outside the solenoid. Within the solenoid volume are silicon pixel and strip trackers, a lead tungstate crystal electromagnetic calorimeter (ECAL), and a brass and scintillator hadron calorimeter (HCAL), each composed of a barrel and two endcap sections. The forward calorimeters

outside the steel return yoke extend the pseudorapidity ($\eta = \frac{1}{2} \ln \left(\frac{|\vec{v}|+v_z}{|\vec{v}|-v_z} \right)$ for any vector \vec{v}) coverage provided by the barrel and endcap detectors.

The CMS detector features a tracker at its core. The tracking volume is contained in a cylinder of 5.8 m length and 2.6 m in diameter. Ten layers of silicon microstrip detectors provide the required granularity and precision to reconstruct charged tracks in high multiplicity events efficiently. The silicon microstrip tracker, with its long bending path and the strong solenoidal field, provides excellent momentum resolution. In addition, the detector is designed initially with three layers of silicon pixel detectors in the barrel region and two forward disks at each end to seed track reconstruction, improve impact parameter measurements, and provide points with sufficient resolution to reconstruct secondary vertices from decays of particles containing b and c quarks [39, 40]. The barrel pixel detector is replaced in 2017 with four layers, and the forward pixel detector is replaced with three disks.

2.2.1 The inner tracker

At an LHC luminosity of $10^{34} \text{ cm}^2\text{s}^{-1}$, more than 20 proton-proton interactions occur at the interaction point during each bunch crossing, causing an average of 1000 particles to traverse the tracker. As the CMS tracker is closest to the interaction point, a detector technology featuring high granularity and fast response is required such that the trajectories can be identified reliably and attributed to the correct bunch crossing. These features imply a high power density of the on-detector electronics which in turn requires efficient cooling,

and this requirement conflicts with the objective to reduce the amount of material and limit multiple scattering, bremsstrahlung, photon conversion and nuclear interactions. The intense particle flux also causes the accumulation of radiation damage to the tracking system over time. With these considerations in mind, the CMS tracker has been chosen to consist entirely of silicon sensors. The subsystems closest to the interaction point are highly granulated pixel detectors, and silicon microstrip sensors are used farther away from the interaction point.

The pixel detector was designed to be initially composed of three barrel layers (BPIX) at radii 4.4 cm, 7.3 cm and 10.2 cm and a silicon strip tracker with 10 barrel detection layers extending outwards to a radius of 1.1 m. The barrel system is complemented by endcaps, which consist of two disks in the pixel detector (FPix), and three (tracker inner detector, TID) and nine (tracker endcap, TEC) disks in the strip tracker on each side, extending the acceptance of the tracker up to a pseudorapidity of $|\eta| < 2.5$ [40–42]. The pixel detector was upgraded in 2017 as part of Phase-1 CMS detector upgrade projects [43]. The initial Phase-0 tracker configuration and the upgraded Phase-1 pixel components are illustrated in Fig. 2.3. We discuss the different subsystems and configurations below.

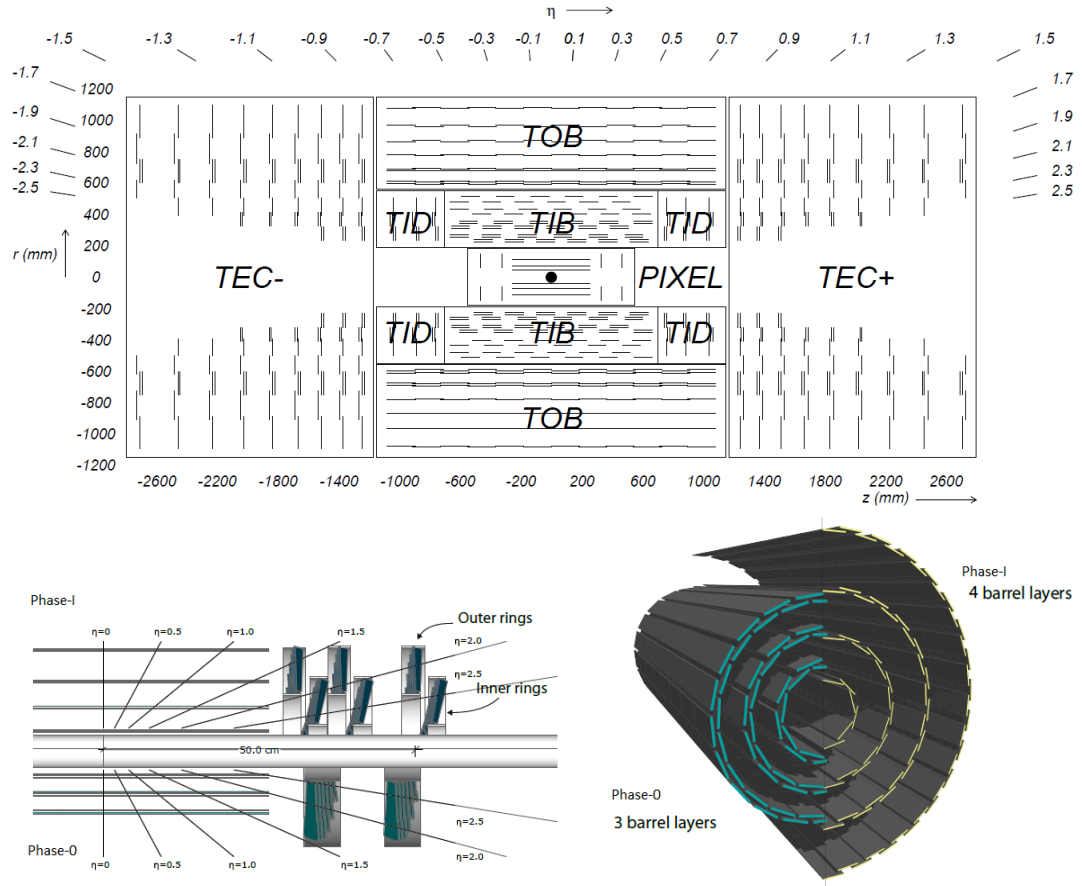


Figure 2.3: Top: Cross sectional view of the CMS Phase-0 tracker. Each line represents a detector module. Double lines indicate back-to-back modules which deliver stereo hits [40]. Bottom: Comparison of Phase-0 and Phase-1 pixel detectors. The left panel shows the conceptual layout of the different layers and disks in the Phase-0 and Phase-1 configurations, and the right panel compares the pixel barrel layers in a transverse-oblique view [43].

2.2.1.1 Phase-0 pixel detector

The pixel system is the part of the tracking system that is closest to the interaction region. It contributes precise tracking points in $r - \phi$ and z and therefore is responsible for a small impact parameter resolution, which is important for good secondary vertex reconstruction. Containing 1440 modules in total, the pixel detector also ensures high granularity and good tracking performance.

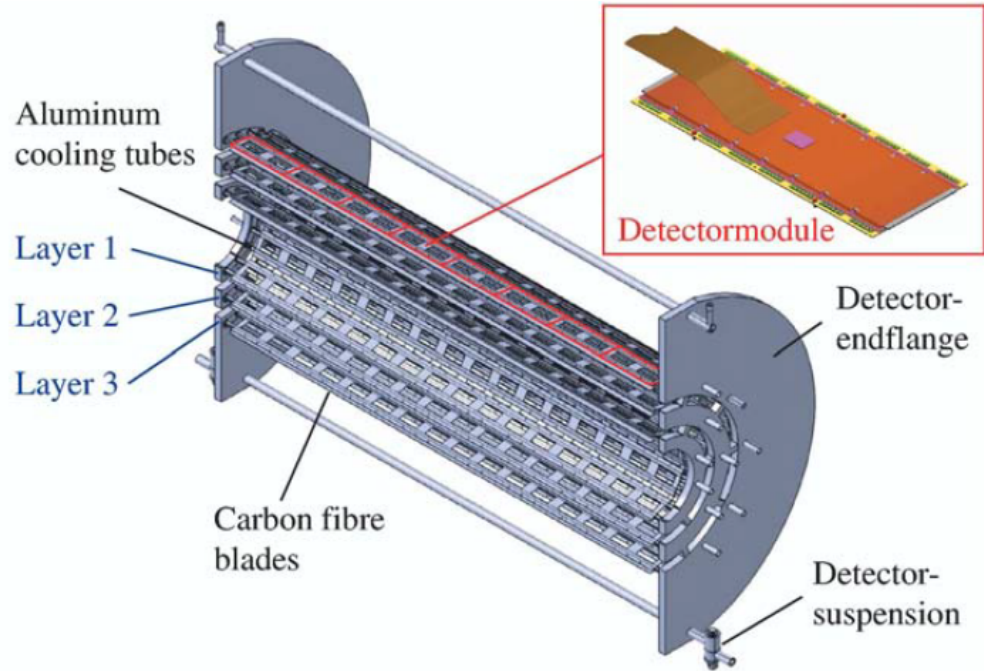


Figure 2.4: Phase-0 BPIX half-barrel support structure with the three detector layers [40].

As shown in Fig. 2.4, the BPIX is constructed as two 53 cm-long half-barrels, each of which containing carbon fiber ladders of thickness 0.24 mm on which the sensor modules are mounted. The modules on each ladder alternate between pointing toward or away from the interaction point. Cooling is done

at about -10°C with C_6F_{14} via aluminum cooling tubes passing adjacent to the ladders. About 800 detector modules lie on these ladders. While the majority of the modules (672) are full modules with 16 readout chips (ROC), the edges of the six half-barrels are equipped with 16 half-modules with 8 ROCs (96 in total). A module is composed of one or two base strips made from $250\text{ }\mu\text{m}$ thick silicon nitride to provide the support of the module. The sensors on each module are designed as n-pixel on an n-substrate, and this design allows partially depleted operation even at very high particle fluences. The front end electronics consists of 8 or 16 ROCs with 52×80 pixels of size $100\text{ }\mu\text{m} \times 150\text{ }\mu\text{m}$, each of which are bump-bonded to the sensor, and they provide analog readout at 40 MHz. The ROCs are thinned down to $180\text{ }\mu\text{m}$. The upper layer of each module consists of a High Density Interconnect (HDI) printed circuit board with a trace thickness of $6\text{ }\mu\text{m}$ to distribute the signal and power to the chips. The HDI is equipped with a Token Bit Manager (TBM) chip that controls the readout of the ROCs. The signals are transferred over a Kapton/copper compound cable with 21 traces and a $300\text{ }\mu\text{m}$ -pitch. Each module is powered via 6 copper coated aluminum wires of $250\text{ }\mu\text{m}$ in diameter. The electric field in each module points towards or away from the interaction point, and the drift of the electrons and holes in the sensors is in a direction parallel to the electric field \vec{E} . This drift is corrected due to the magnetic field \vec{B} of CMS in the direction of $\hat{E} \times \hat{B}$. The resulting Lorentz drift leads to the spreading of the collected signal charge over more than one pixel. Analog pulse height readout and charge interpolation from the sensors result in $1520\text{ }\mu\text{m}$ spatial resolution, varying as a function of track pseudorapidity and p_{T} .



Figure 2.5: Phase-0 FPIX half-cylinder support structure. The FPIX half-disk cooling channels are mounted in the outer half-ring structure, and the panels are mounted on both sides of the cooling channels [40].

The two FPIX detector sections at each end of the BPIX are split vertically down the middle into two half-cylinders so that the detector can be installed around the beam-pipe and its vertical support wire and removed for servicing during major maintenance periods without disturbing the beam-pipe. Each half-cylinder consists of a carbon fiber shell with two half-disks located at its front end, one at 34.5 cm from the interaction point and the other at 46.5 cm. Illustrated in Fig. 2.5, the half-disks support the actual pixel detector that extend from 6 cm to 15 cm in radius from the beam, and each half-disk supports 12 “U”-shaped cooling channels, arranged in a turbine-like structure with a 20° tilt. The cooling channels have two trapezoidal Be panels, attached on each side, and this arrangement forms a 12-blade structure. The modules on the blades are cooled down to -15°C with C_6F_{14} and have essentially the same structure as in the barrel modules, with minor differences. The

turbine-like arrangement also induces charge-sharing, just like in the barrels.

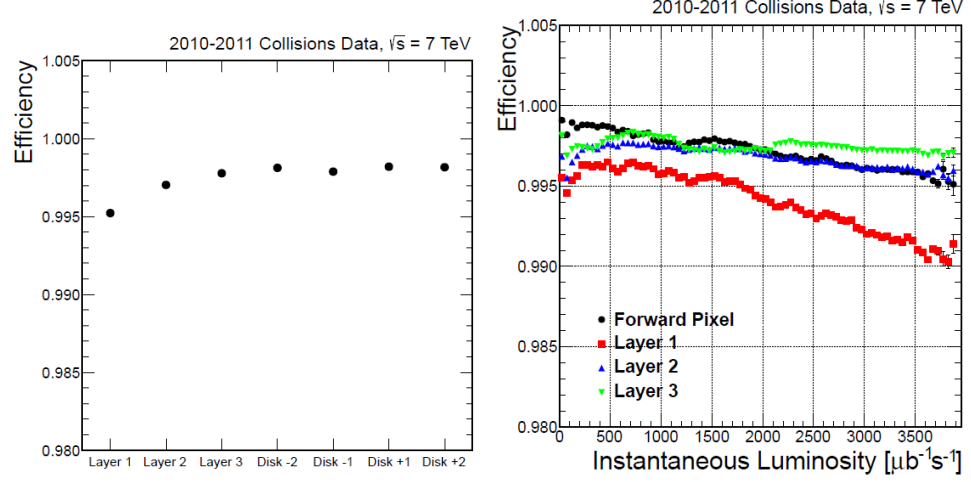


Figure 2.6: Pixel tracking performance measurements from 2010 and 2011 data. Left: Average module hit efficiency per layer/disk in the pixel detector once modules excluded from the readout are excluded from the measurement. Right: Average module hit efficiency as a function of the instantaneous luminosity [43].

Figure 2.6 shows the hit (i.e. charge deposition) efficiencies of each BPIX layer or FPIX disk and the collective hit efficiency as a function of instantaneous luminosity, measured from data collected in 2010 and 2011. The efficiency is in general worse in BPIX Layer 1, and in all subdetectors, it also worsens as instantaneous luminosity is increased. The primary reasons of these inefficiencies are limits in the internal readout chip buffers, and occasional temporary losses of modules. These dynamic inefficiencies reach a significant level, up to 15%, when the average number of interactions within a single bunch crossing reaches 50 or more and when the instantaneous luminosity reaches $2 \times 10^{34} \text{ cm}^2\text{s}^{-1}$. With these considerations, the pixel detector was replaced in 2017 to cope with these challenges.

2.2.1.2 Phase-1 pixel detector

Table 2.1: Comparison of Phase-0 and Phase-1 pixel detector ROC specifications. The values in parentheses for double column speed and data loss are for the chips used in Phase-1 BPIX Layer 1 [43].

	Phase-0	Phase-1
ROC size	7.9 mm \times 9.8 mm	7.9 mm \times 10.2 mm
Pixel size	100 μ m \times 150 μ m	100 μ m \times 150 μ m
Settable DACs / registers	26 / 2	19 / 2
Pixel charge readout	Analog	Digitized, 8-bit
Readout speed	40 MHz	160 Mbit/s
Time stamp buffer size	12	24
Data buffer size	32	80
Output buffer FIFO	No	Yes
Double column speed	20 MHz	20 MHz (40 MHz)
Metal layers	5	6
Leakage current compensation	Yes	No
In-time threshold	3500 e	< 2000 e
Data loss at max. operating flux	$\sim 3.8\%$ at 120 MHz/cm ²	1.6% at 160 MHz/cm ² ($\sim 3\%$ at 580 MHz/cm ²)

The upgraded BPIX contains four layers at radii 3.0 cm, 6.8 cm, 10.9 cm and 16.0 cm [43]. All layers are equipped with 2×8 -ROC modules of equal size (22 mm \times 66 mm). The module is slightly wider than those used during Phase-0 because of the increased periphery of the ROCs. The length of BPIX in z is unchanged. The analog readout at 40 MHz, digitized to 400 Mbit/s, has been changed to 160 Mbit/s digital, resulting in a doubling of the data throughput per fiber. For the outer layers (L2-L4), this provides sufficient reserve for the future expected LHC operations. For the innermost layer (L1), the number of fibers per module is in addition increased from two to four,

resulting in an overall factor of 4 over the Phase-0 L1 situation. A number of design modifications in the periphery of the readout chip allow efficient operation under these increased data rates. The changes in readout protocol and link speed also require modifications of the TBM, the optical link and the Front End Driver. A comparison of the ROC specifications between Phase-0 and Phase-1 designs are shown in Table 2.1.

The upgraded FPIX detector still consists of two sections which are vertically separated with a left and right set of half-disks on each side. The pixel modules are assembled on half-disk support structures with radial coverage ranging from 4.5 to 16.1 cm. The upgrade layout uses the same module type as in L2-4 of BPIX. A total of 56 modules (896 ROCs) per half-disk are arranged radially on thermal pyrolytic graphite blades. Half-disks are divided into an outer assembly with 34 modules and an inner ring with 22 modules. The outer and inner assemblies are supported directly from the half cylinder so that the two assemblies can be easily separated. All the modules on the outer assembly are located to minimize the gap in a 4-hit pattern between the end of BPIX L4 and the forward innermost disk, maximizing coverage while minimizing the number of modules. Each blade on the outer assembly is rotated in the same turbine-like geometry, but to obtain excellent resolution in both the azimuthal and radial directions throughout the FPIX acceptance angle for the inner assembly, the blades are arranged in an inverted cone array with the blades tilted by an additional 12° with respect to the interaction point. In FPIX and BPIX, the cooling substrate is chosen to be CO_2 .

2.2.1.3 Strip detector

The strip tracker has 15,148 silicon modules, which in total cover an active area of about 198 m^2 and have 9.3 million strips. It is composed of four subsystems. The tracker inner barrel (TIB) and disks (TID) cover $r < 55 \text{ cm}$ and $|z| < 118 \text{ cm}$, and are composed of four barrel layers supplemented by three disks at each end. These provide position measurements in $r - \phi$ with a resolution of approximately $13 - 38 \text{ } \mu\text{m}$. The tracker outer barrel (TOB) covers $r > 55 \text{ cm}$ and $|z| < 118 \text{ cm}$ and consists of six barrel layers providing position measurements in $r - \phi$ with a resolution of approximately $18 - 47 \text{ } \mu\text{m}$. The tracker endcaps (TEC) cover the region $124 \text{ cm} < |z| < 282 \text{ cm}$. Each TEC is composed of nine disks, each containing up to seven concentric rings of silicon strip modules, with resolution similar to that of the TOB.

The modules in the innermost two layers of both the TIB and the TOB, as well as the modules in rings 1 and 2 of the TID, and 1, 2 and 5 of the TEC, carry a second strip detector module, which is mounted back-to-back to the first. The second modules are rotated in the plane of the module by a “stereo” angle of 100 mrad . The hits from these two modules provide a measurement of the local y coordinate (z in the barrel and r on the disks) [40]. The sensor elements on each strip are single sided p-on-n type silicon micro-strip sensors [44, 45].

2.2.2 Alignment of the tracker

The CMS tracker provides precise tracking information and vertexing capabilities, and in order to reach precision levels not achievable by mechanical mounting during commissioning and to ensure consistent performance over

time, the location of the individual tracker components need to be updated in the software. Installation of modules introduces curvature to the sensor geometry, and changes in the strength of the magnetic field of the CMS solenoid are known to displace the large structures and modules. Calibration of sensor voltages in different subdetector systems due to the aging of sensors may also affect the modeling of Lorentz drift. All of these changes may affect tracker performance, and adjustments of the position and rotation of the tracker modules (software-level alignment) are needed to compensate for these effects. More details on track reconstruction itself are given in Section 2.4.1.

A schematic overview of the alignment workflow is given in Fig. 2.7. The alignables are first determined from the list of modules, or larger alignable structures such as BPIX ladders or the two tracker endcap sides, and the degrees of freedom are specified from three translations and three rotations. Curvature of each module is modeled as the product of the first two Bernoulli polynomials in each of the local x and y directions, so this model corresponds to having an additional six degrees of freedom for stereo modules in TOB and TEC and only three degrees of freedom for the rest of modules. The bowing of the sensors or the displacement of the alignables can be estimated using the difference between the impact points of the reconstructed tracks on the modules and the hit positions recorded, or using the difference between prior survey measurements done during commissioning.

The data is first split into different run intervals of alignment validity (IOVs) according to the changes in sensor calibrations, magnetic fields or any

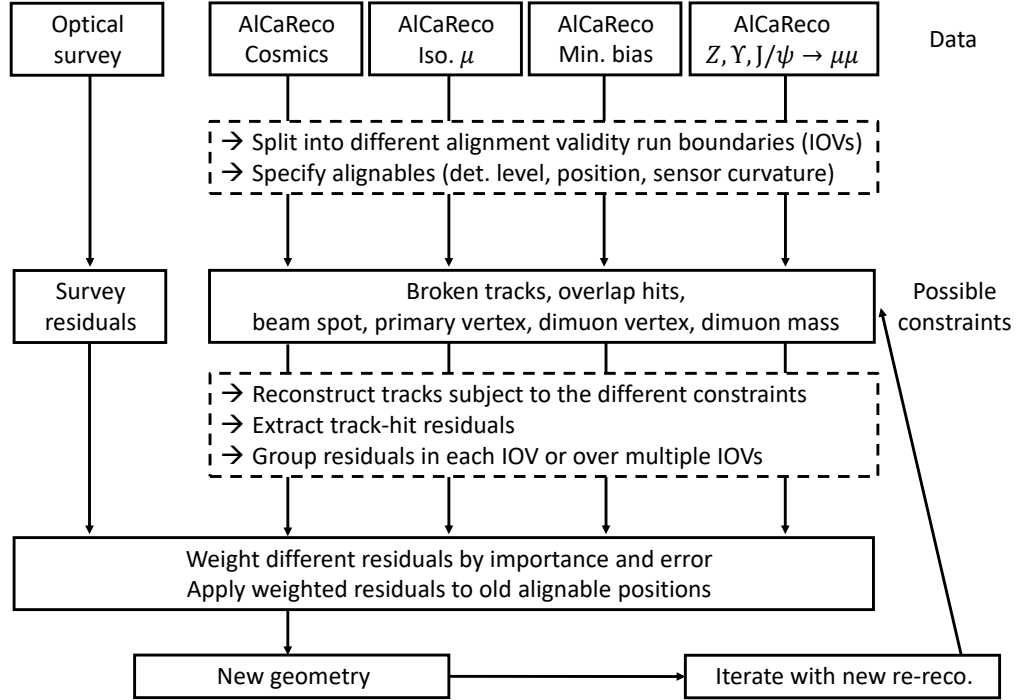


Figure 2.7: Overview of the steps in the tracker alignment workflow. The workflow begins with an initial estimate of the tracker geometry and different input data types, ranging from prior optical survey measurements to cosmics and collision data recorded by the detector. The data is divided into different alignment validity intervals, and possible constraints are chosen to be applied. The tracks are reconstructed with these constraints so that they are propagated to the track-hit residuals. The different displacements predicted by the different inputs are weighted according to their statistical significance, and a final weighted average is applied on each of the old geometry alignable to compute its new position parameters. This procedure is iterated as long as deemed necessary.

other relevant condition. Different constraints such as $Z \rightarrow \mu\mu$ mass and vertex constraint are applied as the tracks are being reconstructed using the initial geometry. The differences (residuals) from the initial geometry are computed after this track reconstruction, and in the case of an alignment over multiple IOVs, they are grouped back into a single set. Typical track-hit residuals computed in alignment are illustrated in Fig. 2.8 from the initial alignment of the 2017 pixel detector using cosmic muons [46]. Weights for the different residual input types are then determined based on a separate evaluation of the statistical errors on the displacement of each alignable predicted by these input types. The displacements are applied with these calculated weights on the old geometry of the alignables in order to derive the new geometry, and this procedure is iterated until adequate convergence is reached.

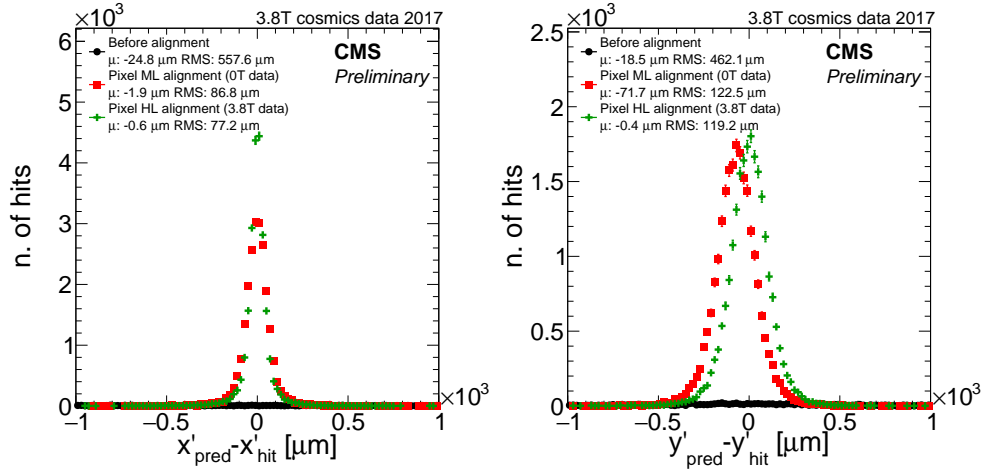


Figure 2.8: Differences in the predicted impact point of the track trajectory to the hit coordinate is shown over the different modules in BPIX. The hit prediction from each track is obtained after refitting the track using all other hits. The left plot shows the residuals in the local x coordinate whereas the right plot shows the same for the local y coordinate. The geometries illustrated are the status at the time of data taking (black circles), the geometry after an alignment of the pixels at the level of modules using cosmics at 0 T magnetic field strength (red squares) and the geometry after a similar, subsequent alignment using cosmics at 3.8 T magnetic field strength [46].

The application of the residuals relies on the minimization of a χ^2 estimator computed as

$$\chi^2(\mathbf{p}, \mathbf{q}) = \sum_i^{\text{modules}} \sum_j^{\text{tracks}} (f_{ij}(\mathbf{p}_i, \mathbf{q}_j) - m_{ij})_c V_{cd}^{-1} (f_{ij}(\mathbf{p}_i, \mathbf{q}_j) - m_{ij})_d,$$

where summation over hit coordinates c and d in the different modules is implied. In the pixel and stereo strip modules, local x and y coordinates can be determined, and in the single strips, only the local x coordinate can be measured. f_{ij} is the predicted impact point based on the trajectory of the track and depends on the geometry (\mathbf{p}_i) and track (\mathbf{q}_j) parameters. The initial geometry description $\mathbf{p}_{i,0}$ is usually available from design drawings, survey measurements, or previous alignment results. This can be used to determine approximate track parameters $\mathbf{q}_{j,0}$. m_{ij} is the vector of hit coordinates for track j on module i . It is important that the trajectory prediction is derived with an unbiased track fit by excluding the hit at the module of concern. The components of V_{cd} , the covariance matrix of the track-hit residuals, are estimated from the error estimates of the hit position and track parameters from all other hits, and the modules' alignment position errors already present in the current geometry.

Assuming alignment corrections to be small, f_{ij} in Eqn. 2.2 can be linearized around these initial values. Minimizing χ^2 after the linearization leads to the normal equations of least squares. These can be expressed as a linear equation system $\mathbf{C}\mathbf{a} = \mathbf{b}$ with $\mathbf{a}^T = (\Delta\mathbf{p}, \Delta\mathbf{q})$, i.e. the alignment parameters $\Delta\mathbf{p}$ and corrections to all parameters of all n used tracks $\Delta\mathbf{q}^T = (\Delta\mathbf{q}_1, \dots, \Delta\mathbf{q}_n)$. There are two approaches utilized in CMS to construct and minimize the χ^2 . In the

global-fit approach [47] using the MILLEPEDE II program [48], the correlations between different modules are taken into account fully, and algebraic properties of the system of linear equations are used to reduce the number of equations by means of block matrix algebra [49]. The HIP/HipPy algorithm [50] uses instead an iterative procedure to account for large alignment corrections that may violate the linear approximation. Since the alignment is done iteratively, the algorithm simplifies the covariance matrix to a block-diagonal matrix, where each block corresponds to a different module being aligned, and the vector \mathbf{a} is simplified as $\mathbf{a}^T = (\Delta \mathbf{p}_i)$. The correlations between the different modules, or the dependence of track parameters on the corrections to the geometry, are ignored as a result of the simplification in computation but are still taken into account as the aligned geometry converges over multiple iterations.

Different track types and physics references can be used to both monitor the effect of the alignment on physics performance directly and introduce as additional constraints to alignment. Figure 2.9 illustrates the geometric effect of alignment on a typical misaligned geometry from a single IOV in the 2016 data. This particular alignment is performed using muons from cosmic rays as well as isolated muons, pairs of muons from $Z \rightarrow \mu\mu$ events, and tracks from minimum bias events (i.e. inelastic proton collisions with loose trigger requirements) [51].

The distribution of the median of residuals over each aligned module

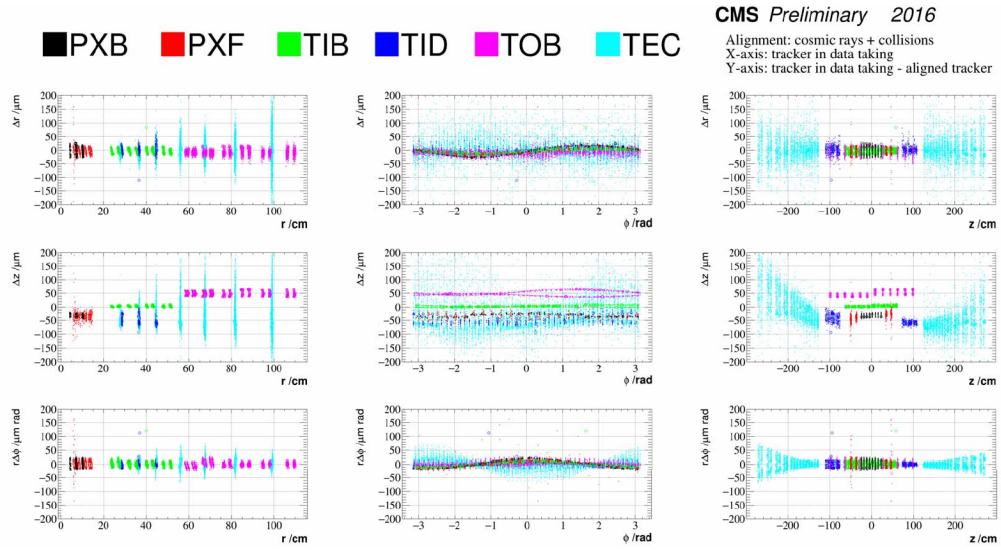


Figure 2.9: Changes in module positions between those during the end of 2016 data taking and after the application of a dedicated alignment. Each point represents a module. Dead modules are indicated with circles; they are not aligned, but they can still change position following the alignment of the higher-level mechanical structure to which they belong. The colors correspond to the different tracker subdetectors indicated in the legend. The different plots show the global coordinates r , ϕ and z on the x-axis, and the position changes Δr , Δz and $r\Delta\phi$ on the y-axis [51].

(DMRs) is a useful check of the average improvement brought by the performed alignment on each subdetector. Each module is considered individually in these validations, and a hit prediction from each track is obtained after refitting the track using all other hits. The median of the distribution of these unbiased hit residuals is then taken for each module and is histogrammed. DMR validations are made for each of the local x and y coordinates so that different Lorentz drift and other calibration aspects are understood and separated. The width of the DMRs depends on the number of tracks, so it is important in these validations to use choose a consistent number of tracks for comparison between different geometries. The validations for the pixel barrel local y coordinate and the strip endcaps, run over a subset of the 2016 data, are shown in Fig. 2.10 to illustrate the overall effect of alignment on the full dataset [51].

Muons from cosmic rays, which come from the upper atmosphere, can be used in both alignment and its validation. These energetic muons pass through the different sections of the tracker and constraint the position of modules along different lines that do not originate from the interaction point. Example distributions of the different momentum coordinates of these tracks is shown in Fig. 2.11 from the validations during the commissioning of the tracker [52]. These tracks can be either used in alignment or in the validation of the improvements in track parameter resolution after an alignment. In the case of validation, the upper and lower portions of the cosmic tracks are reconstructed independently, and the difference between the upper and lower halves in track parameters at the point of closest approach to the beam spot

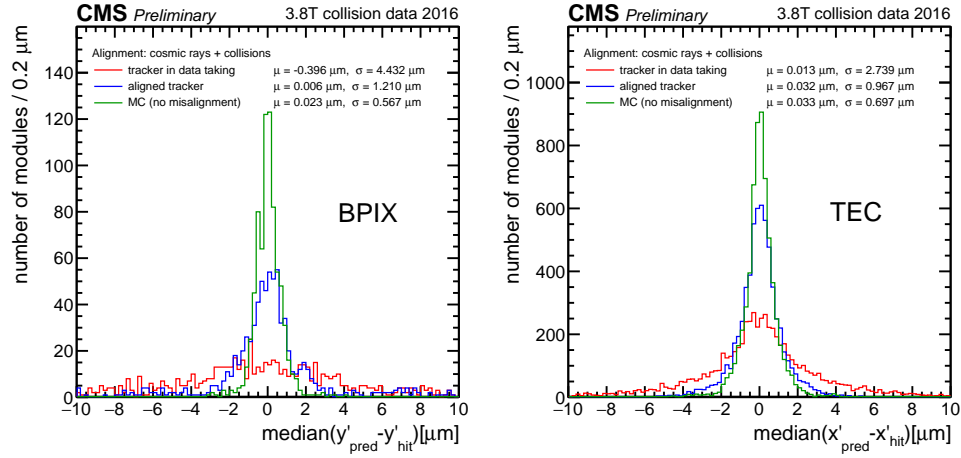


Figure 2.10: DMRs are shown with 1 million collision events collected at 3.8 T magnetic field for the pixel barrel local y coordinate (left) and the strip endcaps (right). The red histograms show the status at the time of data taking, and the blue histograms show the median distributions after a combined alignment with the MILLEPEDE II and HipPy algorithms which is also derived using collision and cosmics data at 3.8 T magnetic field. For comparison, the green histogram shows the DMRs for a reference distribution from simulation with no mis-alignment [51].

are then examined to quantify the effect of alignment. An example track parameter validation is shown in Fig. 2.12.

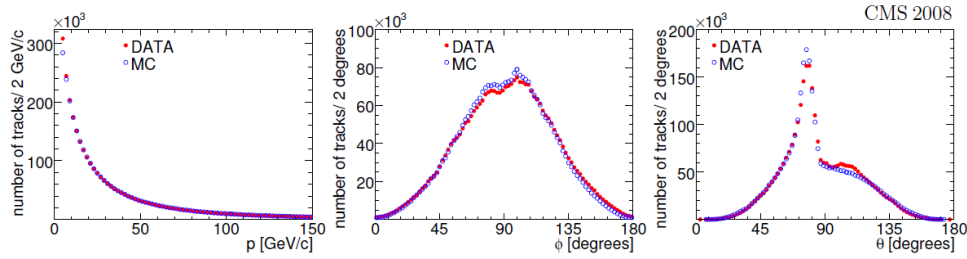


Figure 2.11: The distribution of track momentum (left), and azimuthal (middle) and polar (right) angles are shown for the cosmic muons reconstructed in the CMS tracker volume. The solid red circles represent the data whereas the open blue circles represent the simulation. The vertical direction corresponds to $\phi = \theta = 90^\circ$. The asymmetry around $\phi = 90^\circ$ occurs due to an excess of positively charged particles relative to negatively-charged ones, bending in opposite directions in the magnetic field of the solenoid. The asymmetry around $\theta = 90^\circ$ occurs due to the location of the cavern shaft [52].

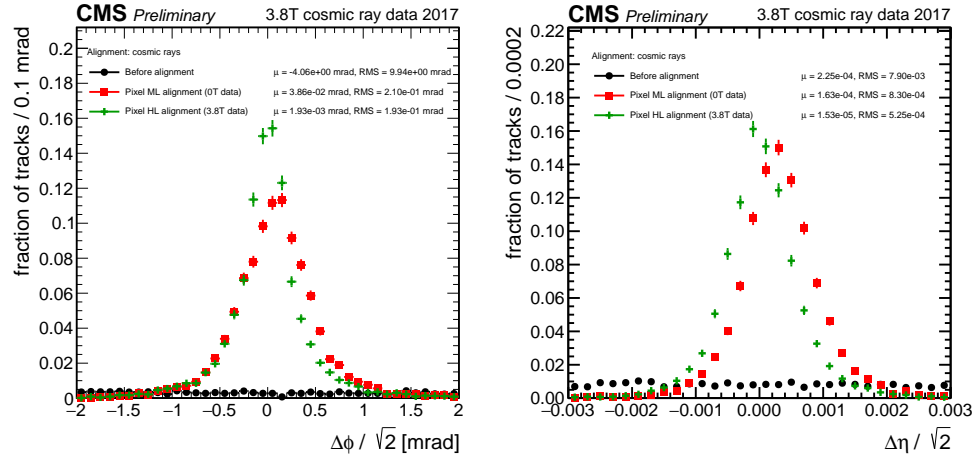


Figure 2.12: Differences between the upper and lower track segment parameters measured at the closest point of approach to the beam spot are shown with a scale of $1/\sqrt{2}$. The shown quantities are the distance of closest approach $\delta\phi$ (left) and $\delta\eta$ (right). The three geometries illustrated are initial 2017 geometry before alignment (black circles), after an alignment of the pixel detector at the level of modules with cosmic ray events recorded at 0 T magnetic field (red squares), and after alignment of higher level pixel detector components with cosmic ray events recorded at 3.8 T (green crosses) [46].

Among each of the interaction vertices around the interaction point in a single event, one of the vertices is usually tagged as primary. These primary vertices (PV) correspond to the reconstructed vertex with the largest value of p_T^2 individually summed over charged-particle tracks (including jets clustered using the jet finding algorithm [53, 54] in Run 2). Tracks originating from this vertex can be randomly taken out to refit this vertex and observe the average impact parameter changes between the track and the refit PV as a function of the angular direction of these tracks. The effect of misalignments are usually observed as average deviations from null as a function of these angular directions of tracks taken out. A typical PV validation performed over minimum bias events is shown in Fig. 2.13. The information from the PV validation can be incorporated into the alignment directly by introducing the unbiased primary vertex as a effective hit during the fit of tracks.

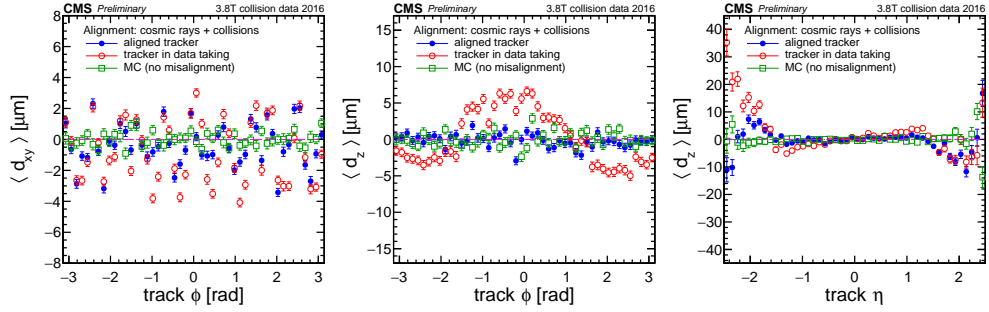


Figure 2.13: The distance in the transverse, d_{xy} (left) and longitudinal, d_z (middle), plane of the track at its closest approach to a refit unbiased primary vertex in bins of the track azimuthal angle ϕ , or d_z in bins of the track pseudorapidity η . A sample of 250,000 collision events collected in 2016 are used. The performance of a dedicated alignment using cosmic ray and collision data at 3.8 T is compared to the alignment used during data taking. The step feature in the distribution in case of the latter geometry is attributed to a relative shift in global z direction of the two pixel half barrels, which are separated at $\phi = \pm\pi/2$ [51].

Resonances such as J/ψ and Y mesons or the Z boson produce copious

amounts of muon track pairs, and the invariant mass of the dimuon system, or the common vertex from which these two tracks originate, can be used as an additional constraint in alignment or as a valuable tool in validation. Certain movements (weak modes) in the tracker may leave the χ^2 in Eqn. 2.2 unchanged. Dimuons from the Z boson are helpful in constraining some of these weak modes in the strips, where charge-symmetric effects on the muon tracks such as an elliptical distortion ($\Delta r \sim \phi$) or charge-asymmetric effects such as a twist ($\Delta \phi \sim z$) can occur. Monitoring the dimuon mass as a function of the angular direction of each muon track is also important since $Z \rightarrow \mu\mu$ events are typically used to calibrate muon momenta, using the mass of the Z boson as external information. A typical validation from $Z \rightarrow \mu\mu$ events is shown in Fig. 2.14 for the 2017 data taking period. Constraints from such resonances can be introduced in the same way as in PV constraints, by introducing the common dimuon vertex as a common effective hit during the fit of the two muon tracks. The mass constraint can further be incorporated if the two muon tracks are parameterized as a single, broken track.

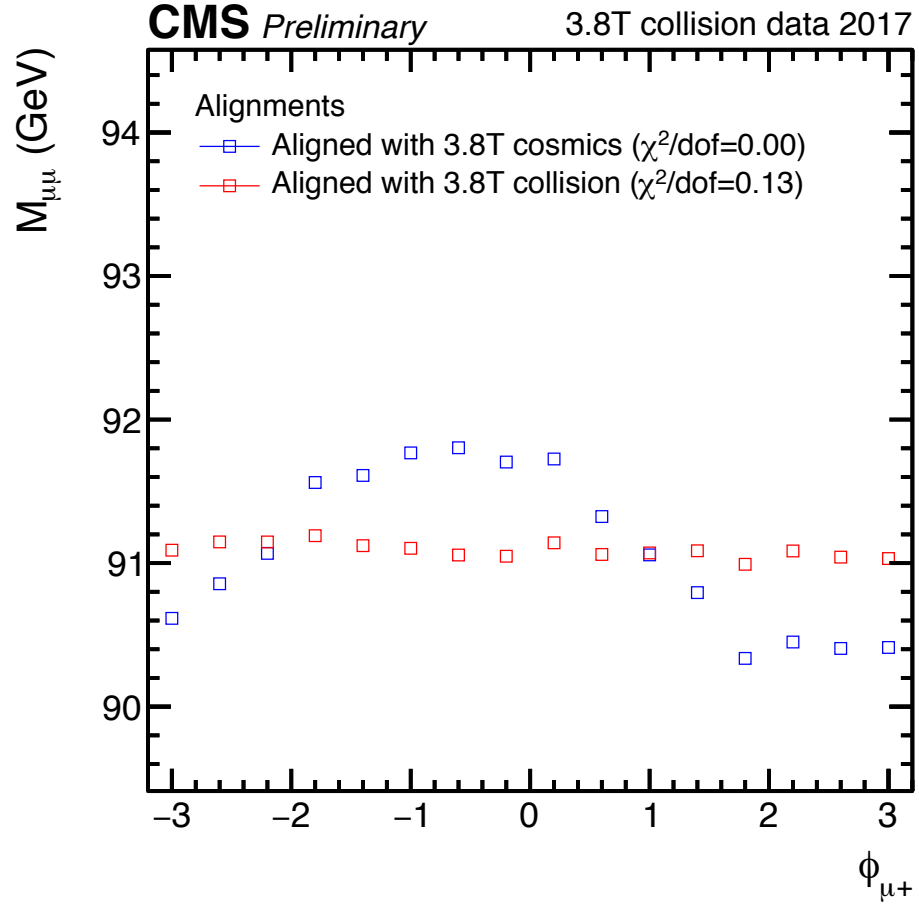


Figure 2.14: Comparison of reconstructed dimuon mass from $Z \rightarrow \mu\mu$ events between the geometry used during 2017 data taking and the geometry after alignment. The dimuon mass is shown in bins of the azimuthal angle ϕ of the positively charged track [55].

2.2.3 The electromagnetic calorimeter and the preshower

The ECAL is a sampling calorimeter providing coverage up to pseudorapidity $|\eta| = 3$. It utilizes 75848 lead tungstate crystals (PbWO_4), which are high in density (8.28 g/cm^3) and short in radiation length (0.89 cm). The crystals emit about 80% of the scintillation light within the LHC bunch crossing time of 25 ns. Each crystal in the barrel ($|\eta| < 1.479$) is 23 cm long with a front face area of $2.2 \times 2.2 \text{ cm}^2$, and each one in the endcap regions is 22 cm long with a front face area of $2.47 \times 2.47 \text{ cm}^2$. They emit blue-green light (420-430 nm), and the light is converted to electric current with about 4.5 photoelectrons per MeV at 18°C by silicon avalanche photodiodes (APDs) in the barrel and vacuum phototriodes (VPTs) in the endcaps [40]. Under irradiation, the ECAL loses transparency. The loss is partially recovered when radiation exposure stops, but the net effect is that the response of the crystals varies with time. the variation is being monitored by a laser system [56], and it was observed starting from 2012 that offline corrections to the energy need to be applied on a weekly basis [57, 58]. The dependence of the energy response of the ECAL as a function of integrated luminosity is shown in Fig. 2.15.

A preshower system is installed in front of the endcap ECAL, in the region $1.653 < |\eta| < 2.6$ for π^0 rejection. This preshower system is a sampling calorimeter consisting of two layers of lead radiators to initiate electromagnetic showers from incoming photons or electrons and silicon strip sensors placed after each radiator to measure the deposited energy and the transverse shower profiles. The material thickness of the preshower traversed at $|\eta| = 1.653$ before reaching the first silicon sensor plane is 2 radiation lengths (i.e. mean

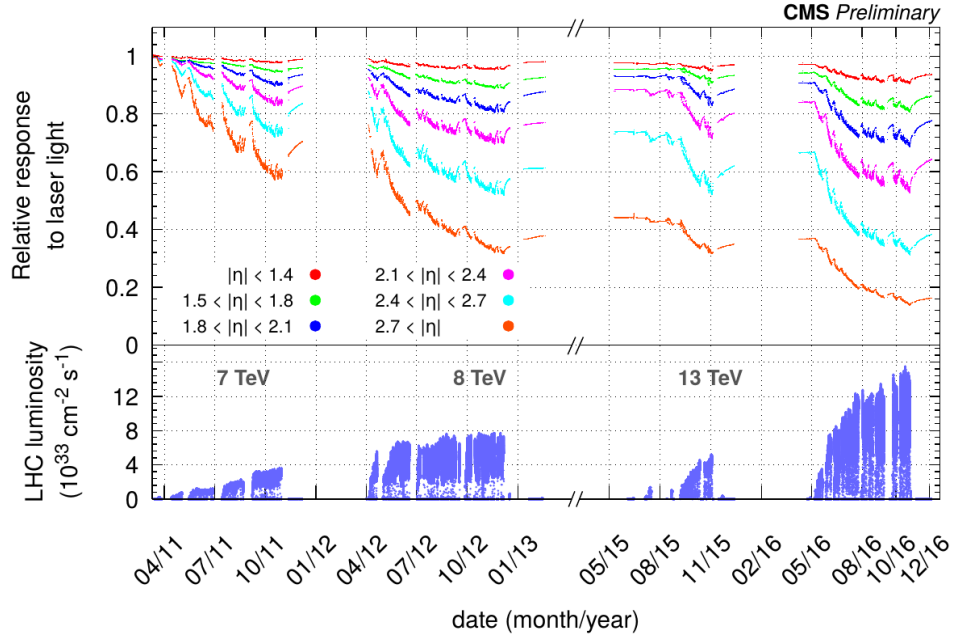


Figure 2.15: Relative response to laser light (440 nm in 2011 and 447 nm from 2012 onward) measured by the ECAL laser monitoring system, averaged over all crystals in bins of pseudorapidity for the 2011, 2012, 2015 and 2016 data taking periods. The response change observed in the ECAL channels is up to 10% in the barrel, and while it reaches up to 50% at $|\eta| \sim 2.5$, the edges of the tracker. The response change is up to 90% in the region closest to the beam pipe. The recovery of the crystal response during the Long Shutdown 1 period (2013, 2014 and first half of 2015) is visible, where the response was not fully recovered, particularly in the region closest to the beam pipe. These measurements are used to correct the physics data. The bottom plot shows the instantaneous LHC luminosity delivered during this time period up to November 2016. [58].

distance λ_0 over which $1 - 1/e$ amount of an electron's initial energy is lost), followed by another $1 \lambda_0$ before reaching the second plane. This arrangement ensures about 95% of incident photons from the neutral pions start to shower before the second sensor plane. The total thickness of the preshower is 20 cm [40].

2.2.4 The hadronic calorimeter

The HCAL plays a central role in the measurement of hadronic energy deposits, which are typically in a cone of certain radius and are called jets, and jet direction. It is also utilized to provide an estimate of missing transverse energy in each event. The barrel (HB) and endcap (HE) regions surround the ECAL, provide coverage up to $|\eta| = 3$, and are made out of plastic scintillators interleaved with brass absorber material. The emitted light is converted by wavelength shifting fibers embedded in the scintillator tiles and channeled via clear fibers for readout to hybrid photodiodes (HPDs) that can operate in high axial magnetic fields. This central calorimetry is complemented by a tail-catcher outer component (HO) in the barrel region insuring that hadronic showers are sampled with nearly eleven interaction lengths and helping muon identification. The HO uses the steel return yoke as the absorber instead of the brass material in the barrel and endcaps. Coverage up to $|\eta| = 5.3$ is provided by an iron/quartz-fiber Cherenkov calorimeter (HF). The Cherenkov light emitted in the quartz fibers is detected by photomultiplier tubes (PMTs). The HF ensures nearly full geometric coverage for measurement of the transverse energy in the event [40]. The HF PMTs were upgraded as part of the Phase-I upgrade operations to use multi-anode output to have timing more compatible with 25 ns bunch crossings, and the HPDs in HB and HE are replaced by silicon photomultipliers (SiPMs) to reduce the operating voltage and reduce high-amplitude noise [59].

2.2.5 The muon system

The CMS muon system is designed to have the capability of reconstructing the momentum and charge of muons over a large muon p_T range and $|\eta| < 2.4$ with 95–99% efficiency. Three types of gaseous particle detectors are present in this system: Drift tube (DT) chambers, cathode strip chambers (CSCs) and resistive plate chambers (RPCs). An alignment algorithm similar to that of the tracker measures the positions of the muon detectors with respect to each other and the inner tracker to optimize the muon reconstruction efficiency and momentum resolution.

Background from neutrons and the overall muon rate is low in the barrel region. The magnetic field is also uniform and mostly contained in the steel yoke. For this reason, drift chambers with rectangular drift cells are used, covering the pseudorapidity region $|\eta| < 1.2$. They are organized into four stations interspersed among the layers of the flux return plates. The first three stations each contain eight chambers in groups of four, which measure the muon coordinate in the $r - \phi$ plane, and four chambers which provide a measurement in the z direction along the beamline. The fourth station does not contain the z -measuring planes. The two sets of four chambers in each station are separated as much as possible to achieve the best angular resolution. The drift cells of each chamber are offset by a half-cell width with respect to their neighbor to eliminate dead spots in the efficiency. This arrangement also provides a convenient way to measure the muon time with excellent time resolution for efficient, standalone bunch crossing identification. The number of chambers in each station and their orientation were chosen to provide good

efficiency for linking together muon hits from different stations into a single muon track and for rejecting background hits.

In the two endcap regions, muon rates and background levels are high, and the magnetic field is large and non-uniform. With fast response time, fine segmentation, and radiation resistance, the CSCs employed in these regions identify muons between $0.9 < |\eta| < 2.4$. Four CSC stations interspersed between the flux return plates are positioned perpendicular to the beam line in each endcap. The cathode strips in each chamber run radially outward and provide a precision measurement in the $r - \phi$ plane. The anode wires run approximately perpendicular to the strips and are also read out in order to provide measurements of η and the beam-crossing time of a muon. Each 6-layer CSC provides robust pattern recognition for rejection of non-muon backgrounds and efficient matching of hits to those in other stations and to the CMS inner tracker.

The DT and CSC subsystems can each trigger on the p_T of muons with good efficiency and high background rejection, independent of the rest of the detector. However, because of the uncertainty in the eventual background rates and in the ability of the muon system to measure the correct beam-crossing time when the LHC reaches full luminosity, a complementary, dedicated trigger system consisting of RPCs was added in both the barrel and endcap regions. The RPCs provide a fast, independent, and highly-segmented trigger with a sharp p_T threshold over the rapidity range $|\eta| < 1.6$. The RPCs are double-gap chambers, operated in avalanche mode to ensure good operation at high rates. They produce a fast response with good time resolution but coarser position

resolution than the DTs or CSCs. They also help to resolve ambiguities in attempting to make tracks from multiple hits in a chamber.

2.3 The trigger system

The collision rate exceeds 1 GHz at the design luminosities of the LHC. A small fraction of these collisions contain events of interest to the CMS physics program, and only a small fraction of those interesting events can be stored for later offline analysis. Reconstruction is also computationally costly, so it is desirable to dedicate the limited computing resources to the reconstruction and identification of particles (i.e. physics objects such as muons, electrons and jets) in the interesting events. For this reason, it is the job of the trigger system to select the interesting events for offline storage from the bulk of the inelastic collision events, and the offline reconstruction algorithms to reconstruct and identify the particles.

The CMS trigger utilizes two levels. The first level (L1) is based on customized hardware, which selects events containing candidate objects such as ionization deposits consistent with a muon, or energy clusters consistent with an electron, photon, τ lepton, E_T^{miss} or jet. The thresholds of L1 are adjusted during data taking in response to the value of the LHC instantaneous luminosity so as to restrict the output rate to the upper limit imposed by the CMS readout electronics, 100 kHz [61]. A schematic view of the L1 trigger is shown in Fig. 2.16.

The two LHC beam position monitors closest to the interaction point for each LHC experiment are reserved for timing measurements and are called

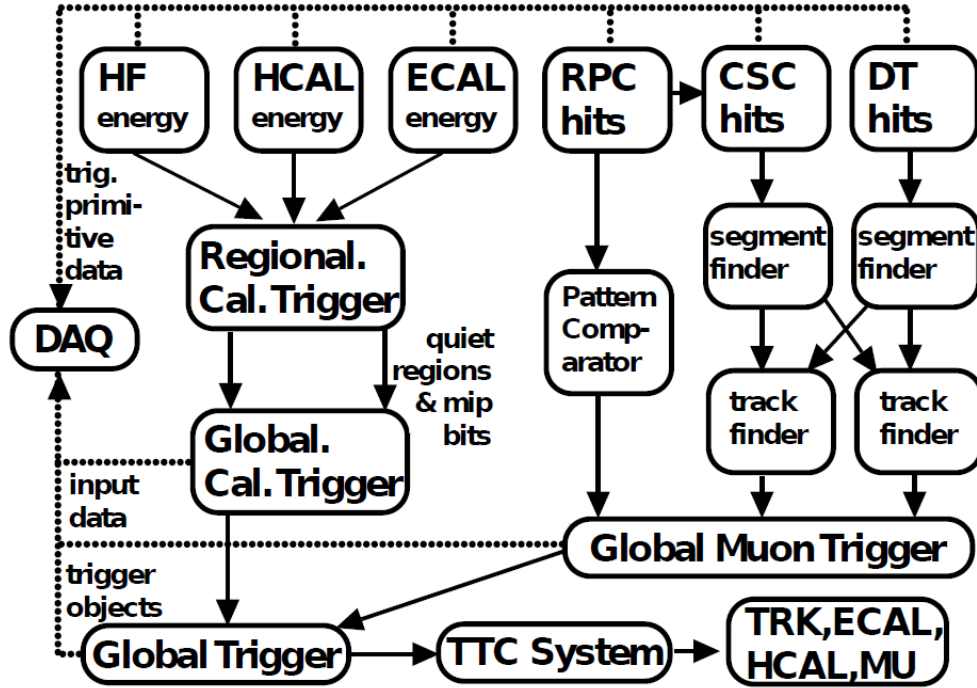


Figure 2.16: Overview of the CMS L1 trigger system. Data from the HF, HCAL and ECAL are processed first regionally (RCT) and then globally (GCT). Energy deposits (hits) from the muon systems are processed either via a pattern comparator or a system of segment and track finders, and this information is then sent to a global muon trigger (GMT). The information from the GCT and GMT is combined in a global trigger (GT), which makes the final trigger decision. This decision is sent to the tracker (TRK), ECAL, HCAL or muon systems (MU) via the trigger, timing and control (TTC) system. The data acquisition system (DAQ) reads data from various subsystems for offline storage [60].

the beam pick-up timing experiment (BPTX) detectors. For CMS, they are located at a distance of approximately 175 m on either side of the interaction point (BPTX+ and BPTX-). This trigger selects valid bunch crossings using the digitized BPTX signal by requiring a coincidence of the signals from the detectors on either side. HF also features pre-firing caused by particles interacting with the photomultiplier anodes rather than the detector itself, and BPTX is also utilized in vetoing events of this kind.

The final event selection is based on the high-level trigger (HLT), a programmable menu in which up to 128 algorithms decide whether the events containing the candidate objects are interesting for physics. The HLT implemented in software further refines the purity of the physics objects and selects an average rate of 400 Hz for offline storage. Selections relying on information from the calorimeters and the muon systems reduce the event rate before the CPU-intensive tracking reconstruction is performed. The reconstruction modules and selection filters of the HLT use the software framework that is also used for offline reconstruction and analyses, but more rigorous timing constraints are imposed due to the limited number of CPUs available for the HLT. The overall output rate of the L1 trigger and HLT can be adjusted by prescaling the number of events that pass the selection criteria of specific algorithms.

After passing trigger, accepted events are sent to the storage manager for archival storage. The event data are stored locally on disk and eventually transferred to the CMS Tier-0 computing center for offline processing and permanent storage. Events are grouped into a set of non-exclusive streams

according to the HLT decisions. Most data are processed as soon as possible, but CMS also has the capability to delay the processing of certain lower-priority data streams (parking). The parking ability increases the amount of data CMS can store on tape, albeit with a longer latency [60].

2.4 Identification of particles and $H \rightarrow 4\ell$ event candidates

2.4.1 Identification of physics objects using the particle-flow algorithm

The strategy to identify the particles in the CMS detector is driven by the order in which the resolution for the position and energy of the objects is better, so identification, in the coarser sense, starts with muons and proceeds toward electrons and photons, and then jets. The simplest approach to identify muons in CMS is to use the information primarily in the muon systems, and likewise for electrons and isolated photons, to use the information from the ECAL. Jets could be identified similarly from the information in the calorimeters, and tagging the jets for the different quark flavors or gluons, or the identification of the τ lepton, could be achieved by matching the calorimeter energy deposits to charged particle tracks in the tracker. The particle-flow (PF) algorithm [62–64] improves the event description by correlating the basic particle reconstruction elements, tracks and energy clusters, from all detector layers to identify each final-state particle, and by combining these measurements to reconstruct the particle properties on the basis of this identification.

Reconstructing tracks is achieved with a combinatorial track finder [65,

[66] based on Kalman filtering [67–70]. In the magnetic field of the tracker, charged particles follow helical paths that are described by five parameters, and extraction of these five parameters requires either three hits that provide three-dimensional information, or two 3-D hits and a constraint on the origin of the trajectory based on the assumption that the particle originated near the beam spot. The initial hits are used as seeds to later identify an initial trajectory to extrapolate. Hits are then found along the expected trajectory via a Kalman filter algorithm, and the parameters of each trajectory are estimated by an iterative Kalman filter and smoother fit. Finally, track quality flags are determined based on various selection criteria, and those that fail these criteria are discarded [66].

Clustering is performed separately in each subdetector: ECAL barrel and endcaps, HCAL barrel and endcaps, and the two preshower layers. In the HF, no clustering is performed; the electromagnetic or hadronic components of each cell directly give rise to a cluster. Cluster seeds are identified as cells with energy larger than a given threshold and the energy of the neighboring cells. The cells considered as neighbors are either the four closest cells that share a side with the seed candidate, or the eight closest cells including cells that only share a corner with the seed candidate. Topological clusters are then accumulated from the seeds by aggregating cells with at least a corner in common with a cell already in the cluster and with an energy in excess of a cell threshold set to twice the noise level. In the ECAL endcaps, the noise level increases as a function of $|\eta|$, so seeds in these subdetectors are additionally required to satisfy a transverse energy requirement. A Gaussian sum model

is then applied to determine the final cluster parameters.

Identification of muons proceeds by first selecting isolated muons by considering tracks and calorimeter energy deposits with a distance $\Delta R = \sqrt{\eta^2 + \phi^2} < 0.3$ to the muon direction. The sum of the p_T of the tracks and of the transverse energy of the deposits is required not to exceed 10% of the muon p_T . For non-isolated global muons, such as muons inside a jet, tighter muon selection criteria are applied. For these types of muons, it is also required that either three or more matching track segments be found in the muon detectors, or the calorimeter deposits associated with the track be compatible with a muon hypothesis. This requirement removes the majority of high- p_T hadrons misidentified as muons as well as accidental associations of tracker and standalone muon tracks. Muons that fail the tight-muon selection due to a poorly reconstructed tracker track may still pass muon identification if the standalone track in the muon system is of high quality and is associated with a large number of hits in the muon detectors. Alternatively, muons may also fail the tight-muon selection due to a poor global track fit. In this case, the muon is still selected if a high-quality fit is obtained with at least 13 hits in the tracker, and if the associated calorimeter clusters are compatible with a muon hypothesis. The final momentum of the muon is chosen to come from the tracker-only track fit if the muon p_T is less than 200 GeV. Otherwise, different versions of track fits involving the tracker hits are compared, and the one with the lowest χ^2 is used to pick the muon p_T value.

Electron and photon identification is based on the information from the inner tracker and the calorimeters. Due to the material in the tracker, electrons

often emit bremsstrahlung photons, and these photons often convert to e^+e^- pairs. Isolated photon reconstruction is therefore conducted together with electron reconstruction. An electron candidate is first seeded from a Global-sum filter (GSF) track [71], which is more adapted to fit tracks for electrons, if the corresponding ECAL cluster is not linked to three or more additional tracks. A photon candidate is seeded from an ECAL supercluster with transverse energy larger than 10 GeV, with no link to a GSF track. For ECAL-based electron and photon candidates, the sum of the energies measured in the HCAL cells with a distance $\Delta R < 0.15$ to the supercluster must not exceed 10% of the supercluster energy. Tracks linked to the ECAL clusters are associated as well if the track momentum and the energy of the HCAL cluster linked to the track are compatible with the electron hypothesis. The tracks and ECAL clusters belonging to identified photon conversions linked to the GSF track tangents are associated as well. Electron candidates must satisfy additional identification criteria. Up to fourteen variables related to how radiation occurs out of the GSF tracks and energy measurements in ECAL and HCAL are combined in boosted decision trees, which are trained separately for the ECAL barrel and endcaps, and for isolated and non-isolated electrons. Photon candidates, on the other hand, are retained if they are isolated from other tracks and calorimeter clusters, and if the ECAL cell energy distribution and the ratio between the HCAL and ECAL energies are compatible with those expected from a photon shower.

Once muons, and isolated electrons and photons are identified, the remaining particles are used to identify hadrons, which appear as non-isolated

photons, charged or neutral hadrons. Within the tracker acceptance, 25% of jet energy is dissipated via photons in the ECAL while only 3% is dissipated via neutral hadrons. Therefore, all ECAL clusters not linked to a tracker track within this acceptance are identified as photons while all HCAL clusters without a tracker track within this acceptance are identified as neutral hadrons. Outside tracker acceptance, neutral and charged hadrons cannot be distinguished, so the precedence in ECAL for photons is no longer valid. Instead, ECAL clusters linked to a given HCAL cluster are assumed to arise from the same charged or neutral hadron shower while ECAL clusters without such a link are classified as photons. The remaining HCAL clusters are linked to one or several tracks not linked to any other HCAL cluster to determine if they satisfy charged hadron criteria [62].

2.4.2 $H \rightarrow 4\ell$ candidate selection

The ultimate goal of reconstructing and identifying physics objects is to search for a certain collection of particles, which may be produced as a result of the decay of an intermediate particle or be completely a new, stable particle. Since this thesis is mainly focused on probing the properties of the H boson by analyzing 4ℓ decay products and associated jets, we describe here how muons, electrons and jets identified in each event are ultimately selected for further assessment. Further specific details can be found in Refs. [72] for Run 1 selection criteria, [73] for 2015 Run 2 data period criteria, [74] for 2016 Run 2 data period criteria, and [75] for 2017 Run 2 data period criteria.

The main triggers of this analysis select a pair of electrons or muons, or

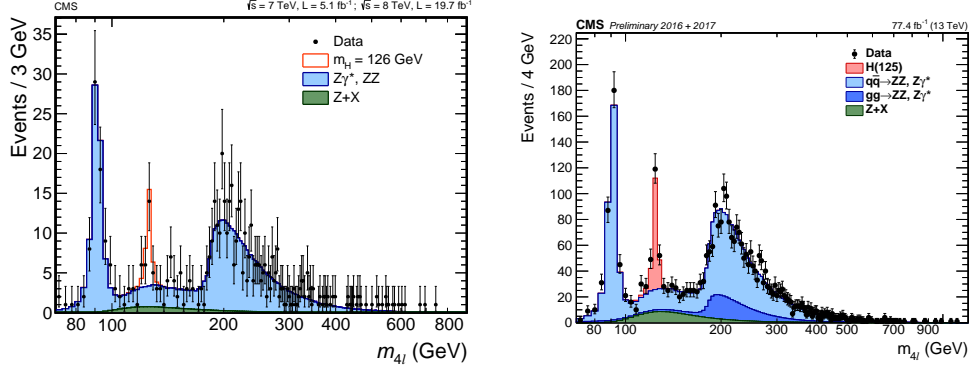


Figure 2.17: Distribution of four-lepton events as a function of $m_{4\ell}$ from Run 1 (left) [72] and Run 2 (right) [75] data taking periods. Each shaded histogram illustrates the additional background contribution expected from simulation, except for the red histogram that shows the expected contribution from H boson events with the assumption $m_H = 126$ or 125 GeV. The dark points with Poisson error bars show the observation from the data. The integrated luminosity to which data from each period corresponds is written at the top right corner of the plots.

an electron and a muon. During Run 1 data taking, the minimal p_T of the leading and subleading electrons or muons are required to be 17 and 8 GeV, respectively. During Run 2, this requirement is altered for the leading electron (muon) to be 23 (17) GeV, and for the subleading lepton to be 12 (8) GeV. In Run 1, a triple-electron trigger is added with thresholds of 15, 8, and 5 GeV to increase the efficiency for low- p_T electrons in the $4e$ final state. Similarly in Run 2, triggers requiring three leptons with low p_T thresholds and no isolation requirement are also used, and isolated single-electron and single-muon triggers, with the thresholds of 27 GeV and 22 GeV in 2016, and 35 GeV and 27 GeV in 2017 respectively, are also added. In addition to the events selected to form the four-lepton sample, dedicated triggers are used for lepton calibration and efficiency measurements. In the case of dimuon events, the online trigger algorithms used to select the signal events are sufficiently loose

that they can also be used to measure the selection efficiency with the $Z \rightarrow \mu^+ \mu^-$ events. In order to measure the selection efficiency of events with low- p_T leptons, low-mass resonances are used. Events corresponding to these low-mass resonances are collected in the dimuon case using dedicated triggers that require an opposite-sign muon pair, with dedicated kinematic conditions on the dimuon system. In the case of electrons, low-mass resonances are collected, with a smaller rate, with standard dielectron triggers. Two specialized triggers are introduced to maximize the number of $Z \rightarrow e^+ e^-$ events covering both high- and low- p_T ranges.

Electron candidates passing trigger requirements are required to have a transverse momentum $p_T > 7$ GeV and be within the geometrical acceptance, defined by $|\eta| < 2.5$. Muon candidates are required to have a transverse momentum $p_T > 5$ GeV and within $|\eta| < 2.4$. Lepton isolation is used to discriminate leptons originating from high- p_T boson decays, as in the case of the signal, from those arising from hadronic processes, which are typically immersed in jets from other hadrons. The isolation of individual leptons is measured relative to their transverse momentum and is defined by

$$R_{\text{Iso}}^\ell = \left(\sum p_T^{\text{charged}} + \max [0, \sum p_T^{\text{neutral}} + \sum p_T^\gamma - p_T^{\text{PU}}(\ell)] \right) / p_T^\ell, \quad (2.2)$$

where the sums are over charged and neutral PF candidates in a cone $\Delta R < 0.4$ in Run 1, and < 0.3 in Run 2, around the lepton direction at the interaction vertex. The contribution from pileup ($p_T^{\text{PU}}(\ell)$) in the isolation cone is subtracted from R_{Iso}^ℓ with different techniques for electrons and muons. In Run 1 selection, electrons or muons are considered isolated if $R_{\text{Iso}}^\ell < 0.4$. In Run 2

2015 and 2016 data periods, the requirement is tightened to $R_{\text{Iso}}^\ell < 0.35$ for both muons and electrons, and in the 2017 data, the R_{Iso}^ℓ is already included as part of the BDT input for electron identification, so this requirement is only applied on muons.

To suppress leptons originating from in-flight decays of hadrons and electrons from photon conversions, we require each lepton track to have the ratio of the impact parameter in three dimensions, computed with respect to the chosen primary vertex position, and its uncertainty (i.e. the significance of the 3-D impact parameter, $\text{SIP}_{3\text{D}}$) to be less than 4. This requirement is changed in the lifetime analysis of the H boson as described in Section 4.2 because an impact parameter requirement with respect to the primary vertex biases the selection against large H boson lifetime.

Final-state radiated photons (FSR photons) are mostly produced with a direction nearly collinear with the parent lepton and have a harder spectrum than background photons from initial-state radiation or pileup interactions. Up to 9% of events in $\text{H} \rightarrow 4\ell$ decay also have an associated FSR photon, and the energy dissipated by the photon needs to be accounted for a more optimal reconstruction of the 4ℓ invariant mass, $m_{4\ell}$. The requirements for identifying a photon as FSR from a lepton is slightly different between Run 1 and Run 2 data periods.

In Run 1, a photon isolation observable R_{Iso}^γ is defined in a similar way to R_{Iso}^ℓ as the sum of the transverse momenta of any charged hadrons, other photons, and neutral hadrons identified by the PF reconstruction within $\Delta R = 0.3$ around the candidate photon direction, divided by the photon transverse

momentum. Isolated photons are first identified with the requirement $R_{\text{Iso}}^\gamma < 1$. A reconstructed photon must either have a transverse momentum $p_T^\gamma > 2$ GeV and be found within a cone of size $\Delta R < 0.07$ from a selected lepton candidate, or have $p_T^\gamma > 4$ GeV and be found isolated from charged particles and energy deposits and within $0.07 < \Delta R < 0.5$ from a selected lepton candidate. In case more than one FSR candidate is associated with a Z candidate, the one with the highest p_T^γ is chosen if that photon has $p_T^\gamma > 4$ GeV. Otherwise, the one closest to any of the individual daughter leptons of the Z-boson candidate is chosen, and the chosen photon is associated to the Z boson if the invariant mass of the lepton pair and the photon is less than 100 GeV.

In Run 2, photons reconstructed by the PF algorithm within $|\eta_\gamma| < 2.4$ are considered as FSR candidates if they pass $p_T^\gamma > 2$ GeV and $R_{\text{Iso}}^\gamma < 1.8$. Every such photon is associated first to the closest selected lepton in the event, and those that do not satisfy $\Delta R(\gamma, \ell)/(p_T^\gamma)^2 < 0.012 \text{ GeV}^{-2}$ and $\Delta R(\gamma, \ell) < 0.5$ are discarded. For each lepton, the photon candidate with the lowest $\Delta R(\gamma, \ell)/(p_T^\gamma)^2$ value are retained as the identified FSR and are associated with that lepton. Photons identified as FSR are excluded from any isolation computation.

Jets are reconstructed from PF candidates, clustered by the anti- k_T algorithm [53, 54] with a distance parameter ΔR of 0.5 in Run 1. In Run 2, the distance parameter is taken to be 0.4. and the constraint that the charged particles are compatible with the primary vertex are added. The jet momentum is determined as the vector sum of all particle momenta in the jet, and is found in the simulation to reproduce the true momentum at the 5 to 10%

level over the whole p_T spectrum and detector acceptance. Corrections on the jet energy scale (JEC) are derived from the simulation and confirmed with measurements examining the energy balance in dijet, multijet, $\gamma + \text{jet}$, and leptonic $Z/\gamma + \text{jet}$ events [76, 77]. Jet energies in simulation are smeared to match the resolution in data. To be considered in the analysis, jets must satisfy $p_T^{\text{jet}} > 30 \text{ GeV}$ and $|\eta^{\text{jet}}| < 4.7$, and be separated from all selected lepton candidates and any selected FSR photon by $\Delta R(\ell/\gamma, \text{jet}) > 0.5$ in Run 1 and > 0.4 in Run 2. Some of the event categorization also uses b-tagging. Jets are tagged as b-jets using the Combined Secondary Vertex algorithm [78–80], which combines information about the impact parameter significance, the secondary vertex and the jet kinematics.

The 4ℓ event selection features at least four isolated leptons, each of which originates from the primary vertex and is possibly accompanied by an FSR photon candidate. FSR photons are included in invariant mass computations in the following discussion of event selection.

The event selection starts with the identification of the Z boson candidates with decay to two opposite sign (OS), same-flavor lepton pairs. The invariant mass of the lepton pair is required to pass $12 < m_{\ell+\ell^-} < 120 \text{ GeV}$. The Z boson candidates are then combined into ZZ pairs, wherein Z_1 denotes the Z candidate with an invariant mass closest to the nominal Z boson mass m_Z and Z_2 denotes the remaining one. Multiple ZZ pairs may be present in the candidate if more than two Z bosons are identified, but the selection logic takes into account all possible pairs in this case before discarding the event. The Z_1 invariant mass is required to be larger than 40 GeV. All leptons

must be separated in angular space by at least $\Delta R(\ell_i, \ell_j) > 0.02$. At least two leptons are required to have $p_T > 10$ GeV, and at least one is required to have $p_T > 20$ GeV. For $Z_1 Z_2$ candidates composed of four same flavor leptons, an alternative pairing $Z_a Z_b$ can be formed out of the same four leptons. In the Run 2 selection, the $Z_1 Z_2$ pair is discarded if $m(Z_a)$ is closer to m_Z than $m(Z_1)$ and $m(Z_b) < 12$ GeV. This protects against events that contain an on-shell Z and another low-mass dilepton resonance. To further suppress events with leptons originating from hadron decays in jet fragmentation or from the decay of low-mass hadronic resonances, all four OS lepton pairs that can be built with the four leptons, irrespective of their flavor, are required to satisfy $m_{\ell+\ell'-} > 4$ GeV, where selected FSR photons are disregarded in the computation of this particular invariant mass quantity. Finally, the four-lepton invariant mass $m_{4\ell}$ is required to be larger than 70 GeV. The final $m_{4\ell}$ distributions of Run 1 and Run 2 events are shown in Fig. 2.17.

Chapter 3

The Phenomenology of the Higgs Boson at the LHC

The observation of an H boson with the mass around 125 GeV by the ATLAS and CMS Collaborations [81–83] is consistent with the expectations of the SM. There have been several experimental and theoretical observations made to this date about this recently discovered boson:

1. It decays to two on-shell photons [81, 82, 84, 85], so it cannot have spin 1 by the Landau-Yang theorem [86, 87].
2. Spin-1 and spin-2 assignments, and a purely spin-0, negative parity hypothesis are also strongly disfavored by the measurement of angular distributions in $H \rightarrow ZZ$ and $H \rightarrow WW$ decays [72, 88–91]. Therefore, the particle appears to be predominantly a $J^{PC} = 0^{++}$ state. Nevertheless, spin-0 mixture states with small anomalous components have not yet been constrained tightly.
3. About 10% of $H \rightarrow VV$ ($V = Z$ or W) decay events at the current center of mass energies of the LHC occur in the SM when the H boson is produced

off-shell, with large interference effects between the H boson-mediated signal and the continuum background [92–96]. It has been proposed that an enhancement of these off-shell events can be used to constrain the H boson total width in a tighter way than on-shell measurements from the resonance peak. It has also been pointed out that off-shell H boson decay may also be enhanced in the presence of anomalous HVV couplings [97–99].

In light of these observations, it is equally important to examine the kinematics of the decay products related to the H boson just as well as the location of the resonance peak to measure its mass in order to learn if it is possible to find small anomalous couplings that might deviate from higher order perturbative corrections in the SM. It is also important to look at the shape of the off-shell H boson production tail together with other kinematic properties to measure the boson’s total width and infer the effect of any small anomalous couplings. For this reason, we first discuss the anomalous couplings formalism used in this thesis in Section 3.1. We then follow in Section 3.2 with the discussion of H boson production and decay mechanisms relevant for the LHC. We later discuss in Section 3.3 the common simulation and analysis tools used in the analyses presented later in Chapter 4. We finalize this chapter with the discussion of the off-shell method and of how techniques used for the on-shell analyses can be applied to off-shell production as well in Section 3.4. Because the results presented use $H \rightarrow 4\ell$ decay channel almost exclusively, we focus on the methods and tools relevant for this decay channel unless otherwise specified.

3.1 The couplings of a spin-0 resonance

The scattering amplitude between a spin-0 resonance X (e.g. $X = H$) and two spin-one gauge bosons VV ($V = Z, W, \gamma$ or g) can have only three possible Lorentz-invariant terms. Ignoring additional dependencies on the invariant masses of the involved momenta, the amplitude can be written simply as

$$A(XVV) = \epsilon_{V1}^{*\mu} \epsilon_{V2}^{*\nu} [c_1 g_{\mu\nu} + c_2 (q_1 \cdot q_2 g_{\mu\nu} - q_{1,\nu} q_{2,\mu}) + c_3 \epsilon_{\mu\nu\rho\sigma} q_1^\rho q_2^\sigma]. \quad (3.1)$$

Here, ϵ_{Vi} and q_i correspond to the polarization vector and the four-momentum of the boson V_i , respectively, and c_1, c_2 and c_3 are arbitrary coefficients which may depend on other invariant masses. These three terms can be combined with loop form factors or point-like interactions in the scattering amplitude as [100–103]

$$A(XVV) = \frac{1}{v} \left[\sum_{p=f,V'} \kappa_p F_p (\epsilon_{V1}^*, \epsilon_{V2}^*, q_1, q_2 | m_p) + \tilde{\kappa}_p \tilde{F}_p (\epsilon_{V1}^*, \epsilon_{V2}^*, q_1, q_2 | m_p) \right. \\ \left. + a_1'^{VV} m_{V1}^2 \epsilon_{V1}^* \epsilon_{V2}^* + a_2'^{VV} f_{\mu\nu}^{*(1)} f^{*(2),\mu\nu} + a_3'^{VV} f_{\mu\nu}^{*(1)} \tilde{f}^{*(2),\mu\nu} \right]. \quad (3.2)$$

In this amplitude, F_p and \tilde{F}_p are generic functions that include loop form factors of a particle p , which could be either a fermion f or a gauge boson V , and also incorporate scalar and pseudoscalar tensor structure. $f^{(i)\mu\nu} = \epsilon_{Vi}^\mu q_i^\nu - \epsilon_{Vi}^\nu q_i^\mu$, and $\tilde{f}_{\mu\nu}^{(i)} = \frac{1}{2} \epsilon_{\mu\nu\rho\sigma} f^{(i),\rho\sigma}$. V_i are ordered by mass when $V_1 \neq V_2$ (i.e. $VV = Z\gamma$), and $V_1 = W^+$ in the case of $VV = WW$. m_{V1} is the pole mass of the gauge boson V_1 . When the mass of the particle p in the form factors are taken to be very large, $F_p \rightarrow f_{\mu\nu}^{*(1)} f^{*(2),\mu\nu}$ and $\tilde{F}_p \rightarrow f_{\mu\nu}^{*(1)} \tilde{f}^{*(2),\mu\nu}$ with some constant factors that depend on the nature of the particle p .

Equation 3.2 may allow q^2 -dependent $a_i'^{\text{VV}}$ [102]:

$$\begin{aligned}
a_i'^{\text{VV}} &= a_i^{\text{VV}} \delta_{i1} + \left(g_i^\Lambda + a_i^{\text{VV}} (1 - \delta_{i1}) \right) \\
&\times \frac{\Lambda_{i1}^2 \Lambda_{i2}^2 \Lambda_{i3}^2}{(\Lambda_{i1}^2 + c_{i1} |q_1^2|) (\Lambda_{i2}^2 + c_{i2} |q_2^2|) (\Lambda_{i3}^2 + c_{i3} |(q_1 + q_2)^2|)} \\
g_i^\Lambda &= g_i' \frac{\Lambda_i^4}{(\Lambda_i^2 + |q_1^2|) (\Lambda_i^2 + |q_2^2|)} \\
&+ g_i'^2 \frac{(q_1^2 + q_2^2)}{\Lambda_i^2} + g_i'^3 \frac{(q_1^2 - q_2^2)}{\Lambda_i^2} + g_i'^4 \frac{(q_1 + q_2)^2}{\Lambda_Q^2} \\
&+ g_i'^5 \frac{((q_1^2)^2 + (q_2^2)^2)}{\Lambda_i^4} + g_i'^6 \frac{((q_1^2)^2 - (q_2^2)^2)}{\Lambda_i^4} + g_i'^7 \frac{q_1^2 q_2^2}{\Lambda_i^4}, \quad (3.3)
\end{aligned}$$

where the different Λ 's correspond to different BSM scales, $g_i'^j$ are complex scale factors for the different q^2 expansion terms, and $|c_{ij}| = 1$.

For the different cases of $V = Z, W, \gamma$ or g , only a subset of the different terms in Eqns. 3.2 and 3.3 are possible at LO:

1. $\text{VV} = \text{ZZ}$ or WW : Only two of the couplings a_1^{ZZ} and a_1^{WW} are possible in the SM with $a_1^{\text{ZZ}} = a_1^{\text{WW}} = 2$. In BSM hypotheses, only the q^2 -independent a_i^{VV} , or Λ_1 and Λ_Q with $|g_i'^2| = |g_i'^4| = 1$ are considered.
2. $\text{VV} = \text{Z}\gamma$ or $\gamma\gamma$: In the SM, this process can only happen via a loop of fermions, where primary contributors are heavy quarks, or a loop of W bosons, so only $\kappa_t, \kappa_b, \kappa_W$ and κ_Z are dominant and non-zero. Sub-dominant contributions also come from light quarks. The BSM couplings discussed in this thesis are always measured with the Z and γ

bosons decaying to 2ℓ , so contributions from the terms scaling with $\Lambda_1^{Z\gamma}$ ($|g_i'^{2,Z\gamma}| = 1$), $a_2^{Z\gamma}$, $a_3^{Z\gamma}$, $a_2^{\gamma\gamma}$ and $a_3^{\gamma\gamma}$ are compared against the SM term relevant for the $H \rightarrow ZZ \rightarrow 4\ell$ decay scaling with $a_1^{ZZ} = a_1^{WW}$.

3. $VV = gg$: The only couplings possible in the SM are κ_q for all six flavors of quarks. Of those six, the most dominant contribution is from κ_t , followed by about 10% additional effect from κ_b . We only mention briefly in Section 3.4 the phenomenological effect of different BSM scenarios with non-zero $\tilde{\kappa}_{t,b}$ or $a_{2,3}^{gg}$, but we do not measure them explicitly.

In ZZ and WW anomalous couplings, we conveniently use a_i to stand for a_i^{ZZ} in the notation in subsequent discussion.

For most of the results discussed in this thesis, we vary anomalous couplings for ZZ, $Z\gamma$ and WW. We also require the additional constraint $a_i^{WW} = a_i^{ZZ}$ except in a few measurements in Run 1. In these measurements, instead of constraining a_i directly, we constrain the fractional contribution of the anomalous coupling to the total partial width of on-shell $H \rightarrow 2e2\mu$ decay because most of the systematics common to any BSM coupling would cancel in the ratio, and because the $2e2\mu$ channel does not feature interference between different permutations of leptons forming the Feynman diagrams. Relative contribution of these couplings either in off-shell H boson production or in H boson production mediated by two electroweak gauge bosons can always be defined in terms of these fractions. We therefore define the fractions f_{ai} and

phases ϕ_{ai} as follows

$$f_{ai} = \frac{|a_i|^2 \sigma_i}{\sum_{j=1,2,3\dots} |a_j|^2 \sigma_j},$$

$$\phi_{ai} = \arg \left(\frac{a_i}{a_1} \right).$$

The ratio between the cross sections σ_i to σ_1 are defined for on-shell $2e2\mu$ events and are listed in Table 3.1 for the assumption $m_H = 125$ GeV. The relationship between a_i^{ZZ}/a_1^{ZZ} and a_i^{WW}/a_1^{WW} can also be relaxed with the following re-parameterization of f_{ai}^{WW} as a function of f_{ai} and ZZ-to-WW double ratio:

$$\begin{aligned} r_{ai} &= \frac{a_i^{WW}/a_1^{WW}}{a_i^{ZZ}/a_1^{ZZ}} \text{ or } R_{ai} = \frac{r_{ai} |r_{ai}|}{1 + r_{ai}^2} \\ S_{ai}^{WW} &= \frac{\sigma_1^{WW}/\sigma_i^{WW}}{\sigma_1^{ZZ}/\sigma_i^{ZZ}} \\ f_{ai}^{WW} &= \frac{R_{ai} f_{ai}}{S_{ai}^{WW} (1 - |R_{ai}|) (1 - |f_{ai}|) + |R_{ai} f_{ai}|}. \end{aligned} \tag{3.4}$$

Table 3.1: List of anomalous HVV couplings considered in the measurements assuming a spin-zero H boson. The cross section ratios correspond to on-shell $H \rightarrow 2e2\mu$ decay and the H boson mass $m_H = 125 \text{ GeV}$ and are derived from JHUGEN [100–103] calculation. The cross sections $\tilde{\sigma}_{\Lambda_i}$ absorb the dimensions of the corresponding Λ_i scales.

Anomalous Coupling	Coupling Phase	Effective Fraction	Translation Constant
a_2	ϕ_{a2}	f_{a2}	$\sigma_1/\sigma_2 = 2.77$
a_3	ϕ_{a3}	f_{a3}	$\sigma_1/\sigma_3 = 6.53$
Λ_1	$\phi_{\Lambda 1}$	$f_{\Lambda 1}$	$\sigma_1/\tilde{\sigma}_{\Lambda 1} = 1.47 \times 10^4 \text{ TeV}^{-4}$
$\Lambda_1^{Z\gamma}$	$\phi_{\Lambda 1}^{Z\gamma}$	$f_{\Lambda 1}^{Z\gamma}$	$\sigma_1/\tilde{\sigma}_{\Lambda 1}^{Z\gamma} = 5.80 \times 10^3 \text{ TeV}^{-4}$
Λ_Q	$\phi_{\Lambda Q}$	$f_{\Lambda Q}$	$\sigma_1/\tilde{\sigma}_{\Lambda Q} = m_H^{-4}$

3.2 Standard Model Higgs boson production and decay at the LHC

The H boson is produced at the LHC via the interactions between the quarks or the gluons in the proton-proton collisions. The dominant modes are through gluon fusion (ggH), weak vector boson fusion (VBF), $q\bar{q}$ annihilation in association with a weak vector boson (VH, Higgs-strahlung), and associated production with two top or bottom quarks ($t\bar{t}H$ and $b\bar{b}H$ respectively). Leading order diagrams of these four different important production mechanisms are given in Fig. 3.1. A subdominant production mechanism in association with a single top quark (tqH) also becomes significant at $\sqrt{s} = 13 \text{ TeV}$ and high H boson invariant mass, but we will not consider this mode in this thesis.

The relative contribution of each production mode depends on the parton luminosity of quarks and gluons and hence is different along the H boson

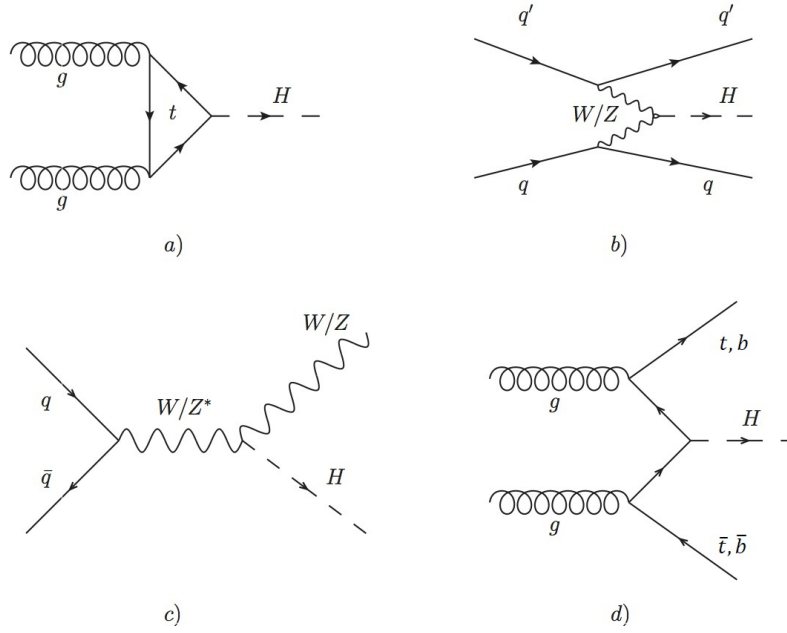


Figure 3.1: H boson production mechanisms are represented at tree level for ggH (a), VBF (b), WH or ZH (c), and $t\bar{t}H$ or $b\bar{b}H$ (d).

invariant mass. For the invariant masses relevant at the LHC, the general trend is that production modes dominated by quarks have an increasing relative contribution with respect to those dominated by gluons as the H boson invariant mass increases. This means that at around $\sqrt{q_H^2} \sim 125$ GeV, H boson production is dominated by gluon fusion mediated by top and bottom triangle loops, whereas at 2 TeV, the H boson is produced mainly via VBF. H boson cross sections at $\sqrt{s} = 8$ and 13 TeV are shown on Fig. 3.2 for the different dominant and subdominant contributions [99, 104].

The ggH production receives large QCD perturbative corrections when accounting for both NLO and NNLO contributions. Note on both panels of Fig. 3.2 that the gg production features an enhancement at around $\sqrt{q_H^2} = 2m_t$ because of the top loop, and this $2m_t$ threshold is also enhanced further with

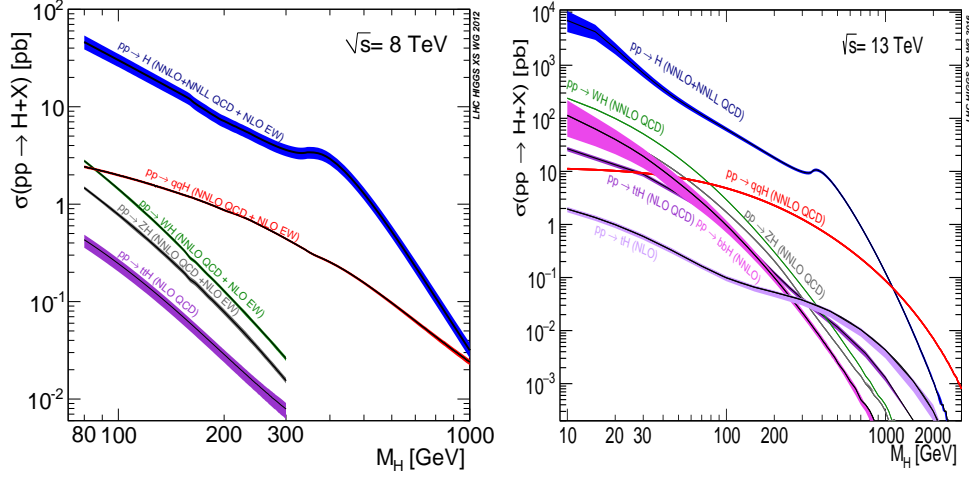


Figure 3.2: H boson production cross sections for the different production modes are shown at $\sqrt{s} = 8$ (left) [104] and 13 TeV (right) [99] in different colors. ggH production mechanism is labelled as $pp \rightarrow H$, and VBF is labelled as $pp \rightarrow qqH$ on these plots.

these QCD corrections. While it is possible to simulate the effects of NLO QCD in this production mode, it is not yet possible to simulate the additional NNLO contributions completely. Instead, any simulation of ggH applies appropriate scale factors (K factors) as a function of the $\sqrt{q_H^2}$ of the H boson. The corrections used in this thesis [99] are calculated using HNNLO v2 [105–107] and are shown on Fig. 3.3. In addition to these K factors, a flat correction of +9.9% is known at $m_H = 125$ GeV and $\sqrt{s} = 13$ TeV to scale the signal cross section to N³LO in QCD [99], so this correction is also applied when deriving results from Run 2 data.

H boson total width Γ_H and branching ratios are calculated up to NLO in QCD and EW [99, 104] and are shown in Fig. 3.4. We observe from the right panel that at $\sqrt{q_H^2} = 125$ GeV, dominant decay mode is the $b\bar{b}$ final state, and at very high masses, the dominant decay modes are WW and ZZ.

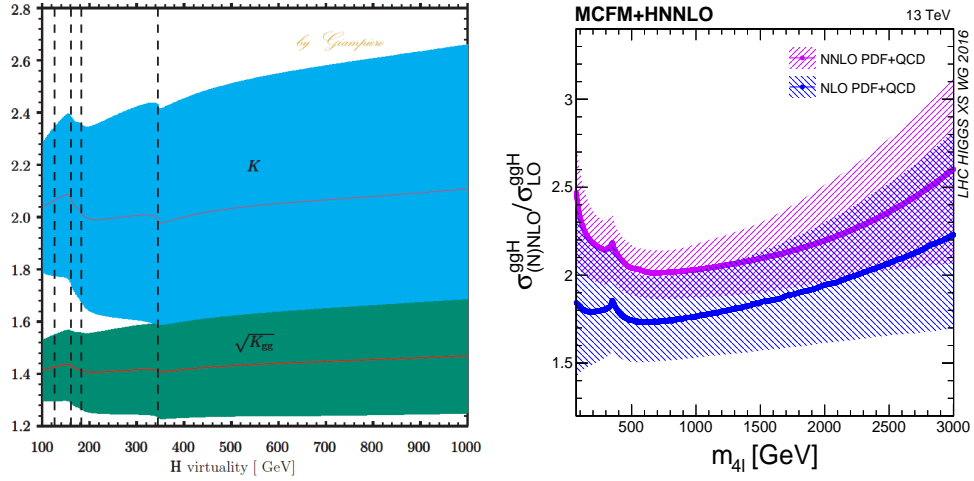


Figure 3.3: Left panel: H boson gluon fusion production K factors to scale the signal from LO in QCD to NNLO in QCD at $\sqrt{s} = 8$ TeV. $\sqrt{K_{gg}}$ shown is the approximate K factor proposed in Ref. [96] for the interference component between gg signal and continuum 4ℓ background. K factors for $\sqrt{s} = 7$ TeV are very similar to those of $\sqrt{s} = 8$ TeV, so they are not shown explicitly. Right panel: H boson gluon fusion production K factors to scale the signal from LO in QCD to either NLO or NNLO in QCD at $\sqrt{s} = 13$ TeV [99]. In the analysis, the signal K factors on both panels are applied on all of the signal, background and interference contributions in the 4ℓ final state.

However, high signal-to-background ratio is important for an experiment to identify good H boson candidate events from the backgrounds, and different mass regions require different choices for which production and decay modes to search. At low mass, $H \rightarrow b\bar{b}$ has the most dominant branching ratio, but gluon fusion production is not accessible due to very high rates of QCD background. On the other hand, VBF and VH production modes in this decay mode has a more distinct signature. VBF and VH topologies in the $H \rightarrow \tau\tau$ decay channel are likewise separable from the background. While $H \rightarrow \gamma\gamma$ and $H \rightarrow ZZ$ have relatively lower rates, one benefits from being able to reconstruct the final states completely and employ full kinematic information to separate signal from background. Because the dominant decay modes

are WW and ZZ at high mass, one can examine $ZZ \rightarrow 4\ell$, $2\ell 2q$ or $2\ell 2\nu$, or $WW \rightarrow \ell\nu\ell\nu$ or $\ell\nu 2q$ events.

As we can read from the left panel of Fig. 3.4, $\Gamma_H = 4.1$ MeV at $m_H = 125$ GeV. This Γ_H value is not measurable directly using on-shell H boson events with in the $ZZ \rightarrow 4\ell$ or $\gamma\gamma$ decay since the resolution from the detector is around 1 GeV. We leave it to Section 3.4 to discuss the technique which could make this measurement possible.

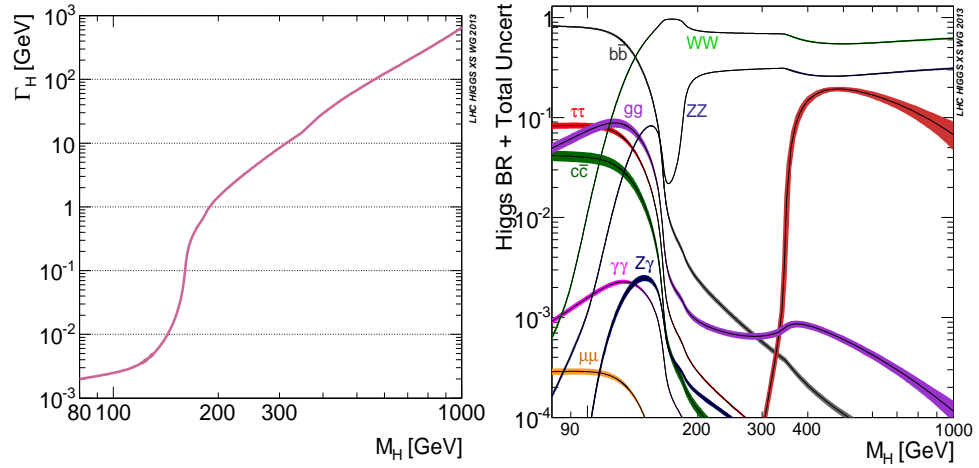


Figure 3.4: H boson total decay width Γ_H (left) and branching ratios (right) for a wide range of masses [99, 104]: At $\sqrt{q_H^2} = 125$ GeV, the dominant decay mode is the $b\bar{b}$ final state, and at very high masses, the dominant decay modes are WW and ZZ . In the right plot, the rise of the Higgs branching ratio at around 300 GeV is due to $H \rightarrow t\bar{t}$ decay and is not to be confused with $H \rightarrow \tau\tau$ decay, which is shown with a similar color in the plot.

3.3 Simulation and analysis tools for the Higgs boson

Tools to simulate H boson signal and the relevant backgrounds, and to distinguish signal from other backgrounds, or alternative signal hypotheses, play

an important role in the discovery of the H boson and the subsequent studies of its properties. Simulation at leading-order QCD may be good enough to describe the decay of the H boson in most cases, but the description of associated particles, or the backgrounds, usually require higher-order corrections to be applied, or approximated, to account for the multiplicity of associated particles, correct correlations between the different final states, and accurate modeling of theoretical systematics. In the following discussions in this section, we take the 4ℓ final state as a medium for discussion since most of the results are presented using this decay mode.

3.3.1 Simulation tools

The standard procedure to investigate correlations between different particles and to construct higher-level analysis observables from these correlations is to simulate the process in question via the Monte-Carlo (MC) method in which events are sampled randomly according to the prescribed multidimensional probability distribution based on the kinematics of the initial and final states. A simulation program commonly used for the simulation of SM H boson signals is the POWHEG generator, V1 in Run 1 and V2 in Run 2 [108–112], which allows NLO QCD effects in the parton-level process. This program is used for the generation of H boson signal for various H boson mass values, from 115 GeV to 3 TeV, in the five main production modes ggH , $t\bar{t}H$, VBF, WH and ZH. To generate a more accurate ggH signal model, the p_T spectrum of the H boson from the POWHEG simulation is tuned at each m_H value separately to

better match predictions from NNLO QCD calculations with next-to-next-to-leading log resummations implemented in the HRES generator [107, 113–116]. Run 2 analyses presented in Chapter 4 simulate the WH and ZH production modes using the MINLO HVJ [117] extension of POWHEG V2 to model up to two additional jets, in addition to the particles already coming from the associated V decay, more accurately. In the simulation of 2016 and 2017 Run 2 detector conditions, the $b\bar{b}H$ production mode is added using JHUGEN event generator [100–103]. The POWHEG signal simulations do not decay the H boson, so its decay is also modeled by JHUGEN. This type of subsequent decay is possible only for a spin-0 particle for which production and decay are independent of each other.

The JHUGEN program is utilized extensively in the simulation of decay or production of the H boson in the presence of anomalous HVV couplings. In the ggH and $t\bar{t}H$ production modes, higher-order QCD effects on the production side are already included from the POWHEG simulation, so the simulation of the different anomalous couplings in HVV are achieved simply by varying the decay hypothesis of the H boson. Likewise in the $b\bar{b}H$ simulation, changing the decay model of the H boson is sufficient to model these effects. Simulation at LO in QCD is adopted from JHUGEN when VBF, WH and ZH productions are considered since JHUGEN does not yet have the capability to model higher-order QCD corrections in these processes.

As will be discussed in Section 3.4, H boson signal production may have a sizable off-shell tail in ZZ or WW decays, and the continuum background and its interference with the H boson signal are also sizable in this region. In

simulations for both Run 1 and Run 2, the MCFM simulation [94, 118, 119] is used to model the different gg contributions, including signal with off-shell effects and certain reference values of m_H and Γ_H (i.e. $m_H = 125.6$ GeV and $\Gamma_H = 4.15$ MeV in Run 1 analyses, and $m_H = 125.0$ GeV and $\Gamma_H = 4.07$ MeV in Run 2 analyses). In Run 1 simulations, the generator PHANTOM [120] is used for the modeling of electroweak H boson signal (i.e. VBF, WH and ZH), continuum background (i.e. vector boson scattering and tri-boson production) and their interference at LO in QCD. In Run 2, the POWHEG simulation is reweighted with the matrix elements at LO in QCD provided by the MELA package [82, 100–103], which interface the MCFM and JHUGEN generators to compute them for each event at parton-level. The same package is also used conveniently to reweight any SM or BSM HVV signal hypothesis, in any production mode or from any generator, to any other HVV signal hypothesis while accounting for signal-background interference effects correctly.

The SM ZZ background contribution from quark-antiquark annihilation is treated as a non-interfering background and is simulated using the POWHEG generator at NLO QCD [121, 122]. The fully differential cross section has been computed at NNLO QCD [123] but is not yet available for event generation, so the simulation is scaled with a K-factor as a function of $m_{4\ell}^{\text{true}}$ for the NNLO/NLO ratio. Additional NLO electroweak corrections [124, 125] which depend on the initial state quark flavor and kinematics are also applied to this process in the region $m(\text{ZZ}) > 2m(\text{Z})$ where the corrections have been computed. The differential QCD and electroweak K factors are illustrated for 13 TeV in Fig. 3.5.

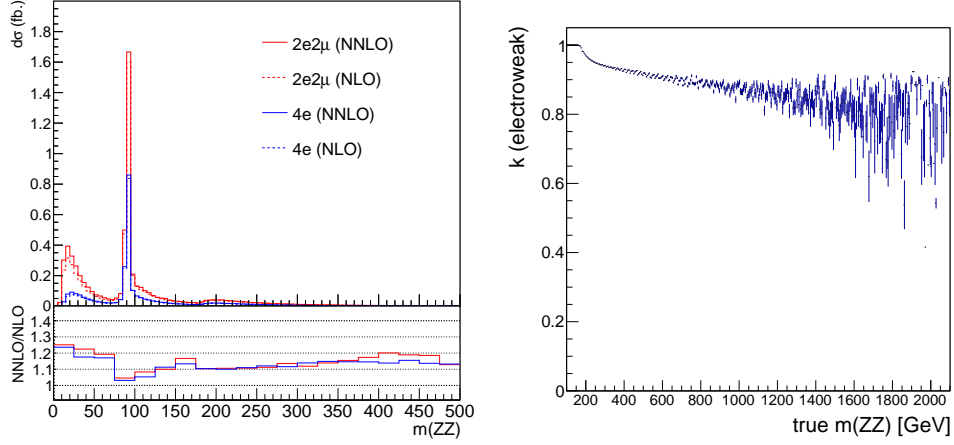


Figure 3.5: Left: NNLO/NLO QCD K factor for the $q\bar{q} \rightarrow ZZ$ background [123] as a function of m_{ZZ} for the 4ℓ and $2\ell 2\ell'$ final states. Right: NLO/LO electroweak K factor [124, 125] as a function of m_{ZZ} . The K factors are illustrated for 13 TeV pp collision energy.

Any simulated parton-level process needs to account for nuclear effects, soft radiations or subsequent production of baryons and mesons from the partons in the hard-process, and detector response before reconstruction algorithms can be run on the final particles. These steps are achieved with PYTHIA 6.4 [126] in Run 1 and 8 [127] in Run 2. This hadronization step uses tunes Z2 and Z2* [128] in Run 1 and tune CUETP8M1 [129] in Run 2. The generated events are processed through a detailed simulation of the CMS detector based on GEANT4 [130, 131] before they are reconstructed with the same algorithms that are used on the data.

3.3.2 Kinematic discriminants

Kinematic information contained in a typical $H \rightarrow VV \rightarrow 4f$ processes is shown in Fig. 3.6. $\cos\theta^*$ and Φ_1 distributions are flat in any spin-0 signal

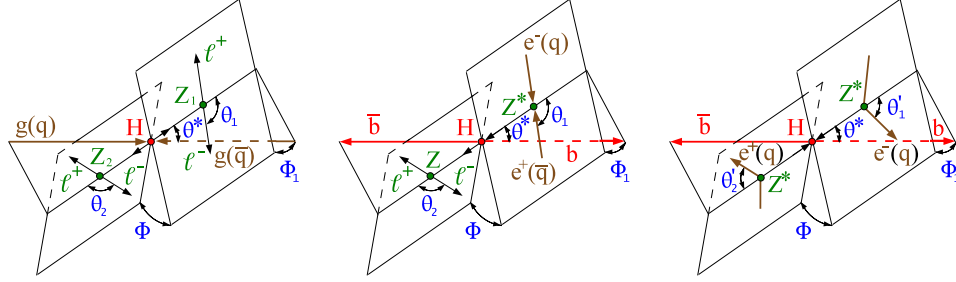


Figure 3.6: Illustrations of H boson production and decay in pp or e^+e^- . Typical VV decay process via gg or $q\bar{q}$ production (left), ZH (middle) and VBF (right) are shown as different rotations of the same diagram. Five angles and three invariant masses fully characterize the production or decay chain, and the angles are defined in the rest frame of the H boson [102].

hypothesis, but their distributions change in spin-1 or spin-2 resonances or the backgrounds. An example set of the other kinematic observables is illustrated in Fig. 3.7.

As evident from the degree of variations shown in Fig. 3.7 for the different kinematic observables, it is difficult to select a subset of them to distinguish different signal hypotheses from each other, or from backgrounds. It is therefore desirable, and doable, to condense the information in the different variables into a single discriminant when full kinematic information is available, or if the missing information such as the momenta of the incoming partons can be approximated. The MELA package allows the possibility to condense this information by computing matrix elements with reconstructed kinematic observables as input. Two main types of discriminants can be computed from the per-event matrix elements:

$$\mathcal{D}_{\text{alt}}(\vec{\Omega}) = \frac{\mathcal{P}_{\text{sig}}(\vec{\Omega})}{\mathcal{P}_{\text{sig}}(\vec{\Omega}) + \mathcal{P}_{\text{alt}}(\vec{\Omega})} \quad (3.5)$$

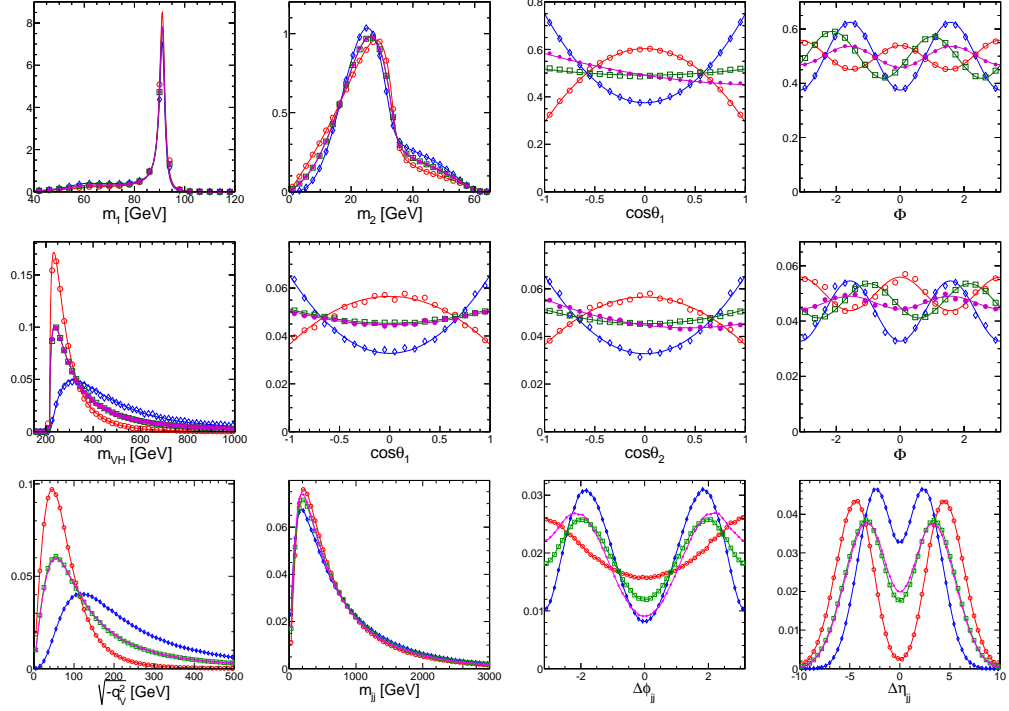


Figure 3.7: Top panel: Exemplary kinematic variables in $H \rightarrow ZZ \rightarrow 4f$ decay. From left to right are m_1 , m_2 (where m_1 taken to be the closest to m_Z), $\cos\theta_1$ (same as $\cos\theta_2$), and Φ . Middle panel: Exemplary kinematic variables in the $p\bar{p} \rightarrow Z^* \rightarrow ZH$ production mode. From left to right are m_1 (m_{VH}), $\cos\theta_1$, $\cos\theta_2$, and Φ . Bottom panel: Exemplary kinematic variables in the VBF production mode. From left to right are m_1 or m_2 ($\sqrt{-q_{1,2}^2}$), m_{jj} , $\Delta\eta_{jj}$ and $\Delta\phi_{jj}$. In the top two panels, points show simulated events, and lines show projections of analytical distributions. In the bottom panel, lines are only to guide the reader. Four scenarios are shown in each of the plots: SM (red open circles), pseudoscalar (blue diamonds), and two mixed states corresponding to $f_{a3} = 0.5$ with $\phi_{a3} = 0$ (green squares) and $\pi/2$ (magenta points). f_{a3} in the ZH or VBF production modes is defined for their own $\sigma_1^{\text{prod}}/\sigma_3^{\text{prod}}$ ratios instead of being defined from $2e2\mu$ decay [102].

and

$$\mathcal{D}_{\text{int}}(\vec{\Omega}) = \frac{\mathcal{P}_{\text{int}}(\vec{\Omega})}{\mathcal{P}_{\text{sig}}(\vec{\Omega}) + \mathcal{P}_{\text{alt}}(\vec{\Omega})}, \text{ or } \frac{\mathcal{P}_{\text{int}}(\vec{\Omega})}{2 \cdot \sqrt{\mathcal{P}_{\text{sig}}(\vec{\Omega}) \cdot \mathcal{P}_{\text{alt}}(\vec{\Omega})}}, \quad (3.6)$$

where “sig” denotes the SM-like signal; “alt” stands for an alternative model, which could be background, an alternative H boson production mechanism, or an alternative H boson coupling model. The “int” label represents the interference between the two model contributions. Two equivalent forms of interference discriminant are defined, where the latter form carries less correlation between the two discriminants and is therefore preferred. Probabilities are normalized for the matrix elements to give the same cross sections in the relevant phase space of each process. Such normalization leads to a balanced distribution of events in the range between 0 and 1 of the \mathcal{D}_{alt} discriminants, and between -1 and 1 of \mathcal{D}_{int} . In computing matrix elements that involve H boson production information, and hence parton distribution functions, the p_T of the H + jet(s) system is taken out before any computation.

By the Neyman-Pearson lemma [132], the \mathcal{D}_{alt} discriminant contains all the information available from the kinematics to separate the two alternative hypotheses. Examples of \mathcal{D}_{alt} used in the analysis presented are \mathcal{D}_0 using decay-only information, or $\mathcal{D}_0^{\text{VBF+dec}}$ using both decay and production information in order to distinguish the SM hypothesis from the alternative pseudoscalar signal hypothesis; $\mathcal{D}_{\text{bkg}}^{\text{kin}}$ using decay-only information, $\mathcal{D}_{\text{bkg}}^{\text{VBF+dec}}$ using both decay and production information, or \mathcal{D}_{bkg} which contains in addition the $m_{4\ell}$ shape of signal and background folded into their respective probabilities, in order to distinguish the SM hypothesis from the alternative

hypothesis of background; and $\mathcal{D}_{2\text{jet}}^{\text{VBF}}$ using production-only information with the two associated jets in order to distinguish the VBF hypothesis from the alternative HJJ production via gluon fusion. Similarly, examples to \mathcal{D}_{int} could be $\mathcal{D}_{\text{CP}}^{\text{dec}}$ using decay-only information, or $\mathcal{D}_{\text{CP}}^{\text{VBF}}$ using production-only information in order to be sensitive to the interference between SM scalar and BSM pseudoscalar signal hypotheses.

3.4 The off-shell technique to measure the width and anomalous couplings

A direct width measurement from on-shell events using the resonance peak is limited by an experimental resolution of $\mathcal{O}(1)$ GeV in the $H \rightarrow ZZ \rightarrow 4\ell$ and $H \rightarrow \gamma\gamma$ decay channels, but as we discussed in Section 3.2, the SM H boson has a total width of 4.1 MeV [99, 104]. It was proposed to constrain the H boson width using its off-shell production and decay to two Z bosons away from the resonance peak [92, 94–96]. The zero-width approximation is inadequate in describing decay to two massive gauge bosons, and off-shell production cross section becomes sizable. In the decay of the H boson to a pair of massive gauge bosons V with mass $m_V < m_H < 2m_V$, either one of the gauge bosons decay off-shell or the H boson decay off-shell, so the decay branching ratio is enhanced in the vicinity of the V-boson pair production threshold as seen on Fig. 3.4. A further enhancement comes in gluon fusion production from the top-quark pair production threshold.

The H boson event rate for production from a generic pair of vector bosons vv and decay to a generic pair of massive vector bosons VV depends on

Γ_H through the H boson propagator and can be written, up to mass-dependent terms in the production cross sections $\sigma_{vv \rightarrow H}$ shown in Fig. 3.2 and decay branching ratios $\mathcal{BR}_{H \rightarrow VV}$ shown in Fig. 3.4, as

$$\frac{d\sigma_{vv \rightarrow H \rightarrow VV}}{dq_H^2} \sim \frac{g_{vvH}^2 g_{HVV}^2}{(q_H^2 - m_H^2)^2 + m_H^2 \Gamma_H^2}, \quad (3.7)$$

where g_{vvH} and g_{HVV} are the couplings of the H boson to vv on the production side and VV on the decay side, respectively. Integrating either in a small region around m_H or above the mass threshold $2m_V$, the relationship between on-shell and off-shell event rates can be written up to momentum-dependent factors as

$$\begin{aligned} N_{vv \rightarrow H \rightarrow VV^*}^{\text{on-shell}} &\sim \frac{g_{vvH}^2 g_{HVV}^2}{m_H \Gamma_H} \sim \mu_{vvH}, \\ N_{vv \rightarrow H^* \rightarrow VV}^{\text{off-shell}} &\sim \frac{g_{vvH}^2 g_{HVV}^2}{(2m_V)^2} \sim \mu_{vvH} \cdot \Gamma_H. \end{aligned} \quad (3.8)$$

The last proportionality relations in Eqn. 3.8 illustrate the phenomenological core of the off-shell technique: The off-shell event rate should scale linearly with Γ_H for the same number of on-shell events observed. While kinematic properties may change with a different choice of vv production modes or with different BSM anomalous couplings, this relationship still remains valid, albeit with different normalization factors, as long as a H boson propagator is present and $\Gamma_H \ll m_H < 2m_V$.

Overall, off-shell H boson production may account for about 10% [92, 93] of the total gg production rate in SM $H \rightarrow VV$ decay, and for similar proportions in other SM production modes. In the presence of anomalous HVV couplings,

however, this proportion may be much larger; as illustrated on the left panel of Fig. 3.8 for the gluon fusion production mode, different couplings may give rise to a H boson decay rate several orders of magnitude larger than that in the SM for the same number of on-shell events. The enhancement is largest for the pure Λ_Q term (not shown), followed by a_3 , a_2 and Λ_1 , and it occurs because of factors dependent on the momentum of the H boson or the two V's in the scattering amplitude in Eqn. 3.2. This type of enhancement also occurs on the production side for VBF or VH production modes regardless of q_H^2 because of the dependence of the amplitude terms on $q_{1,2}$, and this translates to a double-enhancement for these production modes in the off-shell region with respect to what is shown in Fig. 3.8.

At large q_{VV}^2 in the off-shell region, both V bosons are polarized mostly longitudinally in both the signal and background amplitudes. The similarity in polarization and the lack of a narrow signal resonance in this region allows large and destructive interference to occur between the H boson-mediated signal and continuum VV background amplitudes, reaching in magnitude as large as twice the size of the signal amplitude. In the case of vector boson scattering (VBS), this destructive interference has been known for a long time as necessary to preserve the unitarity of the $VV \rightarrow VV$ scattering amplitude and place a theoretical upper bound on the H boson mass of $m_H < 710$ GeV [26, 133, 134]. Therefore, the relationship between the on-shell and off-shell regions outlined in Eqn. 3.8 is also modified to include the contribution from

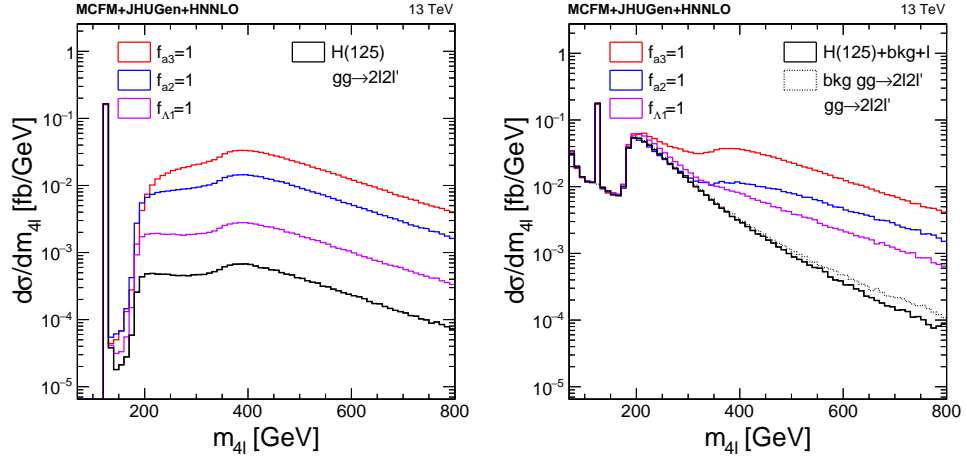


Figure 3.8: Left panel: Signal $gg \rightarrow H \rightarrow 2l2l'$ $m_{4\ell}^{\text{true}}$ lineshape for the pure SM (black), a_3 (red), a_2 (blue) and Λ_1 (magenta) hypotheses at 13 TeV. Right panel: Total $gg \rightarrow 2l2l'$ $m_{4\ell}^{\text{true}}$ lineshape with signal, background and their interference for the pure SM (black), a_3 (red), a_2 (blue) and Λ_1 (magenta) signal hypotheses at 13 TeV. The solid histograms show the total contributions in each of the signal hypotheses, including interference contributions with the SM background fully modeled for the particular signal coupling term. The dashed histogram shows only the continuum background contribution, where the difference with respect to the SM total distribution is negative at high mass due to the large and destructive SM interference [99]. The same QCD NNLO K factor from Fig. 3.3 multiplies all of the distributions shown.

the background amplitude:

$$\begin{aligned}
 N_{sig}^{\text{on-shell}} &\sim \mu_{vvH} \quad \text{and} \quad N_{sig}^{\text{off-shell}} \sim \mu_{vvH} \cdot \Gamma_H, \\
 N_{bkg} &\sim k_{bkg}, \\
 N_{int}^{\text{off-shell}} &\sim \sqrt{\mu_{vvH} \cdot \Gamma_H \cdot k_{bkg}}, \tag{3.9}
 \end{aligned}$$

where k_{bkg} is an arbitrary scale factor for the background contribution, conventionally set to 1. Notice that interference in the on-shell region is not taken into account because Γ_H is very small and the kinematic properties of signal and background are very different, unlike their behavior in the off-shell region.

The scaling of $N_{int}^{\text{off-shell}}$ assumes that any k_{bkg} corrections on the background do not change the phase between the signal and background amplitudes.

Just like the signal contribution itself, the interference pattern in the off-shell region may also change in the presence of BSM anomalous couplings. For example, while interference between the pure CP-odd term a_3 and the CP-even background amplitude may be non-zero as a function of different kinematic observables, its projection on $m_{4\ell}$, a CP-insensitive observable, has to be exactly zero, in comparison to the large and destructive effect predicted in the SM. The effect of the different SM, a_3 , a_2 and Λ_1 HVV couplings in decay are illustrated for the total $gg \rightarrow 4\ell$ process on the right panel of Fig. 3.8.

In addition to a study of anomalous HVV couplings with experimental results presented in Chapter 4, we also briefly illustrate the effect of anomalous ggH couplings for completeness. From the amplitude in Eqn. 3.2, we can consider four terms in this amplitude: Loop terms that scale with the Hff scalar couplings κ_t or κ_b , or the pseudoscalar couplings $\tilde{\kappa}_t$ or $\tilde{\kappa}_b$, and the a_2^{gg} and a_3^{gg} terms that correspond to scalar and pseudoscalar loop integrals in the limit of infinite quark mass. The effect of terms on the $m_{4\ell}$ lineshape is illustrated in Fig. 3.9. The $m_{4\ell}$ lineshape for the pure $\tilde{\kappa}_t$ term features a different top pair threshold shape than that of the pure κ_t term or the SM, but the on-shell– off-shell proportion of event rates remains similar. On the other hand, the pure κ_b or $\tilde{\kappa}_b$ terms exhibit much less off-shell events due to lack of terms in the amplitude that would enhance it at higher masses. The a_2^{gg} and a_3^{gg} terms still follow the general SM-like lineshape, but as expected, they do not have a threshold behavior near $2m_t$. Note also that the phase of

interference in the different scalar couplings may be barely measurable based only on the $m_{4\ell}$ information and the small changes in its shape. The different signal, background and interference contributions are multiplied with the same 13 TeV QCD NNLO K factor shown in Fig. 3.3 for simplicity, but it is possible that the enhancement of this K factor around $2m_t$ may be different under the presence of different ggH couplings.

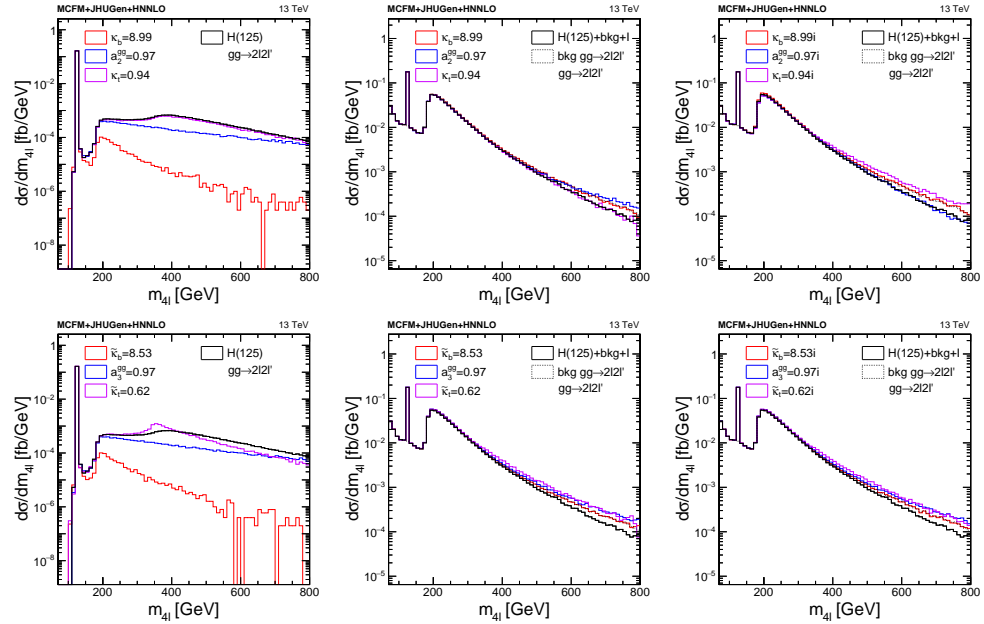


Figure 3.9: Top row: $m_{4\ell}^{\text{true}}$ distribution of signal or total $gg \rightarrow 2l2l'$ events for the pure SM (black), pure κ_b (red), pure κ_t (magenta) and a_2^{gg} (blue) hypotheses at 13 TeV. Bottom row: $m_{4\ell}^{\text{true}}$ distribution of signal or total $gg \rightarrow 2l2l'$ events for the pure SM (black, same as top panels), pure $\tilde{\kappa}_b$ (red), pure $\tilde{\kappa}_t$ (magenta) and a_3^{gg} (blue) hypotheses at 13 TeV. In both rows, the left panels show the signal-only distributions, the middle panels show the scenarios where the phase of the couplings are 0, and the right panels show the scenarios where the phases are $\pi/2$. Although it may not be fully correct at $m_{4\ell}^{\text{true}} \sim 2m_t$, the same QCD NNLO K factor from Fig. 3.3 multiplies all of the distributions shown for simplicity in illustration. In all cases, the couplings of the signal are adjusted to give the same cross section as expected from the SM.

Chapter 4

Analysis of the Higgs boson properties during Run I and Run II of the LHC

4.1 Analysis of anomalous HVV couplings from on-shell Higgs boson production

Constraints on anomalous HVV couplings are placed using events from the Run 1 or Run 2 data taking periods. The general formalism of these couplings were already mentioned in detail in Section 3.1. In the Run 1 analysis, the tested contributions are a_2, a_3, Λ_1 for the HZZ vertex, $a_2^{Z\gamma}, a_3^{Z\gamma}$ and $\Lambda_1^{Z\gamma}$ for the HZ γ vertex, and $a_2^{\gamma\gamma}$ and $a_3^{\gamma\gamma}$ for the H $\gamma\gamma$ vertex. HZZ and HWW couplings are assumed to be the same, but test of separating them on the decay side are also performed via comparison to events from $H \rightarrow WW \rightarrow 2\ell 2\nu$ events [135]. In Run 2, only the anomalous HZZ contributions, or the $\Lambda_1^{Z\gamma}$ contribution, are tested from the 4ℓ decay with the assumption that HZZ and HWW couplings are the same.

All of the trigger, object identification and selection elements in the 4ℓ

channel are identical to what is discussed in Section 2.4.2 and Refs. [72–75], and the details of the $H \rightarrow WW \rightarrow 2\ell 2\nu$ analysis can be found in Ref. [135]. In the Run 1 analysis, the nominal mass of the H boson is assumed to be $m_H = 125.6$ GeV, and in the Run 2 analysis, $m_H = 125.0$ GeV is assumed. When combination of Run 1 and Run 2 results are reported, Run 1 results are re-analyzed for the value $m_H = 125.0$ GeV.

4.1.1 Run 1 analysis strategy

The observables used in the 4ℓ decay channel use only the decay information and are not sensitive to the behavior of associated particles. Events are only divided into the $2e2\mu$, $4e$ and 4μ channels, and for each anomalous coupling hypothesis, a dedicated pair of \mathcal{D}_{BSM} and \mathcal{D}_{int} is constructed as prescribed in Section 3.3 in the on-shell H boson production region, defined as $105.6 < m_{4\ell} < 140.6$ GeV. When the results are re-analyzed for $m_H = 125.0$ GeV, the mass window is shifted to $105 < m_{4\ell} < 140$ GeV. Distributions of an exemplary set of these discriminants is shown in Fig. 4.1.

Only partial reconstruction is possible in the $WW \rightarrow 2\ell 2\nu$ decay. This channel features two isolated, high- p_T , charged leptons and E_T^{miss} due to the presence of neutrinos in the final state. The kinematic distributions of the decay products exhibit the characteristic properties of the parent boson. Three observables can be computed from the two leptons: The azimuthal opening angle between the two leptons ($\Delta\phi_{\ell\ell}$), which is correlated with the spin of the H boson; the dilepton mass ($m_{\ell\ell}$), which is one of the most discriminating kinematic variables for a H boson with low mass and is also correlated to

the spin and to $\Delta\phi_{\ell\ell}$; and the transverse mass (m_T) of the final state objects, which scales with the Higgs boson mass. The transverse mass is defined as $m_T^2 = 2p_T^{\ell\ell} E_T^{\text{miss}}(1 - \cos \Delta\phi(\ell\ell, \vec{E}_T^{\text{miss}}))$, where $p_T^{\ell\ell}$ is the dilepton transverse momentum and $\Delta\phi(\ell\ell, \vec{E}_T^{\text{miss}})$ is the azimuthal angle between the dilepton momentum and \vec{E}_T^{miss} . Two of these observables are used in the final analysis, $m_{\ell\ell}$ and m_T . These two kinematic observables are independent quantities that effectively discriminate signal against most of the backgrounds, and between different signal models in the dilepton analysis in the 0-jet and 1-jet categories. The signal region is defined by $m_{\ell\ell} < 200$ GeV, and $60 \leq m_T \leq 280$ GeV. The distributions of these observables for data, an expected SM Higgs signal, an alternative signal model with $f_{a3}^{WW} = -0.4$, and backgrounds are presented in Fig. 4.2, and the complete set of observables in ZZ and WW are listed in Table 4.1.

4.1.2 Run 2 analysis strategy

Events only from the 4ℓ decay channel in the $m_{4\ell}$ mass window $105 < m_{4\ell} < 140$ GeV are used in the Run 2 analysis. In the 2015 data taking period, the observables used are identical to what is shown in Table 4.1, just like the rest of the analysis strategy as discussed in Section 4.1.1. After 2015, kinematic information from associated particles is also taken into account to both categorize the events for VBF and VH production with hadronic V decay, and make use of this information to distinguish alternative signal hypotheses from the SM hypothesis. The observables used for the 2016 and 2017 data taking periods are listed in Table 4.2 [136], and exemplary distributions of

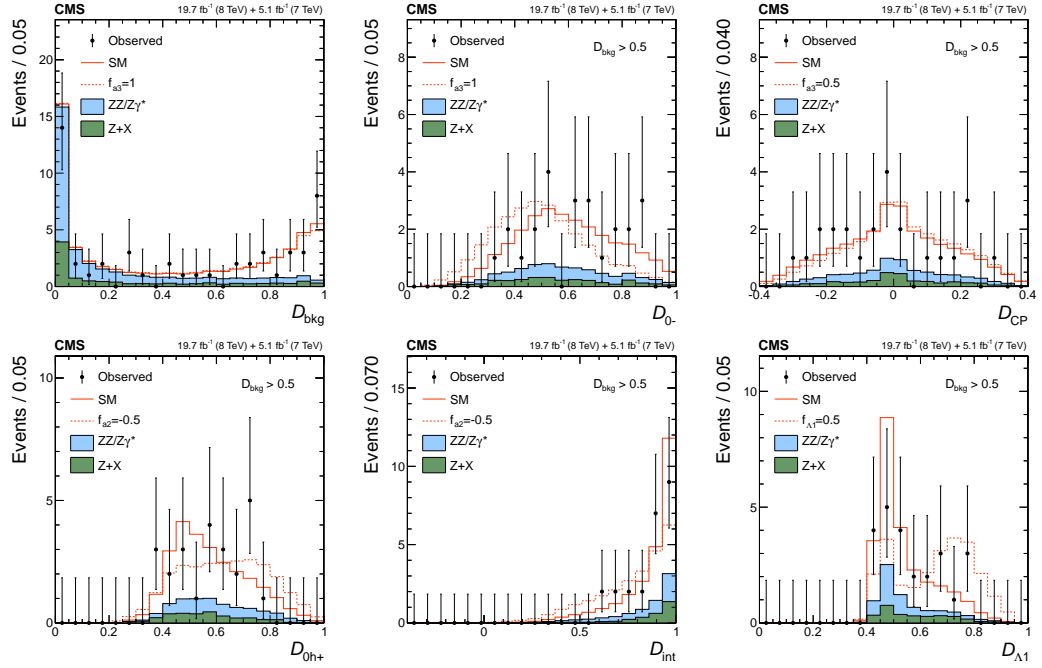


Figure 4.1: Distributions of the kinematic discriminants for the observed data (points with error bars), the expectations for the SM background (shaded areas), the SM H boson signal (open areas under the solid histogram), and the alternative spin-zero resonances (open areas under the dashed histograms) are shown, as indicated in the legend. The mass of the resonance is taken to be 125.6 GeV and the SM cross section is used. Top row from left to right: D_{bkg} , D_{0-} , D_{CP} ; bottom row from left to right: D_{0h+} , D_{int} , $D_{\Delta 1}$. All distributions, with the exception of D_{bkg} , are shown with the requirement $D_{\text{bkg}} > 0.5$ to enhance signal purity.

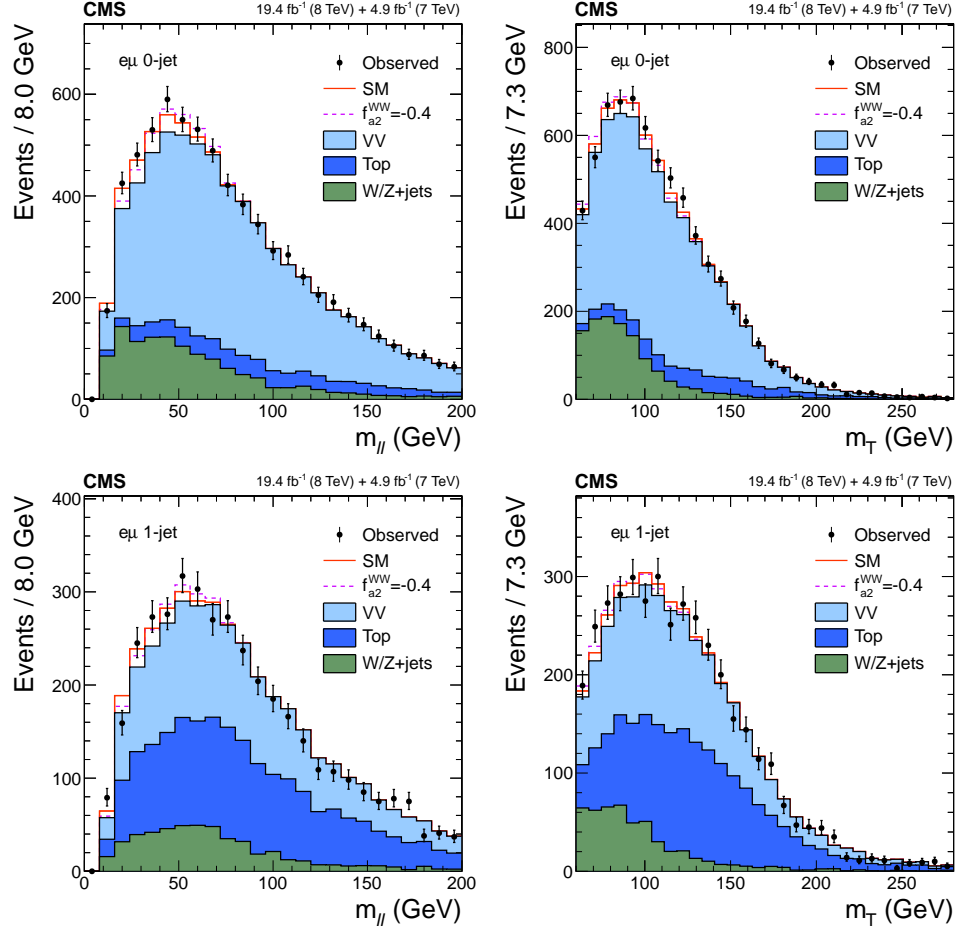


Figure 4.2: Distributions of $m_{\ell\ell}$ (left) and m_T (right) for events with 0 jets (upper row) and 1 jet (lower row) in the $WW \rightarrow \ell\nu\ell\nu$ analysis. The observed data (points with error bars), the expectations for the SM background (shaded areas), the SM H boson signal (open areas under the solid histogram), and the alternative spin-zero resonance (open areas under the dashed histograms) are shown, as indicated in the legend. The mass of the resonance is taken to be 125.6 GeV, and SM cross sections are used.

Table 4.1: List of observables used in the analysis of the anomalous HVV couplings for both the 4ℓ and $WW \rightarrow 2\ell 2\nu$ channels. The discriminant definitions are as discussed in Section 3.3. In the 4ℓ $f_{\Lambda 1}$ analysis, a $\mathcal{D}_{\Lambda 1, \text{int}}$ observable is correlated perfectly with $\mathcal{D}_{\Lambda 1}$, so \mathcal{D}_{0h+} is used as the third observable instead.

Measurement	Observables			
$f_{\Lambda 1}$	\mathcal{D}_{bkg}	$\mathcal{D}_{\Lambda 1}$	\mathcal{D}_{0h+}	
f_{a2}	\mathcal{D}_{bkg}	\mathcal{D}_{0h+}	\mathcal{D}_{int}	
f_{a3}	\mathcal{D}_{bkg}	\mathcal{D}_{0-}	\mathcal{D}_{CP}	
$f_{\Lambda 1}^{\text{WW}}$	m_{T}	$m_{\ell\ell}$		
f_{a2}^{WW}	m_{T}	$m_{\ell\ell}$		
f_{a3}^{WW}	m_{T}	$m_{\ell\ell}$		
$f_{\Lambda 1}^{\text{Z}\gamma}$	\mathcal{D}_{bkg}	$\mathcal{D}_{\Lambda 1}^{\text{Z}\gamma}$	$\mathcal{D}_{\text{int}}^{\text{Z}\gamma, \Lambda 1}$	
$f_{a2}^{\text{Z}\gamma}$	\mathcal{D}_{bkg}	$\mathcal{D}_{a2}^{\text{Z}\gamma}$	$\mathcal{D}_{\text{int}}^{\text{Z}\gamma}$	
$f_{a3}^{\text{Z}\gamma}$	\mathcal{D}_{bkg}	$\mathcal{D}_{a3}^{\text{Z}\gamma}$	$\mathcal{D}_{\text{CP}}^{\text{Z}\gamma}$	
$f_{a2}^{\gamma\gamma}$	\mathcal{D}_{bkg}	$\mathcal{D}_{a2}^{\gamma\gamma}$	$\mathcal{D}_{\text{int}}^{\gamma\gamma}$	
$f_{a3}^{\gamma\gamma}$	\mathcal{D}_{bkg}	$\mathcal{D}_{a3}^{\gamma\gamma}$	$\mathcal{D}_{\text{CP}}^{\gamma\gamma}$	

these observables are shown in Fig. 4.3. The categorization requirements are sequential and follow the logic below:

- **VBF-tagged** requires exactly four leptons, either two or three jets of which at most one is b quark flavor-tagged, or more if none are b-tagged, and $\mathcal{D}_{2\text{jet}}^{\text{VBF}} > 0.5$ using either SM or BSM signal hypothesis for the VBF production.
- **VH-tagged** requires exactly four leptons, either two or three jets, or more if none are b-tagged, and $\mathcal{D}_{2\text{jet}}^{\text{VH}} = \max \left(\mathcal{D}_{2\text{jet}}^{\text{ZH}}, \mathcal{D}_{2\text{jet}}^{\text{WH}} \right) > 0.5$ using either SM or BSM signal hypothesis for the VH production.
- **Untagged** consists of the remaining events.

Table 4.2: Summary of three production categories in the on-shell $m_{4\ell}$ region. The three observables (abbreviated as obs.) are listed for each analysis and category. The discriminants \mathcal{D}_{bkg} in the tagged categories also include probabilities using associated jets and decay at the same time in addition to the $m_{4\ell}$ probability. The VH interference discriminants in the hadronic VH-tagged categories are defined as the simple average of the ones corresponding to the ZH and WH processes. Observables for the on-shell region of the SM-like width analysis are also quoted, and they are further discussed in Section 4.3.

Category	VBF-tagged	VH-tagged	Untagged
Selection	$\mathcal{D}_{2\text{jet}}^{\text{VBF}}$ or $\mathcal{D}_{2\text{jet}}^{\text{VBF,BSM}} > 0.5$	$\mathcal{D}_{2\text{jet}}^{\text{ZH}}$ or $\mathcal{D}_{2\text{jet}}^{\text{ZH,BSM}}$, or $\mathcal{D}_{2\text{jet}}^{\text{WH}}$ or $\mathcal{D}_{2\text{jet}}^{\text{WH,BSM}} > 0.5$	Rest of events
SM obs.	$m_{4\ell}, \mathcal{D}_{\text{bkg}}^{\text{VBF+dec}}$	$m_{4\ell}, \mathcal{D}_{\text{bkg}}^{\text{VH+dec}}$	$m_{4\ell}, \mathcal{D}_{\text{bkg}}^{\text{kin}}$
a_3 obs.	$\mathcal{D}_{\text{bkg}},$ $\mathcal{D}_{0-}^{\text{VBF+dec}}, \mathcal{D}_{\text{CP}}^{\text{VBF}}$	$\mathcal{D}_{\text{bkg}},$ $\mathcal{D}_{0-}^{\text{VH+dec}}, \mathcal{D}_{\text{CP}}^{\text{VH}}$	$\mathcal{D}_{\text{bkg}},$ $\mathcal{D}_{0-}^{\text{dec}}, \mathcal{D}_{\text{CP}}^{\text{dec}}$
a_2 obs.	$\mathcal{D}_{\text{bkg}},$ $\mathcal{D}_{0h+}^{\text{VBF+dec}}, \mathcal{D}_{\text{int}}^{\text{VBF}}$	$\mathcal{D}_{\text{bkg}},$ $\mathcal{D}_{0h+}^{\text{VH+dec}}, \mathcal{D}_{\text{int}}^{\text{VH}}$	$\mathcal{D}_{\text{bkg}},$ $\mathcal{D}_{0h+}^{\text{dec}}, \mathcal{D}_{\text{int}}^{\text{dec}}$
Λ_1 obs.	$\mathcal{D}_{\text{bkg}},$ $\mathcal{D}_{\Lambda_1}^{\text{VBF+dec}}, \mathcal{D}_{0h+}^{\text{VBF+dec}}$	$\mathcal{D}_{\text{bkg}},$ $\mathcal{D}_{\Lambda_1}^{\text{VH+dec}}, \mathcal{D}_{0h+}^{\text{VH+dec}}$	$\mathcal{D}_{\text{bkg}},$ $\mathcal{D}_{\Lambda_1}^{\text{dec}}, \mathcal{D}_{0h+}^{\text{dec}}$
$\Lambda_1^{Z\gamma}$ obs.	$\mathcal{D}_{\text{bkg}},$ $\mathcal{D}_{\Lambda_1}^{Z\gamma, \text{VBF+dec}}, \mathcal{D}_{0h+}^{\text{VBF+dec}}$	$\mathcal{D}_{\text{bkg}},$ $\mathcal{D}_{\Lambda_1}^{Z\gamma, \text{VH+dec}}, \mathcal{D}_{0h+}^{\text{VH+dec}}$	$\mathcal{D}_{\text{bkg}},$ $\mathcal{D}_{\Lambda_1}^{Z\gamma, \text{dec}}, \mathcal{D}_{0h+}^{\text{dec}}$

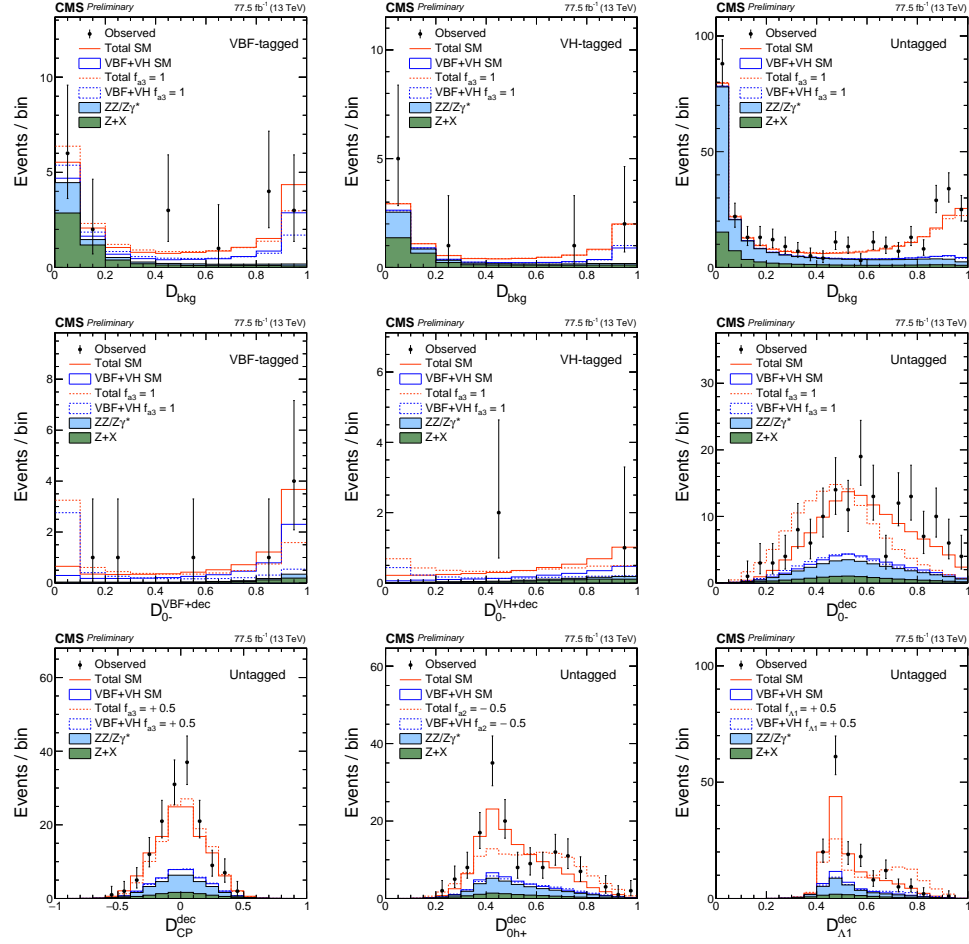


Figure 4.3: The distributions of events in the on-shell region. The top row shows D_{bkg} in the VBF-tagged (left), VH-tagged (middle), and untagged (right) categories of the a_3 analysis. The rest of the distributions are shown with the requirement $D_{\text{bkg}} > 0.5$ in order to enhance signal over background contributions. The middle row shows D_{0-} in the corresponding three categories. The bottom row shows $D_{\text{CP}}^{\text{dec}}$ of the a_3 , D_{0h+}^{dec} of the a_2 , and $D_{\Lambda_1}^{\text{dec}}$ of the Λ_1 analyses in the untagged categories.

4.1.3 Results from the combined Run 1 and Run 2 analysis

Table 4.3: Summary of allowed 68% CL (central values with uncertainties) and 95% CL (in square brackets) intervals on anomalous coupling parameters obtained from the combined Run 1 and Run 2 data analysis.

Parameter	Observed	Expected
$f_{a3} \cos(\phi_{a3})$	$-0.0001^{+0.0005}_{-0.0015} [-0.16, 0.09]$	$0.0000^{+0.0019}_{-0.0019} [-0.082, 0.082]$
$f_{a2} \cos(\phi_{a2})$	$0.0004^{+0.0026}_{-0.0007} [-0.006, 0.025]$	$0.0000^{+0.0030}_{-0.0023} [-0.021, 0.035]$
$f_{\Lambda 1} \cos(\phi_{\Lambda 1})$	$0.0000^{+0.0035}_{-0.0008} [-0.21, 0.09]$	$0.0000^{+0.0012}_{-0.0006} [-0.059, 0.032]$
$f_{\Lambda 1}^{Z\gamma} \cos(\phi_{\Lambda 1}^{Z\gamma})$	$0.000^{+0.355}_{-0.009} [-0.17, 0.61]$	$0.000^{+0.009}_{-0.010} [-0.10, 0.34]$

The final constraints on the anomalous HVV couplings from the combination of the Run 1 and Run 2 datasets are placed in terms of $f_{ai} \cos(\phi_{ai})$ with the profile likelihood method. In this method, the extended likelihood function is defined for N_{ev} candidate events as

$$\begin{aligned} \mathcal{L} = & \exp \left(- \sum_j n_{\text{sig}}^j - \sum_k n_{\text{bkg}}^k \right) \\ & \times \prod_i^{N_{\text{ev}}} \left(\sum_j n_{\text{sig}}^j \mathcal{P}_{\text{sig}}^j(\vec{x}_i; \vec{\xi}_j) + \sum_k n_{\text{bkg}}^k \mathcal{P}_{\text{bkg}}^k(\vec{x}_i; \vec{\xi}_k) \right), \end{aligned} \quad (4.1)$$

where n_{sig}^j is the number of signal events of a certain type j , n_{bkg}^k is the number of background events of a certain type k , and \vec{x} is the set of observables in Tables 4.1 and 4.2. The signal probability density functions $\mathcal{P}_{\text{sig}}^j$ are described as a collection of histogram templates scaled with different powers of a_i/a_1 according to how many terms arise from having one or two HVV vertices. In the Run 1 portion of the analysis, possible contributions from the HVV production side are absorbed by simply scaling the cross section, leaving only template variations due to variations in decay kinematics, but the parameterization

allows for different ϕ_{ai} values other than 0 or π , or for variation of shapes by two separate f_{ai} fractions. The $\mathcal{P}_{\text{bkg}}^k$ background contributions are described as single templates. The likelihood parameterization is constructed independently in each of the $4e$, 4μ , or $2e2\mu$ final states, different data taking periods, or the different production categories of the Run 2 analysis. The parameters $\vec{\xi}_j$ for the signal and $\vec{\xi}_k$ for the background processes include parameterization uncertainties, but $\vec{\xi}_j$ also includes $f_{ai} \cos(\phi_{ai})$ (Run 1 or Run 2), or f_{ai} and ϕ_{ai} (only Run 1) as parameters of interest. While not explicitly indicated in Eqn. 4.1, the parameters $\vec{\xi}_j$ and $\vec{\xi}_k$ also change the numbers of signal and background, respectively. The likelihood in Eqn. 4.1 is maximized with respect to the parameters $\vec{\xi}_j$ and $\vec{\xi}_k$, which constitute the nuisance parameters and the parameters of interest. The nuisance parameters are either constrained within the associated uncertainties or left unconstrained in the fit.

Four $f_{ai} \cos(\phi_{ai})$ parameters sensitive to anomalous HVV interactions are tested in the combined on-shell data sample with the assumption $\cos(\phi_{ai}) = \pm 1$. Figure 4.4 shows the results of the likelihood scans of these parameters for the 2016 and 2017 periods of the 13 TeV run and for the full, combined dataset from collisions at 7, 8, and 13 TeV, and a summary of these results is presented in Table 4.3. The allowed 68% and 95% CL intervals are defined using the respective profile likelihood function values $-2 \ln(\mathcal{L}/\mathcal{L}_{\text{max}}) = 1.00$ and 3.84. Exact coverage at these intervals is expected in the asymptotic limit [137], and the approximate coverage presented through the profile likelihood method has been tested on the Run 1 parameterizations and found to be equivalent.

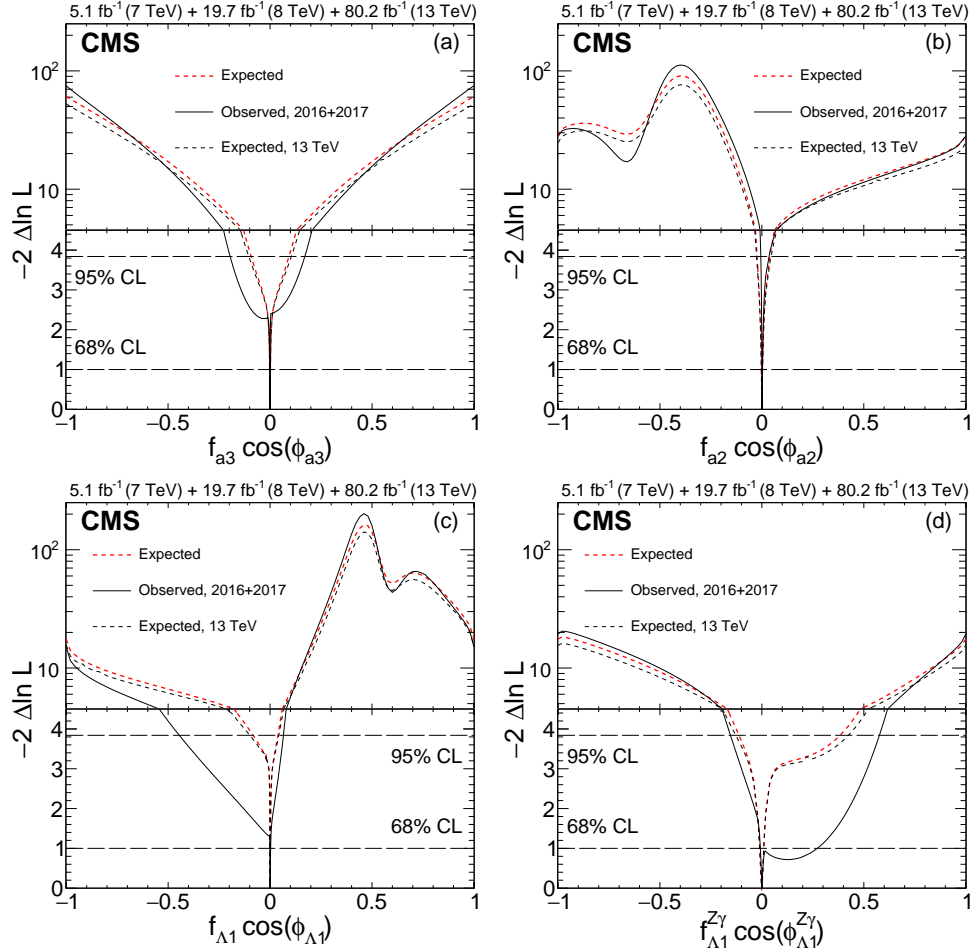


Figure 4.4: Observed (solid) and expected (dashed) likelihood scans of $f_{a3} \cos(\phi_{a3})$ (top-left), $f_{a2} \cos(\phi_{a2})$ (top-right), $f_{\Lambda 1} \cos(\phi_{\Lambda 1})$ (bottom-left), and $f_{\Lambda 1}^{Z\gamma} \cos(\phi_{\Lambda 1}^{Z\gamma})$ (bottom-right) using on-shell events only. Results of analysis of the data from 2016 and 2017 only (black) and the combined Run 1 and Run 2 analysis (red) are shown. The dashed horizontal lines show the 68% and 95% CL regions.

4.1.4 Additional results using only Run 1 events

Table 4.4: Summary of allowed 68% CL (central values with uncertainties) and 95% CL (in square brackets) intervals on anomalous coupling parameters obtained from only the Run 1 data analysis.

Parameter	Observed	Expected
Constraints on $f_{ai} \cos(\phi_{ai})$ using 4ℓ events		
$f_{a3} \cos(\phi_{a3})$	$0.00^{+0.14}_{-0.11} [-0.40, 0.43]$	$0.00^{+0.33}_{-0.33} [-0.70, 0.70]$
$f_{a2} \cos(\phi_{a2})$	$0.00^{+0.41}_{-0.06} [-0.66, -0.57]$ $\cup [-0.15, 1.00]$	$0.00^{+0.38}_{-0.08} [-0.18, 1.00]$
$f_{\Lambda 1} \cos(\phi_{\Lambda 1})$	$0.22^{+0.10}_{-0.16} [-0.25, 0.37]$	$0.00^{+0.16}_{-0.87} [-1.00, 0.27]$ $\cup [0.92, 1.00]$
Constraints on $f_{ai}^{WW} \cos(\phi_{ai}^{WW})$ using $WW \rightarrow \ell\nu\ell\nu$ events		
$f_{a3}^{WW} \cos(\phi_{a3}^{WW})$	$-0.03^{+1.03}_{-0.97} [-1.00, 1.00]$	$0.00^{+1.00}_{-1.00} [-1.00, 1.00]$
$f_{a2}^{WW} \cos(\phi_{a2}^{WW})$	$-0.02^{+1.02}_{-0.16} [-1.00, -0.54]$ $\cup [-0.29, 1.00]$	$0.00^{+1.00}_{-0.12} [-1.00, -0.58]$ $\cup [-0.22, 1.00]$
$f_{\Lambda 1}^{WW} \cos(\phi_{\Lambda 1}^{WW})$	$0.21^{+0.18}_{-1.21} [-1.00, 1.00]$	$0.00^{+0.34}_{-1.00} [-1.00, 0.41]$ $\cup [0.49, 1.00]$
Constraints on $f_{ai}^{Z\gamma} \cos(\phi_{ai}^{Z\gamma})$ using 4ℓ events		
$f_{a3}^{Z\gamma} \cos(\phi_{a3}^{Z\gamma})$	$0.02^{+0.21}_{-0.13} [-0.40, 0.51]$	$0.00^{+0.51}_{-0.51} [-0.75, 0.75]$
$f_{a2}^{Z\gamma} \cos(\phi_{a2}^{Z\gamma})$	$0.00^{+0.14}_{-0.20} [-0.49, 0.46]$	$0.00^{+0.51}_{-0.51} [-0.78, 0.79]$
Constraints on $f_{ai}^{\gamma\gamma} \cos(\phi_{ai}^{\gamma\gamma})$ using 4ℓ events		
$f_{a2}^{\gamma\gamma} \cos(\phi_{a2}^{\gamma\gamma})$	$0.12^{+0.20}_{-0.11} [-0.04, +0.51]$	$0.00^{+0.11}_{-0.09} [-0.32, 0.34]$
$f_{a3}^{\gamma\gamma} \cos(\phi_{a3}^{\gamma\gamma})$	$-0.02^{+0.06}_{-0.13} [-0.35, 0.32]$	$0.00^{+0.15}_{-0.11} [-0.37, 0.40]$

In the Run 1 analysis of anomalous HVV couplings, additional constraints for the $HZ\gamma$ and $H\gamma\gamma$ couplings are also derived from the 4ℓ events as a function of $f_{ai} \cos(\phi_{ai})$. These constraints are shown in Fig. 4.5. In addition, results from the combination of ZZ and WW decay are derived for the cases

where the quantity

$$r_{ai} = \frac{a_i^{WW}/a_1^{WW}}{a_i/a_1}, \text{ or } R_{ai} = \frac{r_{ai}|r_{ai}|}{1 + r_{ai}^2} \quad (4.2)$$

is constrained based on custodial symmetry (i.e. $r_{ai} = 1$ or $R_{ai} = 0.5$), or varied for the respective $f_{ai} \cos(\phi_{ai})$ in the scan. Constraints on $f_{ai} \cos(\phi_{ai})$ from ZZ and WW decay conditional on the value of R_{ai} are illustrated in Fig. 4.6, and $f_{ai} \cos(\phi_{ai})$ constraints at $R_{ai} = 0.5$ are shown in Fig. 4.7. The different results are summarized in Table 4.4.

One-parameter likelihood scans in terms of f_{ai} with ϕ_{ai} unconstrained are also considered in the Run 1 analysis as well as two parameter likelihood scans in terms of two different $f_{ai} \cos(\phi_{ai})$ parameters. f_{ai} constraints with unconstrained ϕ_{ai} are illustrated in Fig. 4.8 while results with two different $f_{ai} \cos(\phi_{ai})$ as parameters are shown in Fig. 4.9. Figure 4.6 finally illustrates the likelihood scans in $f_{ai} \cos(\phi_{ai})$ using the combination of Z and WW events, conditional on a given value of the R_{ai} parameter described in Eqn. 4.2. In the full two-parameter likelihood scans, the allowed 68% and 95% CL intervals are defined using the respective profile likelihood function values $-2 \ln(\mathcal{L}/\mathcal{L}_{\max}) = 2.3$ and 5.99.

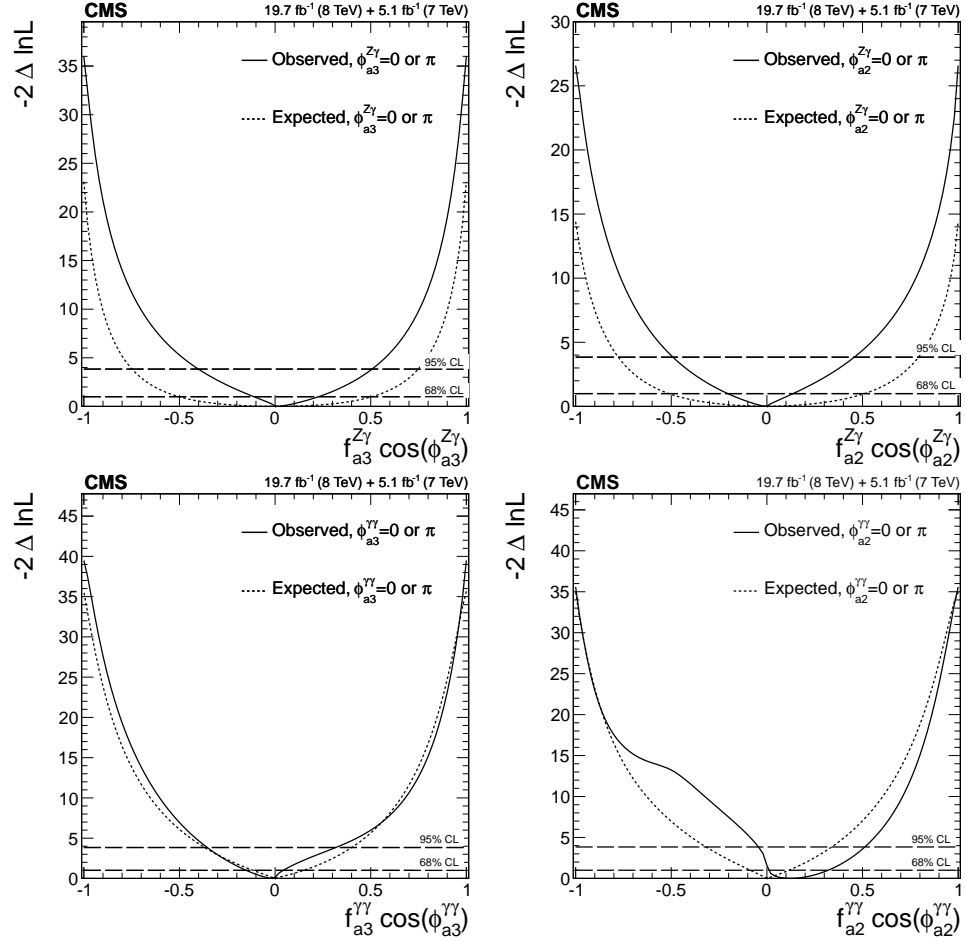


Figure 4.5: Observed (solid) and expected (dashed) likelihood scans of the various $f_{ai} \cos(\phi_{ai})$ are shown for anomalous $HZ\gamma$ couplings (top), and anomalous $H\gamma\gamma$ couplings (bottom). Left panels show the relevant f_{a3} scans whereas right panels show the f_{a2} scans. These results are derived from Run 1 4ℓ events.

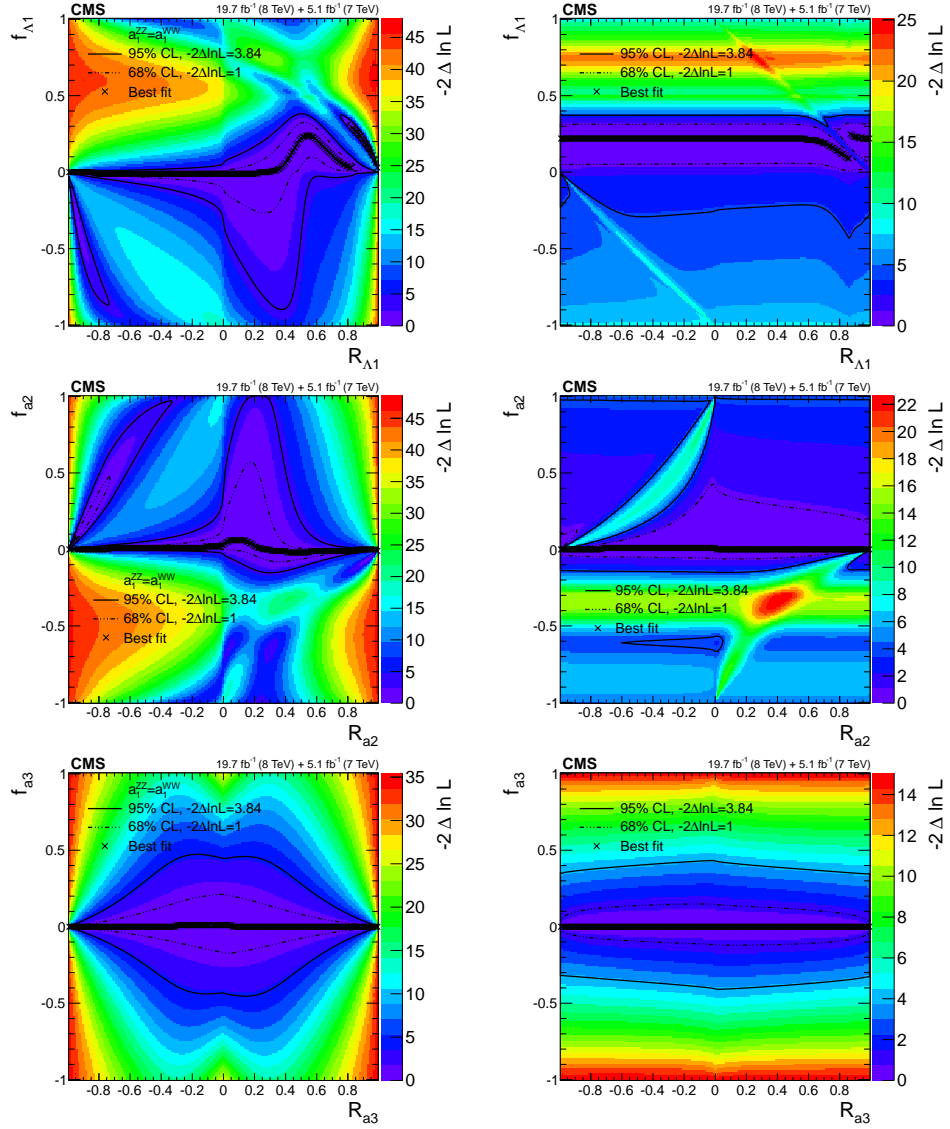


Figure 4.6: Observed conditional likelihood scans of $f_{\Lambda 1}$ (top), f_{a2} (middle), f_{a3} (bottom) for a given R_{ai} value from the combined analysis of the $H \rightarrow WW$ and $H \rightarrow ZZ$ channels using the template method. The results are shown with custodial symmetry $a_1 = a_1^{WW}$ (left) and without such an assumption (right). Each cross indicates the minimum value of $-2\Delta\ln\mathcal{L}$ and the contours indicate the one-parameter confidence intervals of f_{ai} for a given value of R_{ai} .

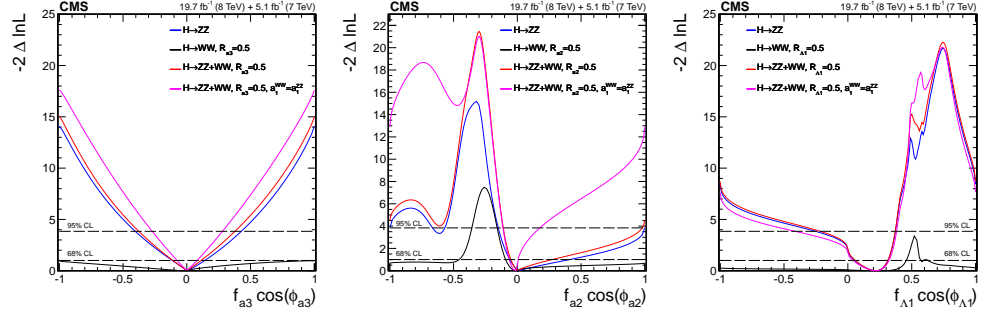


Figure 4.7: Observed (solid) and expected (dashed) likelihood scans of the various $f_{ai} \cos(\phi_{ai})$ are shown for anomalous HZZ couplings combining with HWW decay under the assumption $R_{ai} = 0.5$. Constraints from 4ℓ events is also shown for comparison. These results are derived from only the Run 1 analysis.

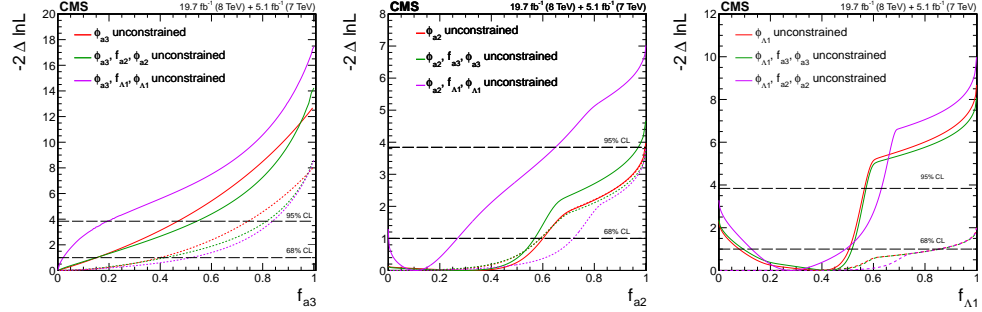


Figure 4.8: Expected (dashed) and observed (solid) likelihood scans for the effective fractions f_{a3} , f_{a2} , and $f_{\Lambda 1}$ (from left to right) with ϕ_{ai} unconstrained. The f_{a3} result with ϕ_{a3} unconstrained in the left plot is from Ref. [72].

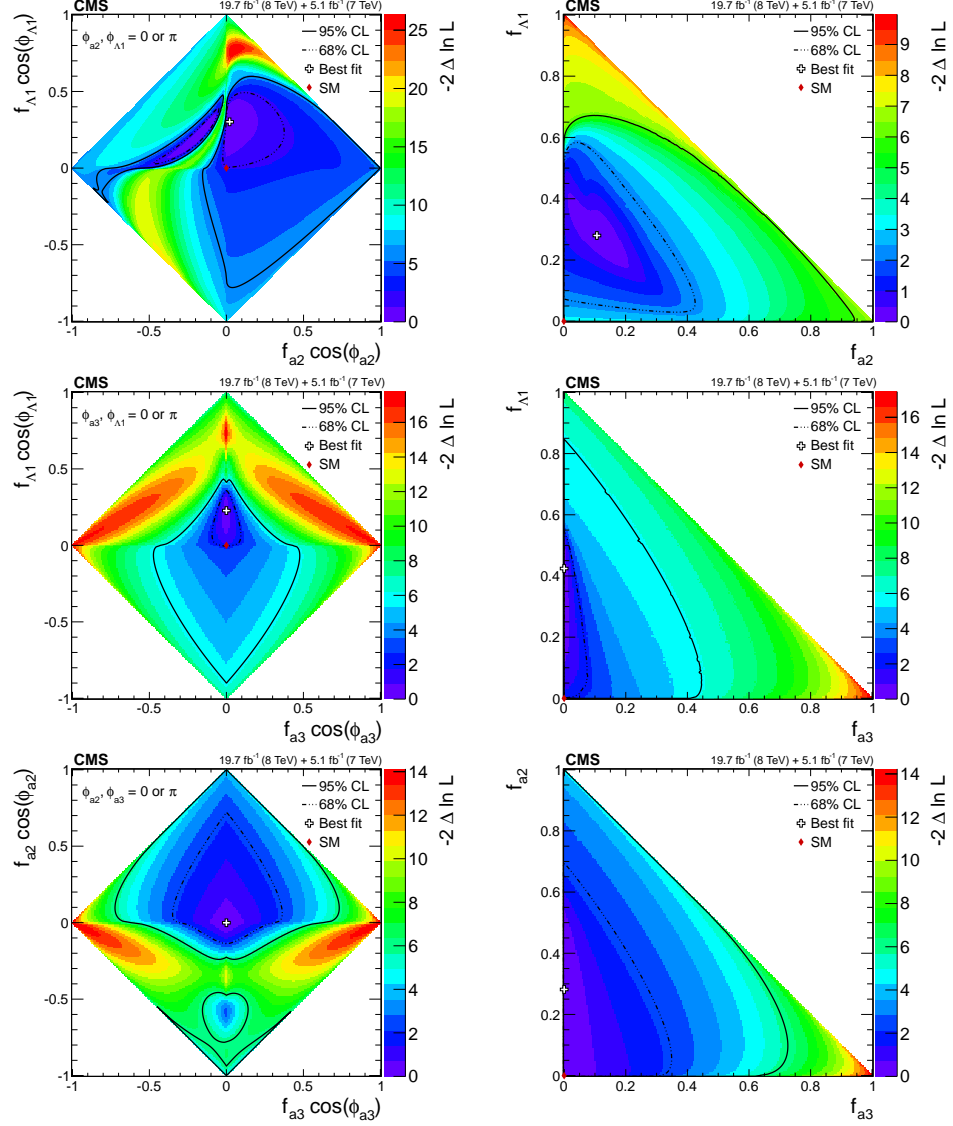


Figure 4.9: Observed likelihood scans for pairs of effective fractions $f_{\Lambda 1}$ vs. f_{a2} , $f_{\Lambda 1}$ vs. f_{a3} , and f_{a2} vs. f_{a3} (from top to bottom) describing HZZ interactions. Plots on the left show the results when the couplings studied are constrained to be real and all other couplings are fixed to the SM predictions. Plots on the right show the results when the phases of the anomalous couplings are left unconstrained. The SM expectations correspond to points (0,0) and the best fit values are shown with the crosses. The confidence level intervals are indicated by the corresponding $-2 \Delta \ln \mathcal{L}$ contours.

4.2 Lifetime analysis from on-shell Higgs boson production

The measurement of the H boson lifetime is derived from its flight distance in the CMS detector from Run 1 data [98]. Since full kinematic information is present, the lifetime of a H boson candidate in its rest frame can be determined in four-lepton decay as

$$\Delta t = \frac{m_{4\ell}}{p_T} (\Delta \vec{r}_T \cdot \hat{p}_T), \quad (4.3)$$

where $m_{4\ell}$ is the four-lepton invariant mass, $\Delta \vec{r}_T$ is the displacement vector between the decay vertex and the production vertex of the H boson in the plane transverse to the beam axis. p_T is the transverse momentum of the H boson, and \hat{p}_T is its unit direction vector. The expectation value of Δt is inversely proportional to the total width Γ_H :

$$\langle \Delta t \rangle = \tau_H = \frac{\hbar}{\Gamma_H}. \quad (4.4)$$

The distribution of the measured lifetime Δt is used to set an upper limit on the average lifetime of the H boson, or equivalently a lower limit on its width Γ_H . Δt follows the exponential distribution if known perfectly, but vertex resolution of the detector may smear it to both positive and negative values. One could use the total momentum of the H boson in place of the transverse momentum in Eqn. 4.3, but sensitivity on displacement measurement along the beam axis is much worse than sensitivity along the transverse plane. Therefore, the analysis chooses not to use components along the beam axis. The reference point for the H boson production vertex is taken to be the

beam spot, which is the proton-proton collision point determined by fitting charged-particle tracks from events in multiple collisions, so the value of $\Delta\vec{r}_T$ is calculated as the displacement from the beam spot to the 4ℓ vertex in the plane transverse to the beam axis. An alternative calculation of Δt could also been considered using the primary vertex of each event instead of the beam spot, but the different associated particles in the H boson production and their multiplicity would introduce additional model dependence in the primary vertex resolution and thus on the distribution of Δt in these production modes.

Trigger, object identification and selection are identical to Ref. [72] except the requirement on $\text{SIP}_{3\text{D}}$ for electrons and muons. This requirement does not allow for a displaced vertex, so in order to constrain the lifetime of the H boson, the reference of the comparison is switched from the primary vertex of the event to the vertex formed by the two leptons from the Z_1 candidate ($\text{SIP}_{3\text{D}}^{Z_1}$). The two leptons from Z_1 are required to satisfy $\text{SIP}_{3\text{D}}^{Z_1} < 4$, and the remaining two leptons are required to satisfy $\text{SIP}_{3\text{D}}^{Z_1} < 5$. An additional requirement $\chi_{4\ell}^2/\text{dof} < 6$ for the four-lepton vertex is applied to further suppress the $Z + X$ background. This background may include displaced vertices due to b-quark jets and is evaluated using tight-to-loose lepton misidentification methods on the observed control samples as discussed in Ref. [72]. While the misidentification rates are consistent between the two different vertex selection requirements, the overall number of selected $Z + X$ background events is about 15% higher when using the vertex requirements of the lifetime measurement. The number of prompt-decay signal and background events is about 2% higher with these lifetime measurement requirements, and the

number of signal events with large lifetime are the same as in the number of prompt-decay signal events.

In addition to the standard simulation samples discussed in Section 3.3, four different values of the H boson lifetime have been generated with $c\tau_H = 0, 100, 500, 1000 \mu\text{m}$ for the gluon fusion production mechanism, and these samples are reweighted to model the values of lifetime in between the generated values. Making use of the fact that Δt is determined with respect to the beam spot without model dependence on the multiplicity of particles associated with H boson production, the only difference between gluon fusion and the other production mechanisms relevant for the constraint on the lifetime is the H boson p_T spectrum. Hence, reweighting this spectrum allows the modeling of Δt in different production mechanisms with nonzero H boson lifetime. In all signal hypotheses, the simulation uses $m_H = 125.6 \text{ GeV}$ as the mass of the H boson.

The expected and observed distributions of Δt used in the analysis are illustrated in Fig. 4.10. The lifetime analysis also uses \mathcal{D}_{bkg} with decay-only information as the observable to discriminate background against signal. The distribution of this discriminant does not change significantly with large H boson lifetime values in the signal, and its distribution is also shown in Fig. 4.10. The distributions of p_T^H and Δt in different production modes are also illustrated.

Uncertainties in the Δt distribution for the signal and the prompt background are obtained from a comparison of the expected and observed distributions in the $m_{4\ell}$ sidebands, $70 < m_{4\ell} < 105.6 \text{ GeV}$ and $170 < m_{4\ell} < 800 \text{ GeV}$.

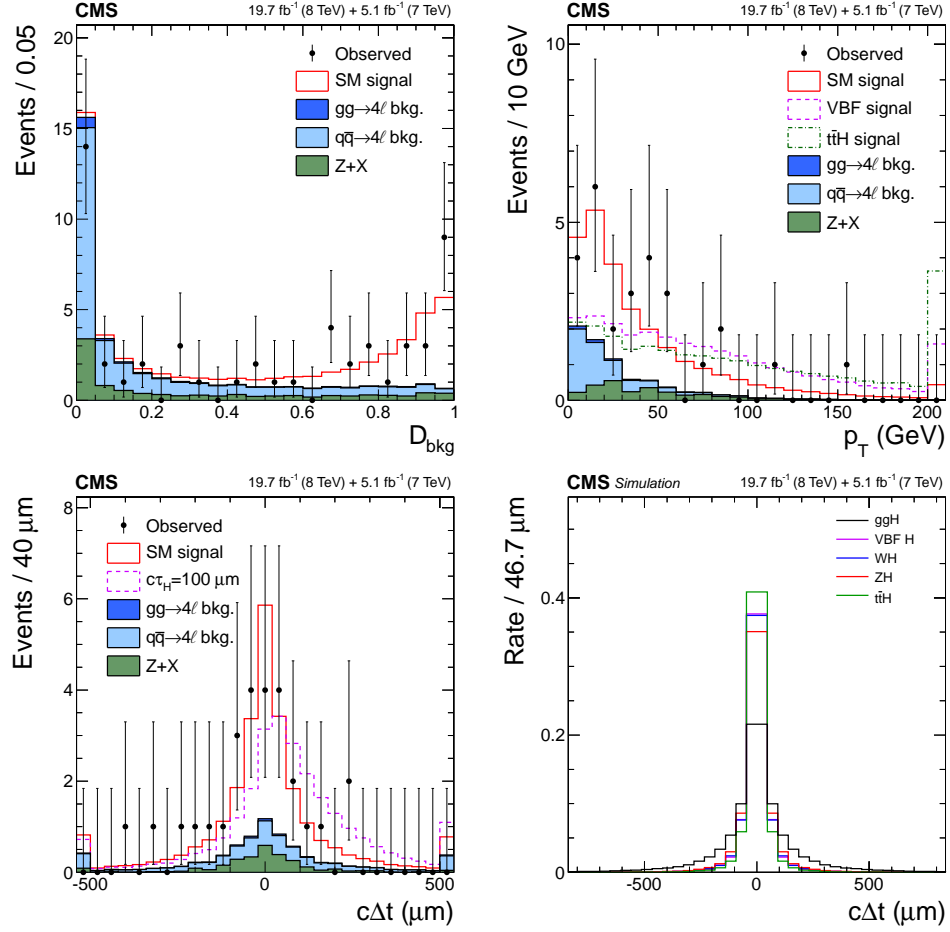


Figure 4.10: Top panels: Distribution of D_{bkg} (left) and p_T^H (right). When showing p_T^H distributions, $D_{\text{bkg}} > 0.5$ is required to enhance the signal contribution, and comparison between the distributions of the SM mixture, a VBF-only and a $t\bar{t}H$ -only production hypothesis with the same number of events are also illustrated. Bottom panels: Distributions of $c\Delta t$ constructed using p_T^H and transverse displacement quantities. The left panel shows the expected contributions from the SM backgrounds and the additional signal contributions under prompt decay or the hypothesis $c\tau_H = 100 \mu\text{m}$. The right panel compares the distribution of different signal production modes. The first and last bins of the $c\Delta t$ distributions include all events beyond the boundary of these bins.

These uncertainties obtained from this comparison correspond to varying the Δt resolution by $+17/-15\%$, $+14/-12\%$, and $+20/-17\%$ for the $4e$, 4μ , and $2e2\mu$ final states, respectively. The $Z + X$ parameterization is obtained from the control region in the analysis mass range $105.6 < m_{4\ell} < 140.6$ GeV, and its alternative parameterization obtained from the control region events in the mass range $140.6 < m_{4\ell} < 170$ GeV reflects the uncertainties in the data-driven estimate. A cross-check of the Δt distributions is also performed with the 3ℓ control samples enriched in WZ prompt decay, and the distributions are found to be consistent with simulation.

The final constraints on the H boson lifetime $c\tau_H$ are placed with the profile likelihood method. The extended likelihood function is defined in the same way as in Eqn. 4.1. Each probability density function \mathcal{P}_{sig} for signal and $\mathcal{P}_{\text{bkg}}^k$ for the background processes are likewise described as histogram templates, and $\vec{\zeta}$ in the case of this analysis also includes τ_H as the parameter of interest.

Figure 4.11 shows the likelihood distribution as a function of $c\tau_H$. The approximate coverage from the profile likelihood method has been tested with the generated samples at different $c\tau_H$ values, and the shown results have been found to be conservative. The observed (expected) average lifetime is $c\tau_H = 2_{-2}^{+25}$ (0_{-0}^{+24}) μm ($\tau_H = 10_{-10}^{+80}$ fs for the observation and $\tau_H = 0_{-0}^{+80}$ fs for the expectation), and the allowed region at the 95% CL is $c\tau_H < 57$ (56) μm ($\tau_H < 190$ fs for both the observation and the expectation). The observed number of signal events remains consistent with Ref. [72]. The observed (expected) upper limit on the average lifetime at 95% CL corresponds through Eqn. 4.4 to the lower limit on the H boson width $\Gamma_H > 3.5 \times 10^{-9}$ MeV

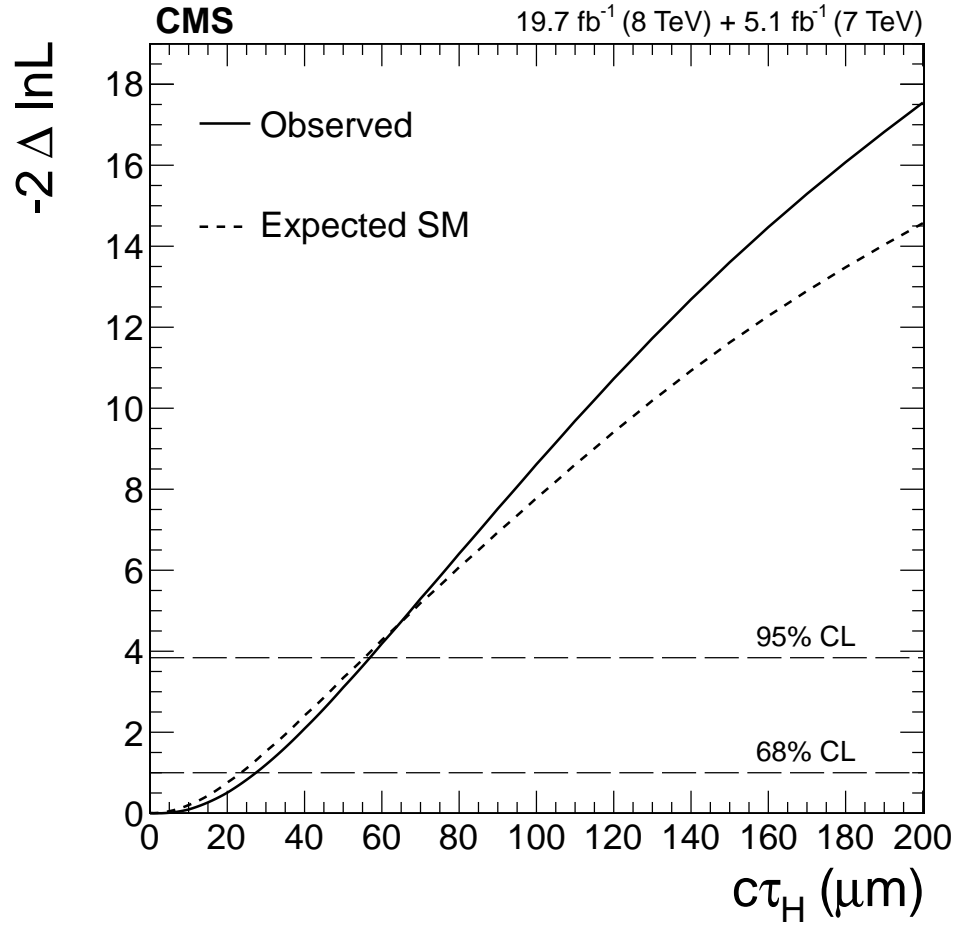


Figure 4.11: Observed (solid) and expected (dashed) distributions of $-2 \ln(\mathcal{L}/\mathcal{L}_{\max})$ as a function of the H boson average lifetime $c\tau_H$.

($\Gamma_H > 3.6 \times 10^{-9}$ MeV). The upper bounds on τ_H are consistent with the SM value of 48 fm/c (16×10^8 fs).

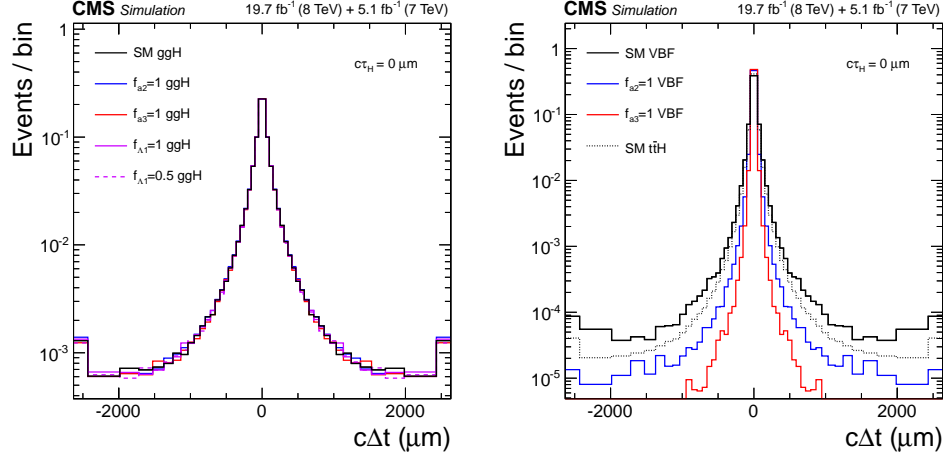


Figure 4.12: Variations of Δt signal resolution shape due to differences in the p_T spectrum of different H boson production modes. The left panel shows variations for different anomalous HVV couplings in 4ℓ decay using gluon fusion production, which illustrates that anomalous HVV couplings on the decay side do not affect H boson p_T and hence the distribution of Δt . The right panel shows variations of anomalous HVV couplings in the VBF and VH production mechanisms and compares it to the SM VBF and $t\bar{t}H$ production mechanism. In the presence of anomalous HVV couplings, the p_T spectrum from VBF and VH (not shown) are harder than their corresponding SM counterparts.

The Δt and \mathcal{D}_{bkg} distributions have little variation within the allowed range of exotic couplings in the $H \rightarrow 4\ell$ decay. The expected τ_H constraint remains stable within 10% when the simulation for those exotic models is tested instead of the simulation with SM couplings. Anomalous couplings in production are found to have a substantial effect on the p_T spectrum, typically making the spectrum harder in the VBF, VH, and $t\bar{t}H$ production mechanisms. These hypotheses are illustrated in Fig. 4.12. Extreme variations in the p_T spectrum, however, are already excluded by the data as illustrated in Fig. 4.10. Nevertheless, we allow extreme variations in the Δt parameterization to

account for any variations in the H boson p_T spectrum by taking the SM gluon fusion-only and SM $t\bar{t}H$ -only hypotheses as two extremes with respect to the SM mixture of production mechanisms. This variation provides enough coverage of model dependence on H boson production.

4.3 Width and spin-parity analysis combining off-shell events

As discussed in Section 3.4, off-shell H boson production in ZZ or WW final states is sensitive to small changes in both H boson total width, Γ_H , and anomalous HVV couplings. The methodology of the analysis combines the anomalous coupling formalism in Section 3.1, and the off-shell width technique in Section 3.4. In the Run 1 measurements, only SM-like couplings are considered with the exception of Λ_Q , and in the Run 2 analysis, anomalous couplings a_2 , a_3 and Λ_1 are constrained in addition to Γ_H using the combination of on-shell and off-shell events.

4.3.1 On-shell parameterization in the combined width and spin-parity analysis

The on-shell parameterization of the likelihood is the same as in Eqn. 4.1 with the inclusion of $f_{ai} \cos(\phi_{ai})$ as the parameter of interest. Γ_H does not change this on-shell likelihood per the off-shell method. The observables used in the on-shell region of this analysis remains the same as in Table 4.1 for the Run 1 or 2015 datasets, and Table 4.2 for the 2016 and 2017 datasets. The Run 1 observables of the SM-like analysis, which are not explicitly quoted in

Table 4.1, are $m_{4\ell}$, $\mathcal{D}_{\text{bkg}}^{\text{kin}}$, and either $\mathcal{D}_{2\text{jet}}^{\text{VBF}}$ for events with more than one jet or $p_{\text{T}}^{4\ell}$ for the remaining events.

In contrast to the approach based fully on templates in the on-shell parameterization of anomalous HVV couplings analyses, the on-shell region of the SM-like width analysis can use parametric signal $m_{4\ell}$ shapes whereas the treatment of the backgrounds are still based on binned histograms as templates that include the $m_{4\ell}$ shape information. The signal probability density for each process is parameterized separately as the product of a double-sided Crystal-Ball function and templates of other discriminants conditional in $m_{4\ell}$. The double-sided Crystal-Ball function [138–140] is defined as

$$dCB(\xi) = N \cdot \begin{cases} A \cdot (B + |\xi|)^{-n_L}, & \text{for } \xi < \alpha_L \\ A \cdot (B + |\xi|)^{-n_R}, & \text{for } \xi > \alpha_R \\ \exp(-\xi^2/2), & \text{for } \alpha_L \leq \xi \leq \alpha_R \end{cases} \quad (4.5)$$

where $\xi = (m_{4\ell} - m_{\text{H}} - \Delta m)/\sigma_m$. This function has six independent parameters, and is intended to capture the Gaussian core of the four-lepton mass resolution function and the left- and right-hand tails originating from bremsstrahlung in the tracker material and from the non-Gaussian mis-measurements originating from interactions of the leptons with the detector material. The parameters A and B are not independent; they are defined by requiring the continuity of the function itself and its first derivatives. N is a normalization constant. The parameter Δm for the peak shift is modified by a separate nuisance parameter for electrons and muons to vary for the lepton energy and momentum scales, and the parameter σ_m is modified likewise by a separate nuisance parameter to vary for lepton energy and momentum resolutions.

Uncertainties in the lepton momentum arise from imperfect calibration of

the ECAL supercluster and uncertainty in the GSF track fit due to possible high-bremsstrahlung emissions in the case of the electrons, and from the uncertainty in the muon track fit due to the multiple scattering of the muons in the material of the inner tracker. For use in the Δm and σ_m parameters in Eqn. 4.5, the uncertainties are reduced to a basis of lepton scale and resolution uncertainties. The scale uncertainties are derived from $Z \rightarrow 2\ell$ events during Run 2, and they are derived from Z , $\Upsilon(nS)$ ($n = 1, 2, 3$) and J/ψ dilepton resonances in Run 1 to reach lower lepton p_T ranges. Figure 4.13 illustrates the derived uncertainties in the 2012 and 2016 datasets in different p_T and η bins. An envelope of 0.3% for electrons in $4e$ decay and 0.1% for muons in 4μ decay is applied conservatively to cover for the effect of lepton scale uncertainty on $m_{4\ell}$ at different p_T and η values in both Run 1 and Run 2 datasets, and the electron and muon uncertainties are adjusted for the less number of leptons in $2e2\mu$ decay.

The per-event mass uncertainties are calculated as the sum in quadrature of the individual mass uncertainty contributions from each lepton and any identified FSR photon candidate. After several corrections to account for differences between data and simulation for the approximations involved in its calculation, this per-event uncertainty is supposed to equal the resolution on $m_{4\ell}$ under the Gaussian approximation. As shown in Fig. 4.14, comparison in dilepton events between the measured and predicted per-event errors, relative to the dilepton mass, yields differences that are covered by a $\pm 20\%$ uncertainty envelope in all 4ℓ decay channels even after the corrections are applied. Therefore, this uncertainty is used in place of the smaller uncertainties obtained

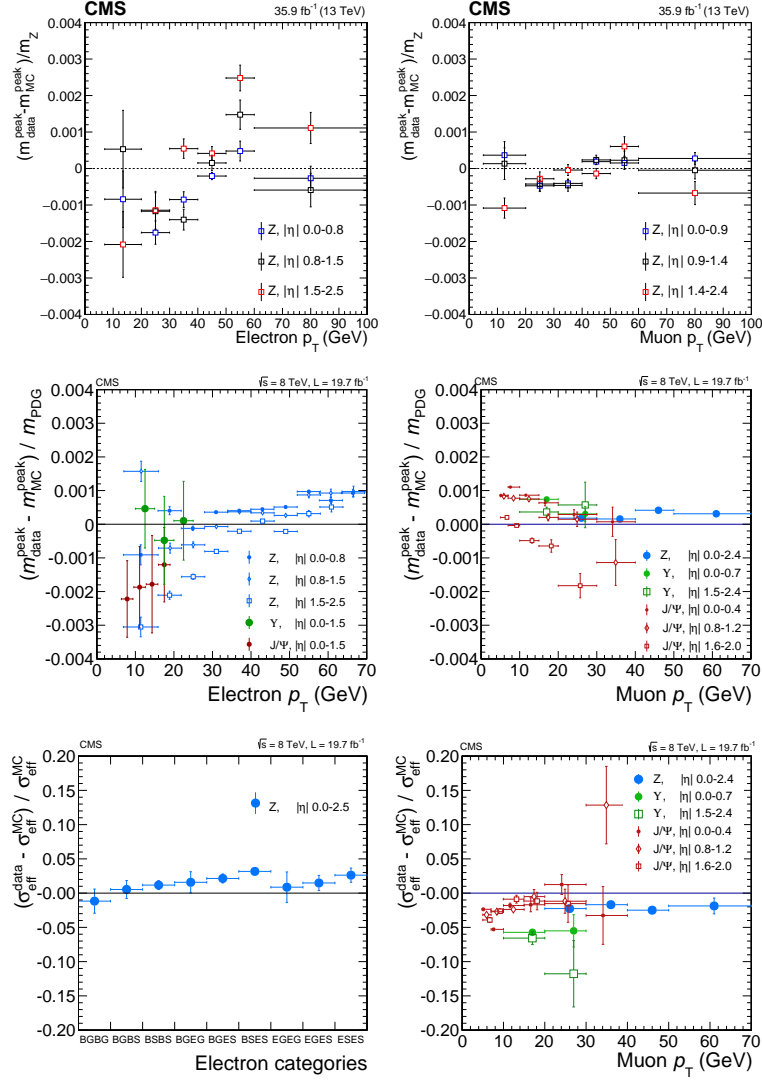


Figure 4.13: The relative difference between data and simulation in the location of the peak or in the width of the dilepton resonance mass lineshape for electrons (left plots) and muons (right plots). The difference in peak locations is used as a measure of the lepton energy and momentum scale uncertainty, and the difference in the width is used as a measure of the lepton energy and momentum resolution uncertainty. The top row shows the scale comparisons done on the 2016 dataset, the middle row shows the scale comparisons done on the 2012 dataset, and the bottom row shows the resolution comparisons done on the 2012 dataset. All comparisons are done in bins of p_T and η of a lepton chosen randomly while the other lepton is integrated [72, 74].

from the comparison of data and simulation dilepton mass resolution widths, which are illustrated in the bottom panels of Fig. 4.13 for the 2012 dataset. The per-event mass errors are not used directly in the parameterization of on-shell events in the SM-like width analysis.

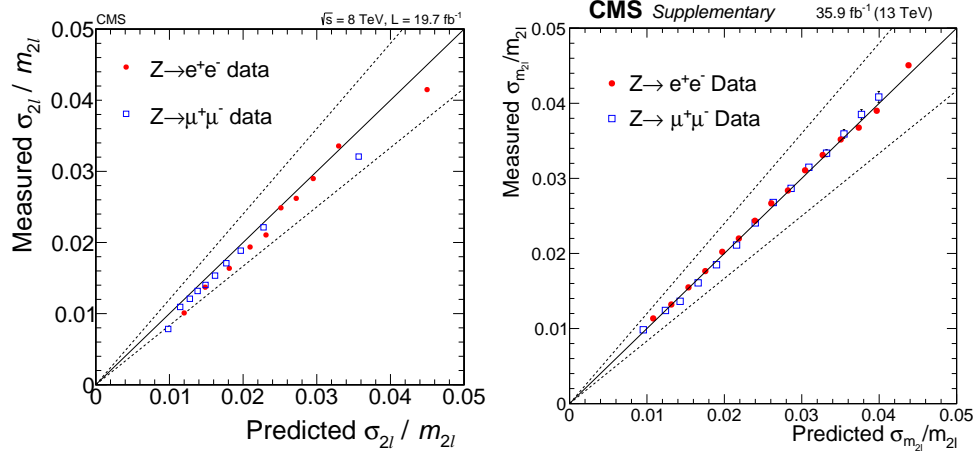


Figure 4.14: The comparison of predicted and measured relative per-event dilepton mass error in the 2012 (left, from Ref. [72]) and 2016 (right, from Ref. [74]) datasets is shown in bins of predicted relative per-event mass error. The predicted error is calculated with the uncorrelated momentum errors on the individual leptons, corrected by calibration constants to introduce the correlation. The measured error comes from the parameterization of the dilepton resonance as a Breit-Wigner convoluted with a double-sided Crystal-Ball function. The same uncertainty envelope of $\pm 20\%$ taken to be the final resolution uncertainty in the different 4ℓ decay channels.

4.3.2 Off-shell parameterization in the combined width and spin-parity analysis

The off-shell parameterization of the likelihood replaces \mathcal{P}_{sig} with $\mathcal{P}_{\text{total}}$, which is defined as

$$\begin{aligned}\mathcal{P}_{\text{total}}(\vec{x}; \vec{\xi}) &= (\mu_i \cdot \Gamma_H / \Gamma_0) \mathcal{P}_{\text{sig}}(\vec{x}; \vec{\xi}) \\ &+ \sqrt{\mu_i \cdot \Gamma_H / \Gamma_0} \mathcal{P}_{\text{int}}(\vec{x}; \vec{\xi}) \\ &+ \mathcal{P}_{\text{bkg}}(\vec{x}; \vec{\xi}).\end{aligned}\tag{4.6}$$

μ_i is either μ_F for scaling the ggH, ttH and bbH production mechanisms, or μ_V for scaling the VBF and VH production mechanisms. $f_{ai} \cos(\phi_{ai})$ is included in the set of parameters $\vec{\xi}$ that modify signal or interference contributions. $\Gamma_0 = 4.15$ MeV is used in the Run 1 analysis, and $\Gamma_0 = 4.07$ MeV is used in the Run 2 analysis as a result of the change in the m_H value from 125.6 GeV to 125 GeV.

In the Run 1 analysis, the observables \vec{x} in the off-shell region are $m_{4\ell}$ and \mathcal{D}_{gg} , which defined as

$$\mathcal{D}_{\text{gg}} = \frac{10 \times \mathcal{P}_{\text{sig}}^{\text{gg}} + \sqrt{10} \times \mathcal{P}_{\text{int}}^{\text{gg}} + \mathcal{P}_{\text{bkg}}^{\text{gg}}}{10 \times \mathcal{P}_{\text{sig}}^{\text{gg}} + \sqrt{10} \times \mathcal{P}_{\text{int}}^{\text{gg}} + \mathcal{P}_{\text{bkg}}^{\text{gg}} + \mathcal{P}_{\text{bkg}}^{\text{q}\bar{\text{q}}}}\tag{4.7}$$

The coefficient 10 is chosen as the approximate sensitivity of the Run 1 analysis to $\Gamma_H / \Gamma_H^{\text{SM}}$ [98, 141]. Categorization is done only as VBF-tagged or untagged, determining the VBF-tagged category with the simple $\mathcal{D}_{2\text{jet}}^{\text{VBF}} > 0.5$ requirement [98].

Categorization requirements in the Run 2 analysis are identical to the anomalous couplings scheme presented in Section 4.1.2. The observables are chosen such that all analyses can separate signal and background contributions optimally and are sensitive to Γ_H -dependent signal and signal-background interference effects in the SM-like analysis, and in addition to pure BSM HVV contributions in the anomalous coupling analyses. These observables are listed in Table 4.5, and exemplary distributions are shown in Fig. 4.15.

Table 4.5: Summary of the three production categories and the observables \vec{x} in the off-shell $m_{4\ell}$ region, listed in a similar manner to Table 4.2. The \mathcal{D}_{bsi} discriminant is only used in the SM-like analysis off-shell region; it is sensitive to the interference between the SM signal and background for the primary signal process targeted in each category.

Category	VBF-tagged	VH-tagged	Untagged
Selection	$\mathcal{D}_{2\text{jet}}^{\text{VBF}}$ or $\mathcal{D}_{2\text{jet}}^{\text{VBF,BSM}} > 0.5$	$\mathcal{D}_{2\text{jet}}^{\text{ZH}}$ or $\mathcal{D}_{2\text{jet}}^{\text{ZH,BSM}}$, or $\mathcal{D}_{2\text{jet}}^{\text{WH}}$ or $\mathcal{D}_{2\text{jet}}^{\text{WH,BSM}} > 0.5$	Rest of events
SM obs.	$m_{4\ell},$ $\mathcal{D}_{\text{bkg}}^{\text{VBF+dec}}, \mathcal{D}_{\text{bsi}}^{\text{VBF+dec}}$	$m_{4\ell},$ $\mathcal{D}_{\text{bkg}}^{\text{VH+dec}}, \mathcal{D}_{\text{bsi}}^{\text{VH+dec}}$	$m_{4\ell},$ $\mathcal{D}_{\text{bkg}}^{\text{kin}}, \mathcal{D}_{\text{bsi}}^{\text{gg,dec}}$
a_3 obs.	$m_{4\ell},$ $\mathcal{D}_{\text{bkg}}^{\text{VBF+dec}}, \mathcal{D}_{0-}^{\text{VBF+dec}}$	$m_{4\ell},$ $\mathcal{D}_{\text{bkg}}^{\text{VH+dec}}, \mathcal{D}_{0-}^{\text{VH+dec}}$	$m_{4\ell},$ $\mathcal{D}_{\text{bkg}}^{\text{kin}}, \mathcal{D}_{0-}^{\text{dec}}$
a_2 obs.	$m_{4\ell},$ $\mathcal{D}_{\text{bkg}}^{\text{VBF+dec}}, \mathcal{D}_{0h+}^{\text{VBF+dec}}$	$m_{4\ell},$ $\mathcal{D}_{\text{bkg}}^{\text{VH+dec}}, \mathcal{D}_{0h+}^{\text{VH+dec}}$	$m_{4\ell},$ $\mathcal{D}_{\text{bkg}}^{\text{kin}}, \mathcal{D}_{0h+}^{\text{dec}}$
Λ_1 obs.	$m_{4\ell},$ $\mathcal{D}_{\text{bkg}}^{\text{VBF+dec}}, \mathcal{D}_{\Lambda_1}^{\text{VBF+dec}}$	$m_{4\ell},$ $\mathcal{D}_{\text{bkg}}^{\text{VH+dec}}, \mathcal{D}_{\Lambda_1}^{\text{VH+dec}}$	$m_{4\ell},$ $\mathcal{D}_{\text{bkg}}^{\text{kin}}, \mathcal{D}_{\Lambda_1}^{\text{dec}}$

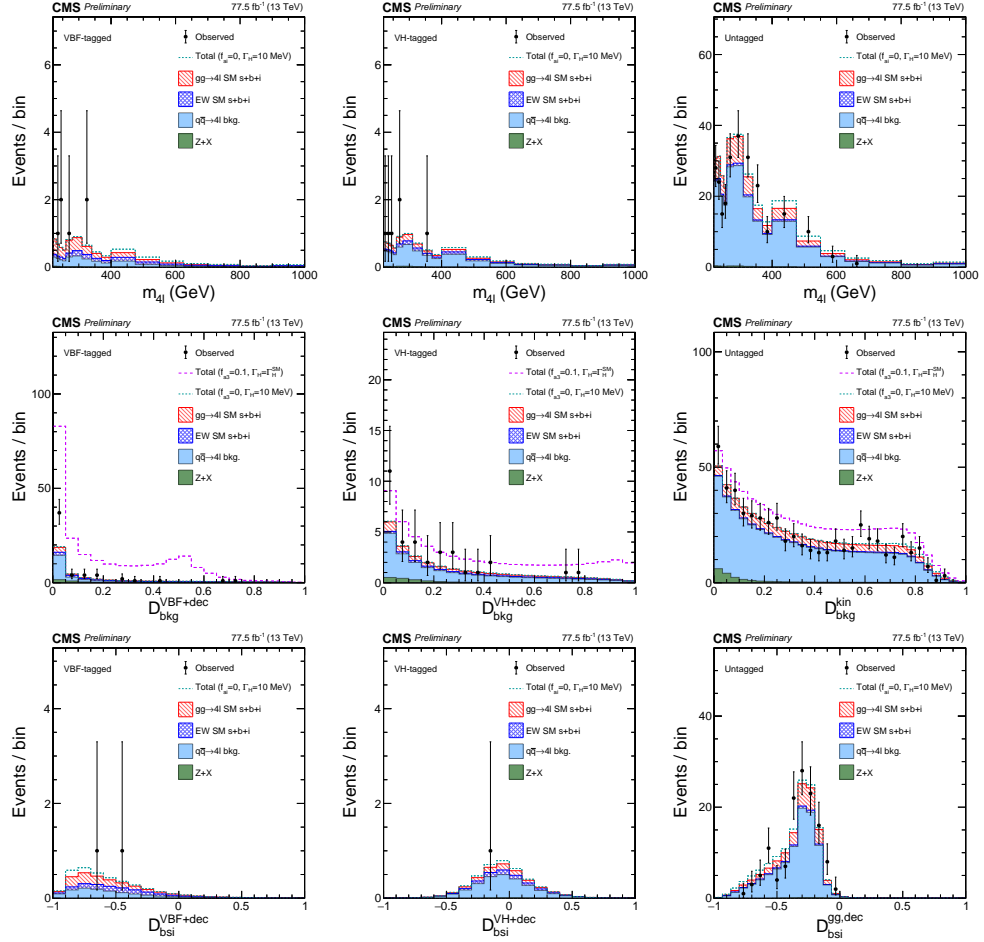


Figure 4.15: The distributions of events in the off-shell region. The top row shows $m_{4\ell}$ in the VBF-tagged (left), VH-tagged (middle), and untagged (right) categories in the dedicated SM-like width analysis where a requirement on $\mathcal{D}_{\text{bkg}}^{\text{VBF+dec}}$, $\mathcal{D}_{\text{bkg}}^{\text{VH+dec}}$, or $\mathcal{D}_{\text{bkg}}^{\text{kin}} > 0.6$ is applied in order to enhance signal over background contributions. The middle row shows $\mathcal{D}_{\text{bkg}}^{\text{VBF+dec}}$ (left), $\mathcal{D}_{\text{bkg}}^{\text{VH+dec}}$ (middle), $\mathcal{D}_{\text{bkg}}^{\text{kin}}$ (right) of the a_3 analysis in the corresponding three categories. The requirement $m_{4\ell} > 340$ GeV is applied in order to enhance signal over background contributions. The bottom row shows \mathcal{D}_{bsi} in the corresponding three categories in the dedicated SM-like width analysis with both of the $m_{4\ell}$ and $\mathcal{D}_{\text{bkg}}^{\text{kin}}$ requirements enhancing the signal contribution.

4.3.3 Results of the Run 1 analysis

Constraints are placed either on Γ_H under the hypothesis of SM-like couplings, or on $f_{\Lambda Q}$ for the SM value of Γ_H , or on both parameters jointly. The observed distribution of the likelihood as a two-parameter function of Γ_H and $f_{\Lambda Q} \cos \phi_{\Lambda Q}$, with $\phi_{\Lambda Q} = 0$ or π , is shown in Fig. 4.16. Also shown is the one-parameter, conditional likelihood scan of $f_{\Lambda Q} \cos \phi_{\Lambda Q}$ for a given Γ_H , where the $-2 \ln(\mathcal{L}/\mathcal{L}_{\max})$ distribution is shown for \mathcal{L}_{\max} adjusted according to the most likely value of $f_{\Lambda Q} \cos \phi_{\Lambda Q}$ at the given value of Γ_H . The observed and expected likelihood distributions as a function of Γ_H are shown in Fig. 4.17, where $f_{\Lambda Q}$ is either constrained to zero or left unconstrained. The observed (expected) central values with 68% CL uncertainties are $\Gamma_H = 2_{-2}^{+9} (4_{-4}^{+17})$ MeV with $f_{\Lambda Q} = 0$, and $\Gamma_H = 2_{-2}^{+15} (4_{-4}^{+30})$ MeV with $f_{\Lambda Q}$ unconstrained and $\phi_{\Lambda Q} = 0$ or π . The observed (expected) constraints at 95% CL are $\Gamma_H < 26 (41)$ MeV with $f_{\Lambda Q} = 0$, and $\Gamma_H < 46 (73)$ MeV with $f_{\Lambda Q}$ unconstrained and $\phi_{\Lambda Q} = 0$ or π . The constraints on $f_{\Lambda Q} \cos \phi_{\Lambda Q}$ given particular Γ_H values become tighter for increasing Γ_H . The limits on $f_{\Lambda Q} \cos \phi_{\Lambda Q}$ with the assumption $\Gamma_H = \Gamma_H^{\text{SM}}$ are also presented in Fig. 4.17. The observed (expected) value is $f_{\Lambda Q} \cos \phi_{\Lambda Q} = 0_{-0.4}^{+1.0} (0_{-0.4}^{+1.1}) \times 10^{-3}$, and the allowed region at 95% CL is $[-2.4, 3.8] \times 10^{-3} ([-3.6, 4.4] \times 10^{-3})$ [98, 141].

The Γ_H constraints with $f_{\Lambda Q} = 0$ can be re-parameterized into off-shell signal strengths $\mu_i^{\text{off-shell}} = \mu_i \Gamma_H / \Gamma_H^{\text{SM}}$, provided the signal strength μ_i for the on-shell region is uncorrelated with the signal strength $\mu_i^{\text{off-shell}}$ for the off-shell region in the likelihood scan. With this re-parameterization, the observed (expected) central values and the 68% CL uncertainties of Γ_H constraints

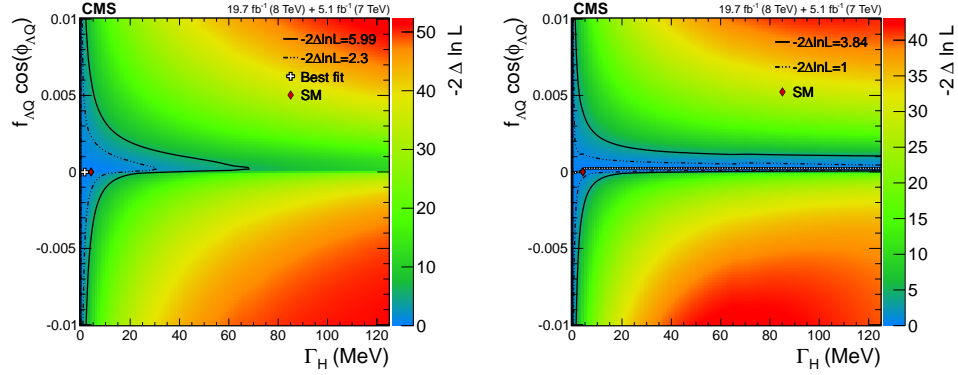


Figure 4.16: Observed distribution of $-2\ln(\mathcal{L}/\mathcal{L}_{\max})$ as a function of Γ_H and $f_{\Lambda Q} \cos \phi_{\Lambda Q}$ with the assumption $\phi_{\Lambda Q} = 0$ or π (left panel). The right panel shows the observed conditional likelihood scan as a function of $f_{\Lambda Q} \cos \phi_{\Lambda Q}$ for a given Γ_H . The likelihood contours are shown for the two-parameter 68% and 95% CL_s (left) and for the one-parameter 68% and 95% CL_s (right). The black curve with white dots on the right panel shows the $f_{\Lambda Q} \cos \phi_{\Lambda Q}$ minima at each Γ_H value. Only 4ℓ events from the Run 1 datasets are used in the results presented [98].

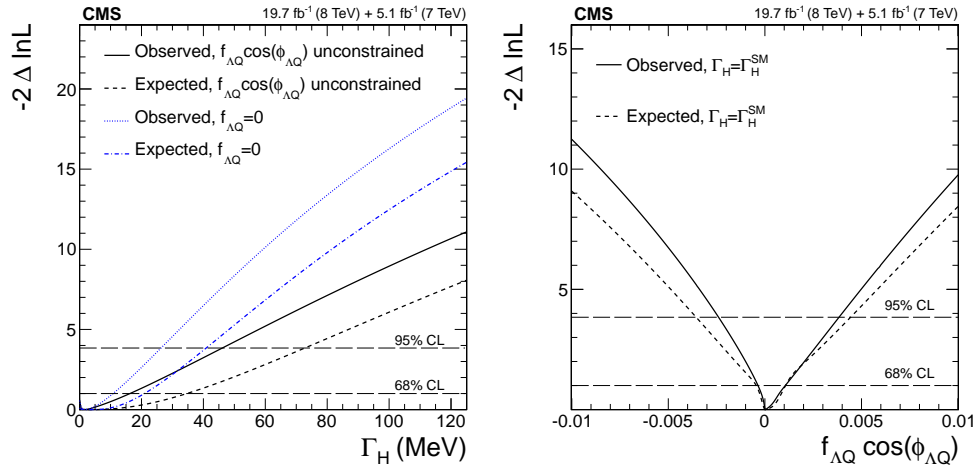


Figure 4.17: Observed (solid) and expected (dashed) distributions of $-2\ln(\mathcal{L}/\mathcal{L}_{\max})$ as a function of Γ_H (left) and $f_{\Lambda Q} \cos \phi_{\Lambda Q}$ (right). On the left panel, the $f_{\Lambda Q}$ value is either constrained to zero (blue) or left unconstrained (black, weaker limit), while $\Gamma_H = \Gamma_H^{\text{SM}}$ and $\phi_{\Lambda Q} = 0$ or π are assumed on the right. Only 4ℓ events from the Run 1 datasets are used in the results presented [98].

with the $f_{\Lambda Q} = 0$ correspond to $\mu_F^{\text{off-shell}} = 0.5_{-0.5}^{+2.2}$ ($1.0_{-1.0}^{+5.1}$) and $\mu_V^{\text{off-shell}} = 0.4_{-0.4}^{+10.5}$ ($1.0_{-1.0}^{+20.6}$), and the observed (expected) constraints at 95% CL become $\mu_F^{\text{off-shell}} < 6.2$ (9.3) and $\mu_V^{\text{off-shell}} < 31.3$ (44.4).

4.3.4 Results of the Run 2 analysis

Table 4.6: Summary of allowed 68% CL (central values with uncertainties) and 95% CL (in square brackets) intervals on the anomalous coupling parameters $f_{ai} \cos(\phi_{ai})$ obtained from the analysis of the combination of Run 2 2016 and 2017 datasets (on-shell and off-shell), and Run 1 and Run 2 2015 (only on-shell) datasets. Different constraint scenarios are shown using the combination of on-shell and off-shell events by either unconstraining the value of Γ_H or setting it to $\Gamma_H = \Gamma_H^{\text{SM}}$.

Parameter	Observed	Expected
Unconstrained Γ_H		
$f_{a3} \cos(\phi_{a3})$	$0.0000_{-0.0010}^{+0.0003} [-0.0165, 0.0087]$	$0.0000_{-0.0015}^{+0.0015} [-0.0377, 0.0377]$
$f_{a2} \cos(\phi_{a2})$	$0.0004_{-0.0006}^{+0.0026} [-0.0035, 0.0147]$	$0.0000_{-0.0017}^{+0.0019} [-0.0152, 0.0214]$
$f_{\Lambda 1} \cos(\phi_{\Lambda 1})$	$0.0001_{-0.0006}^{+0.0015} [-0.0904, 0.0589]$	$0.0000_{-0.0007}^{+0.0013} [-0.0172, 0.0194]$
$\Gamma_H = \Gamma_H^{\text{SM}}$		
$f_{a3} \cos(\phi_{a3})$	$0.0000_{-0.0009}^{+0.0003} [-0.0067, 0.0050]$	$0.0000_{-0.0014}^{+0.0014} [-0.0098, 0.0098]$
$f_{a2} \cos(\phi_{a2})$	$0.0005_{-0.0006}^{+0.0025} [-0.0029, 0.0129]$	$0.0000_{-0.0016}^{+0.0012} [-0.0100, 0.0118]$
$f_{\Lambda 1} \cos(\phi_{\Lambda 1})$	$0.0001_{-0.0005}^{+0.0015} [-0.0162, 0.0682]$	$0.0000_{-0.0006}^{+0.0013} [-0.0154, 0.0178]$

Three $f_{ai} \cos(\phi_{ai})$ parameters, f_{a3} , f_{a2} and $f_{\Lambda 1}$, are tested together with Γ_H in the combination of on-shell and off-shell regions. As discussed above, the on-shell region is analyzed in the 2015, 2016 and 2017 runs, and the earlier Run 1 data. The off-shell region is analyzed only using 2016 and 2017 data because no such analysis of the four anomalous couplings has been performed with Run 1 or Run 2 2015 data. The one-parameter likelihood scans of $f_{ai} \cos(\phi_{ai})$ combining all such available on-shell and off-shell events is shown for two cases in Fig. 4.18, either unconstraining the value of Γ_H in the fit or

setting its value to $\Gamma_H = \Gamma_H^{\text{SM}}$. The corresponding 68% and 95% CLs are summarized in Table 4.6. The full two-parameter likelihood scans of $f_{ai} \cos(\phi_{ai})$ and Γ_H are likewise shown in Fig. 4.18. The $f_{ai} \cos(\phi_{ai})$ constraints using off-shell events are much tighter than those presented in Table 4.3 due to the enhancements effects of anomalous HVV couplings in the off-shell region.

Limits on Γ_H are set by combining events from the on-shell and off-shell regions. Figure 4.19 left panel shows the results of the likelihood scans of Γ_H for the 2016 and 2017 period of the 13 TeV run and for the full combined dataset from collisions at 7, 8 and 13 TeV under the assumption of SM-like couplings. These combined results are listed in Table 4.7, where the Run 1 analysis includes both on-shell and off-shell regions in the analysis of the $H \rightarrow ZZ \rightarrow 4\ell$ decay [98, 141]. The best fitted (μ_V, μ_F) values in these results are $(0.62^{+0.57}_{-0.43}, 1.20^{+0.19}_{-0.16})$ when $\Gamma_H = \Gamma_H^{\text{SM}}$, and $(0.65^{+0.61}_{-0.45}, 1.21^{+0.19}_{-0.17})$ when Γ_H is unconstrained. The Γ_H constraints are also obtained with the $f_{a3} \cos(\phi_{a3})$, $f_{a2} \cos(\phi_{a2})$, or $f_{\Lambda 1} \cos(\phi_{\Lambda 1})$ parameters unconstrained and are shown in Figure 4.19 right panel and in Table 4.7. These results are obtained using combination of Run 1 and Run 2 data with a small difference from the above fit with SM-like couplings. There is no analysis of off-shell data with anomalous couplings, therefore only on-shell data are used in anomalous coupling fit with Run 1 data. On the other hand, 2015 data are included in the on-shell anomalous couplings study only. While the expected Γ_H constraints are similar but somewhat looser with the unconstrained anomalous coupling parameters, fluctuations in the data lead to somewhat tighter observed constraints.

Similar to the case of the Run 1 off-shell analysis presented in Section 4.3.3,

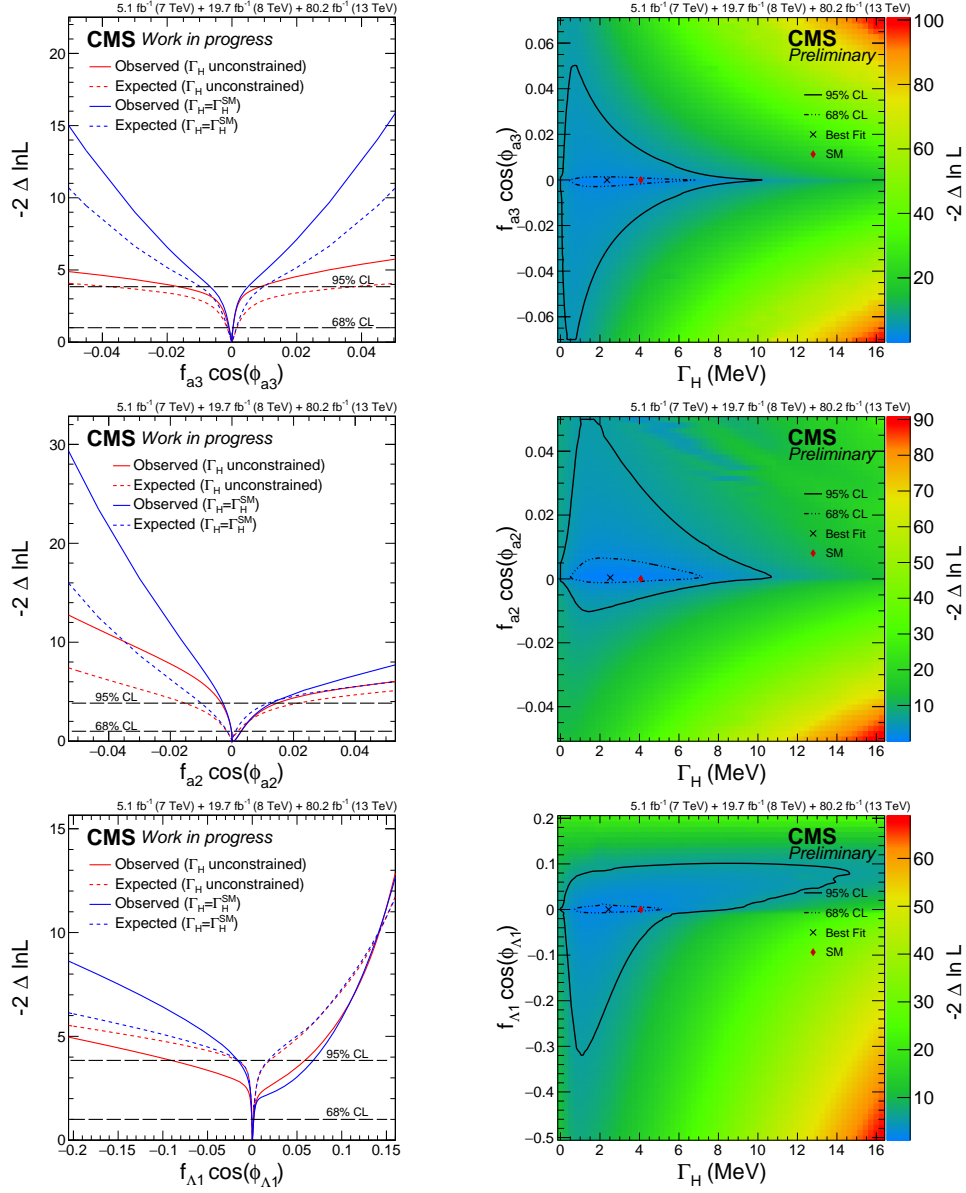


Figure 4.18: Constraints on $f_{a3} \cos(\phi_{a3})$ (top), $f_{a2} \cos(\phi_{a2})$ (middle), and $f_{\Lambda 1} \cos(\phi_{\Lambda 1})$ (bottom) from the combined Run 1 and Run 2 dataset with different assumptions on Γ_H . Left plots: Results of the analysis by either unconstraining the value of Γ_H (red) or assuming $\Gamma_H = \Gamma_H^{\text{SM}}$ (blue). The dashed horizontal lines show the 68% and 95% CL regions. Observed likelihood scans are shown with solid curves whereas the expected scans are shown with dashed ones. Right plots: Observed two-parameter likelihood scans in Γ_H (x-axis) and $f_{ai} \cos(\phi_{ai})$ (y-axis). The two-parameter 68% and 95% CL regions are indicated with the dashed and solid curves, respectively.

Table 4.7: Summary of the total width Γ_H measurements, showing allowed 68% CL (central values with uncertainties) and 95% CL (in square brackets). The Γ_H limits are reported for the SM-like configuration or for an unconstrained anomalous coupling parameter of interest using the Run 1 and Run 2 combination.

Parameter	Free parameter	Observed	Expected
Γ_H (MeV)	SM-like	$3.2^{+2.8}_{-2.2}$ [0.08, 9.16]	$4.1^{+5.0}_{-4.0}$ [0.0, 13.7]
Γ_H (MeV)	$f_{a3} \cos(\phi_{a3})$	$2.4^{+2.7}_{-1.8}$ [0.02, 8.38]	$4.1^{+5.2}_{-4.1}$ [0.0, 13.9]
Γ_H (MeV)	$f_{a2} \cos(\phi_{a2})$	$2.5^{+2.9}_{-1.8}$ [0.02, 8.76]	$4.1^{+5.2}_{-4.1}$ [0.0, 13.9]
Γ_H (MeV)	$f_{\Lambda 1} \cos(\phi_{\Lambda 1})$	$2.4^{+2.5}_{-1.6}$ [0.06, 7.84]	$4.1^{+5.2}_{-4.1}$ [0.0, 13.9]

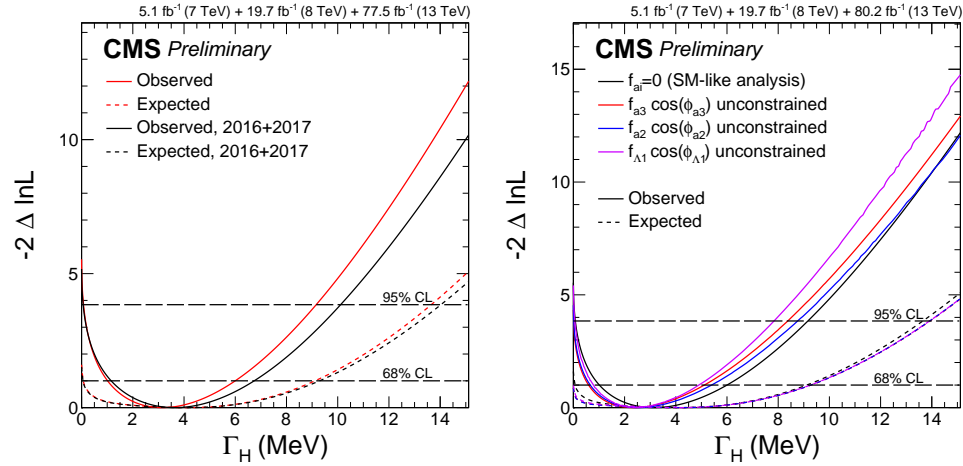


Figure 4.19: Observed (solid) and expected (dashed) likelihood scans of Γ_H . Left plot: Results of the SM-like couplings analysis are shown using the data only from 2016 and 2017 (black) or from the combination of Run 1 and Run 2 (red). Right plot: Results of the combined Run 1 and Run 2 data analyses for the SM-like couplings or with three unconstrained anomalous coupling parameters, $f_{a3} \cos(\phi_{a3})$ (red), $f_{a2} \cos(\phi_{a2})$ (blue), and $f_{\Lambda 1} \cos(\phi_{\Lambda 1})$ (violet). The dashed horizontal lines show the 68% and 95% CL regions.

constraints on $\mu_{\text{F}}^{\text{off-shell}}$, $\mu_{\text{V}}^{\text{off-shell}}$ and $\mu^{\text{off-shell}}$ are also derived from the SM-like analysis, but only off-shell events are using during their derivation. They are summarized in Table 4.8, and are shown in Fig. 4.20 together with joint constraints on $\mu_{\text{F}}^{\text{off-shell}}$ and $\mu_{\text{V}}^{\text{off-shell}}$.

Table 4.8: Summary of allowed 68% CL (central values with uncertainties) and 95% CL (in square brackets) intervals on $\mu_{\text{F}}^{\text{off-shell}}$, $\mu_{\text{V}}^{\text{off-shell}}$ and $\mu^{\text{off-shell}}$ obtained from the analysis of the combination of Run 2 2016 and 2017 datasets (on-shell and off-shell), and Run 1 datasets. The constraints are set using only off-shell events.

Parameter	Observed	Expected
$\mu_{\text{F}}^{\text{off-shell}}$	$0.86^{+0.92}_{-0.68}$ [0.0, 2.7]	$1.0^{+1.3}_{-1.0}$ [0.0, 3.5]
$\mu_{\text{V}}^{\text{off-shell}}$	$0.67^{+1.26}_{-0.61}$ [0.0, 3.6]	$1.0^{+3.8}_{-1.0}$ [0.0, 8.4]
$\mu^{\text{off-shell}}$	$0.78^{+0.72}_{-0.53}$ [0.02, 2.28]	$1.00^{+1.20}_{-0.99}$ [0.0, 3.2]

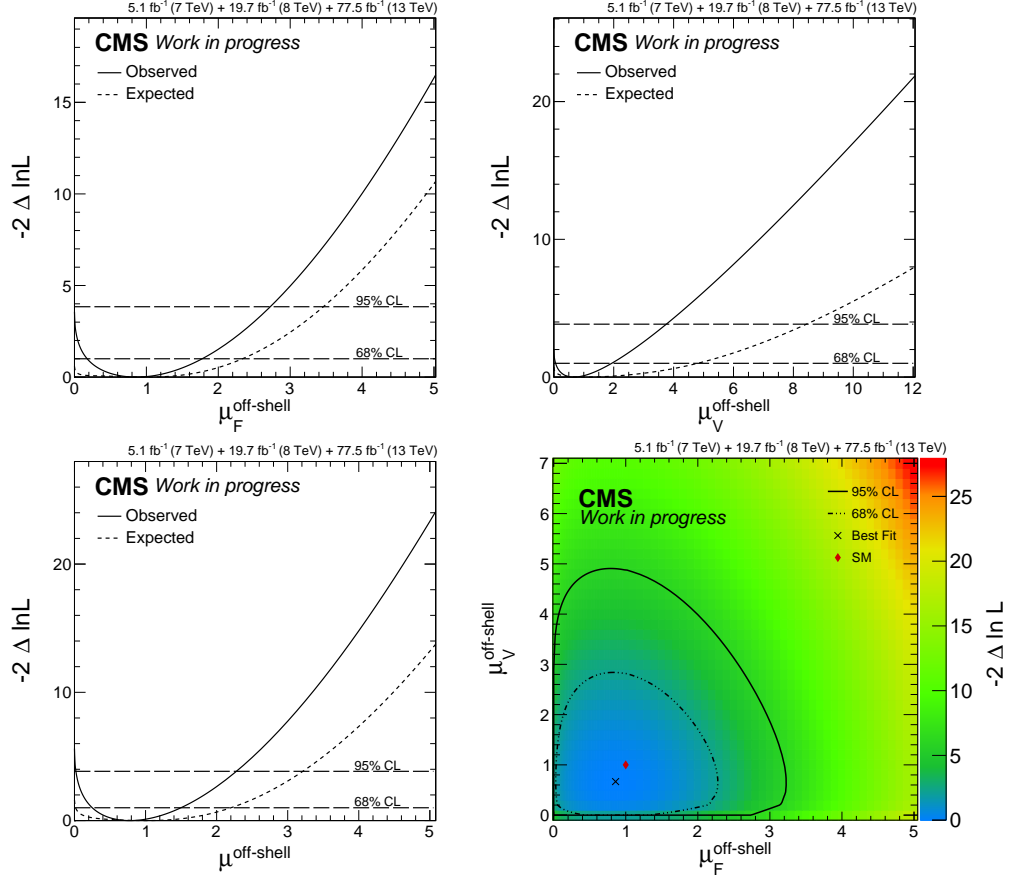


Figure 4.20: Constraints on $\mu_F^{\text{off-shell}}$ (top left), $\mu_V^{\text{off-shell}}$ (top right) and $\mu_F^{\text{off-shell}}$ (bottom left) as well as the observed joint constraints on $\mu_F^{\text{off-shell}}$ and $\mu_V^{\text{off-shell}}$ (bottom right) from off-shell events in the combined Run 1 and Run 2 dataset. In the one-parameter constraints, the dashed horizontal lines show the 68% and 95% CL regions, and observed likelihood scans are shown with solid curves whereas the expected scans are shown with dashed ones. In the two-parameter observed constraint, the two-parameter 68% and 95% CL regions are indicated with the dashed and solid curves, respectively.

4.4 Width and spin-parity projections for the HL-LHC

Using the simulation of the 2016 data at 13 TeV, predictions for the bounds on $f_{a3} \cos(\phi_{a3})$ and Γ_H attainable during the High-Luminosity LHC runs are also derived for an integrated luminosity of 3 ab^{-1} . The predictions are made for two different systematics scenarios. In Scenario 1, the experimental and theoretical systematics are assumed to be the same. In Scenario 2, experimental systematics are assumed to be the same, and theory systematics are halved with respect to their current status. The 10% additional uncertainty applied on the QCD NNLO K factor on the gg background process is kept the same in Scenario 2 in order to remain conservative on the approximate understanding of these corrections on this background component.

The predictions are shown in Fig. 4.21 and summarized in Table 4.9. Systematics are found to have negligible effect on $f_{a3} \cos(\phi_{a3})$ results using either on-shell and off-shell events combined or only on-shell events, so only Scenario 1 is shown. In the case of Γ_H limits, theoretical systematics are dominant over experimental ones. The dominant theoretical systematic effect comes from the uncertainty on the NLO EW correction on the $q\bar{q} \rightarrow 4\ell$ simulation above the $2m_Z$ threshold, but this systematic also appears to be constrained from data if an integrated luminosity of 3 ab^{-1} can be reached. Therefore, Scenario 2 is differentiated from Scenario 1 in Γ_H limits explicitly.

Table 4.9: Summary of 95% CL intervals in square brackets on $f_{a3} \cos(\phi_{a3})$ under the assumption $\Gamma_H = \Gamma_H^{\text{SM}}$, and Γ_H under the assumption $f_{ai} = 0$ for projections when 3 ab^{-1} is attained at HL-LHC runs. Constraints on $f_{a3} \cos(\phi_{a3})$ are multiplied by 10^4 . Scenario 1 is abbreviated as “S1” whereas Scenario 2 is abbreviated as “S2”.

Parameter	Scenario	Projected 95% CL interval
$f_{a3} \cos(\phi_{a3}) \times 10^4$	S1, only on-shell	$[-1.75, 1.75]$
$f_{a3} \cos(\phi_{a3}) \times 10^4$	S1, on-shell and off-shell	$[-1.62, 1.62]$
Γ_H (MeV)	S1	$[2.01, 6.10]$
Γ_H (MeV)	S2	$[2.03, 6.02]$

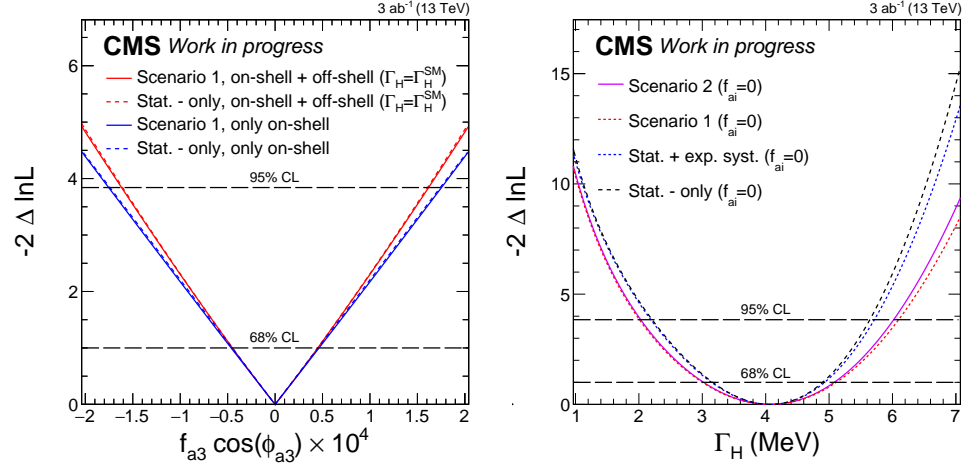


Figure 4.21: Shown are likelihood scans for projections on $f_{a3} \cos(\phi_{a3})$ (left) and Γ_H (right) results at 3 ab^{-1} for HL-LHC runs. On the left plot, the scans are shown using either the combination of on-shell and off-shell events (red) or only on-shell events (blue). The dashed lines represent the effect of removing all systematic uncertainties. On the right plot, Scenario 2 (solid magenta) and Scenario 1 (dotted red) are compared to the cases where either only theory systematics (dotted blue) or all systematics (dashed black) are removed. The Γ_H limits are derived using the parameterization from the SM-like analysis. The dashed horizontal lines shown the 68% and 95% CLs.

4.5 Joint constraints on the mass and width of the Higgs boson

A fully parametric joint mass and width constraint [74] is shown for a potentially wide resonance in Fig. 4.22. Only on-shell events from the Run 2 2016 dataset are used. The $m_{4\ell}^{\text{true}}$ shape of all backgrounds and signals, as well as gluon fusion or electroweak interference contributions are parameterized across on-shell and off-shell using the MCFM simulation for an arbitrary value of m_H or Γ_H . The gluon fusion $m_{4\ell}^{\text{true}}$ shape is further corrected for the NNLO QCD K factors shown in Fig. 3.3. The parameterization for each process is then multiplied with the combined selection efficiency and detector acceptance as well as the categorization efficiency of a simple $\mathcal{D}_{2\text{jet}}^{\text{VBF}} > 0.5$ requirement to enhance VBF production. The resolution on $m_{4\ell}$ is included afterward through numerical convolution. Only the $\mathcal{D}_{\text{bkg}}^{\text{kin}}$ discriminant is used as a second observable to distinguish signal from background. The constraints on m_H are found to be comparable to a dedicated on-shell analysis optimized for the measurement of H boson mass for a narrow resonance.

Similar joint constraints can be placed for the assumption of a narrow Higgs resonance. The dependence of the double-sided Crystal Ball function in Eqn. 4.5 on m_H already allows for the variation of this parameter for different H boson mass values, and no numerical convolution with the $m_{4\ell}^{\text{true}}$ lineshape would be needed in this scenario. In order to place joint constraints on m_H and Γ_H , the on-shell yield expectation also needs to depend on this parameter; otherwise the limits on Γ_H would be biased exactly by the amount of change in the on-shell yield due to the change in the value of m_H . Roughly +10%

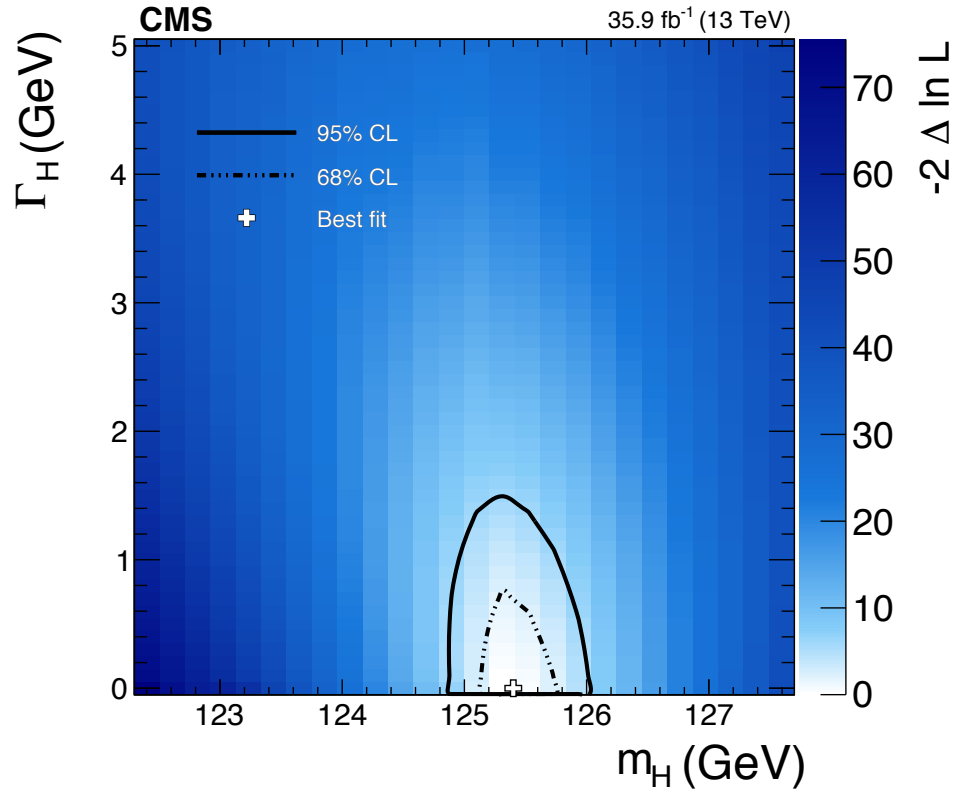


Figure 4.22: Observed likelihood scan of m_H and Γ_H are shown using the on-shell events in the 2016 dataset. The dashed and solid curves show the two-parameter 68% and 95% CLs, respectively [74].

change is expected in the total $H \rightarrow 4\ell$ cross section as the mass shifts by +1 GeV around $m_H = 125$ GeV, and changes on the order of a few percent are also expected in acceptance and efficiency combined.

Two-parameter constraints on m_H and Γ_H under the assumption of the narrow-width resonance are derivable using the combined Run 1 and Run 2 SM-like analysis with on-shell and off-shell events, presented in Section 4.3. The full two-parameter constraints, and constraints on Γ_H given different values of m_H are both shown in Fig. 4.23. These limits are only preliminary because the dependence of the on-shell yield on the value of m_H is not yet included. However, constraints on m_H with the value of Γ_H unconstrained are not affected by this mis-modeling as the signal strengths μ_F and μ_V are unconstrained in the fit. As discussed in Section 4.3.1, the lepton scale and resolution uncertainties are also kept conservative in this study to cover for the scale differences at different lepton p_T and η values, or any mismodeling in lepton resolution. The likelihood scan in m_H of this configuration is shown in Fig. 4.24. The observed (expected) best fit value is $m_H = 125.05 \pm 0.15(\text{stat.})_{-0.13}^{+0.12}(\text{syst.})$ GeV ($m_H = 125.00_{-0.19}^{+0.20}(\text{stat.}) \pm 0.16(\text{syst.})$ GeV), and the observed (expected) 95% CL allowed region is $124.65 < m_H < 125.43$ GeV ($124.50 < m_H < 125.50$ GeV).

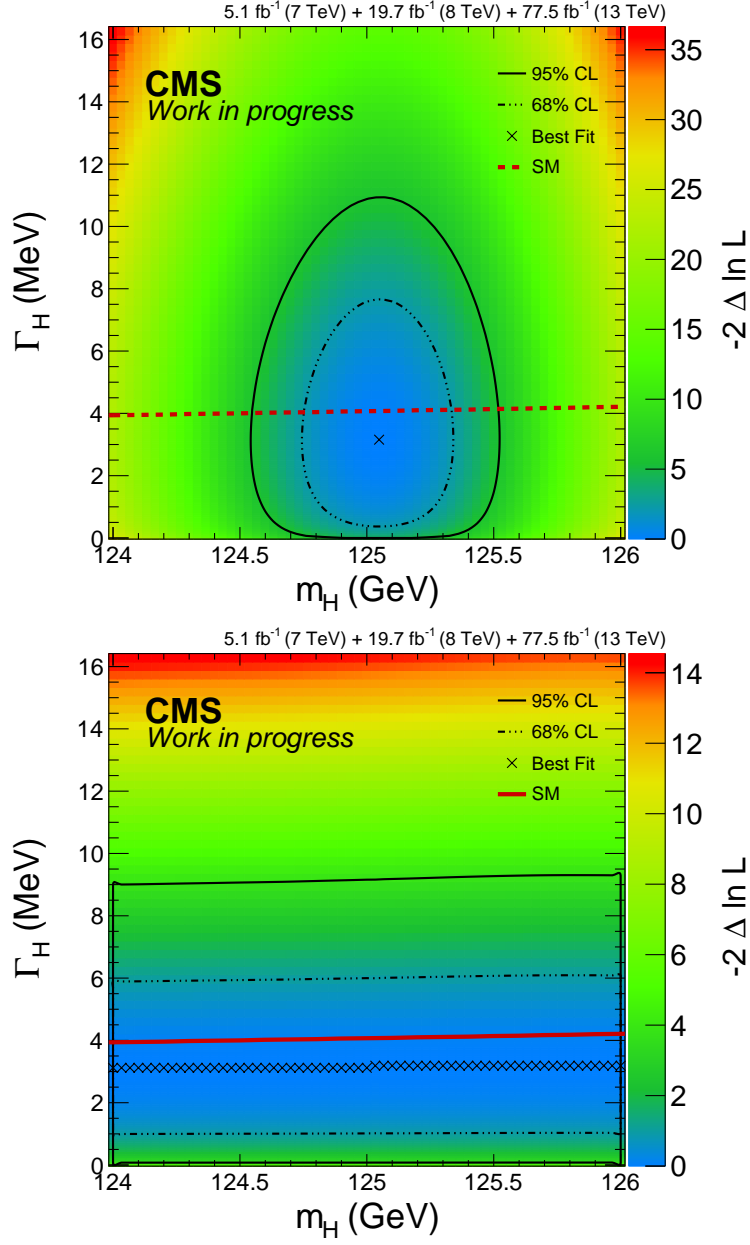


Figure 4.23: Observed likelihood scan of m_H and Γ_H are shown using the on-shell and off-shell events in the combined Run 1 and Run 2 (only 2016 and 2017) dataset. Top plot illustrates the full two-parameter likelihood scan whereas the bottom plot shows constraints only on Γ_H given different values of m_H . The dashed and solid curves show the two-parameter (top) or one-parameter (bottom) 68% and 95% CLs, respectively.

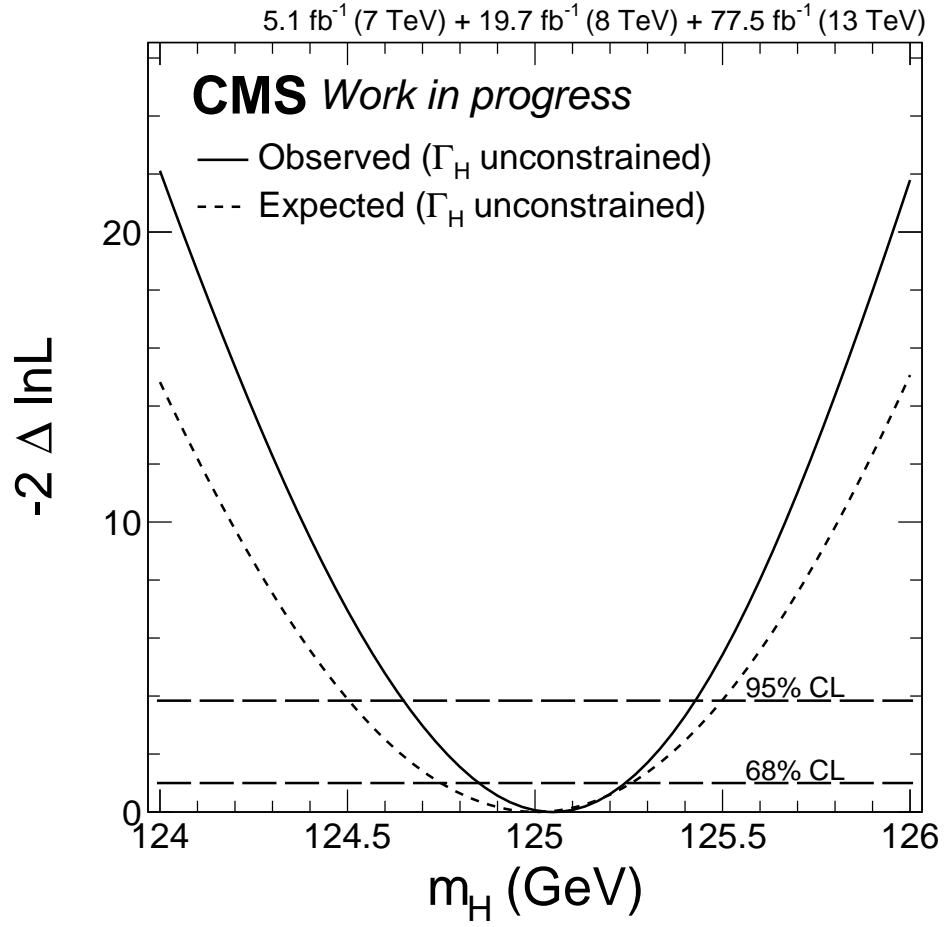


Figure 4.24: Observed (solid) and expected (dashed) likelihood scans of m_H are shown using the on-shell and off-shell events in the combined Run 1 and Run 2 (only 2016 and 2017) dataset. The value of Γ_H is left unconstrained in the scan, so the likelihood is not affected by the dependence of the on-shell yield on the value of m_H . The dashed lines show the 68% and 95% CLs.

Chapter 5

Summary and outlook

Studies of the production and decay of the spin-0 H boson are described. In particular, anomalous HVV couplings are studied in Section 4.1 from on-shell H boson production in 4ℓ and $WW \rightarrow \ell\nu\ell\nu$ decay using the Run 1 data collected by the CMS detector. These constraints and techniques are improved in the Run 2 on-shell analysis of the 4ℓ decay channel. Events from Run 1 are also analyzed in Section 4.2 for the 4ℓ vertex information to make a direct and model-independent measurement of the H boson lifetime, constraining it from above and thereby the H boson total width, Γ_H , from below. The value of Γ_H is constrained further in Section 4.3 by employing the off-shell technique in the 4ℓ decay channel. These constraints are placed using events from both Run 1 and Run 2 datasets. Assumptions on the tensor structure of the spin-0 H boson and the $m_{4\ell}$ lineshape are relaxed by placing joint constraints on Γ_H and different anomalous HVV couplings, unifying the on-shell and off-shell analyses and resulting in tighter anomalous coupling limits with respect to results using only on-shell events. Projections of $f_{a3} \cos(\phi_{a3})$ results, from likelihood parameterizations using only on-shell H boson production

or the combination of on-shell and off-shell regions, and Γ_H results from the combined on-shell and off-shell parameterization in the SM-like width analysis are provided for possible HL-LHC scenarios at 3 ab^{-1} in Section 4.4. The combined on-shell and off-shell parameterization from the SM-like width analysis is used once again in Section 4.5 to place approximate joint constraints on the H boson mass and width, and preliminary constraints on the value of m_H with the value of Γ_H unconstrained in the fit. No significant deviation from the Standard Model is found in the anomalous HVV couplings or in the total width of the H boson, and a preliminary value of m_H from the combined Run 1 and Run 2 dataset is provided.

As presented in Section 3.4, studies of off-shell H boson production appear as a promising tool to study anomalous couplings in gluon fusion production. With more data accumulated and simulation tools better understood, it should be possible to conduct a study of point-like interactions and Yukawa loop couplings with similar off-shell methodology to what is presented in this thesis. It should also be possible to include events from other decay channels, such as on-shell $H \rightarrow \gamma\gamma$, or on-shell and off-shell $H \rightarrow WW$ events, or dedicated kinematic observables for associated particles in order to increase the sensitivity to such couplings.

Consistent performance in the CMS detector over several years is crucial to realize any study on H boson properties. Of particular note is the recent improvements in tracker, presented in Section 2.2.1, where the Phase-1 upgrades to the pixel detector modules and geometry are outlined. Consistent performance is ensured via improvements in its alignment, which is discussed

in Section 2.2.2. The HIP/HipPy and MILLEPEDE II alignment procedures are outlined, and the alignment of sensor curvature, in addition to the standard procedure to align module positions and rotations, and the inclusion of different vertex and mass constraints are discussed. Possible future improvements in tracker alignment could be to account for overlapping modules, introduce constraints to apply on cosmics, improve the application of constraints from dimuon events, and increase the speed of the algorithm in consideration of planned increases in the instantaneous luminosity delivered by the LHC.

Bibliography

- [1] S. L. Glashow. “Partial-Symmetries of Weak Interactions”. In: *Nucl. Phys.* 22 (1961), p. 579. DOI: [10.1016/0029-5582\(61\)90469-2](https://doi.org/10.1016/0029-5582(61)90469-2).
- [2] Steven Weinberg. “A Model of Leptons”. In: *Phys. Rev. Lett.* 19 (1967), p. 1264. DOI: [10.1103/PhysRevLett.19.1264](https://doi.org/10.1103/PhysRevLett.19.1264).
- [3] Abdus Salam. “Weak and electromagnetic interactions”. In: *Elementary particle physics: relativistic groups and analyticity*. Ed. by Nils Svartholm. Proceedings of the eighth Nobel symposium. Almqvist & Wiksell, 1968, p. 367.
- [4] David J. Gross and Frank Wilczek. “Ultraviolet Behavior of Non-Abelian Gauge Theories”. In: *Phys. Rev. Lett.* 30 (1973), p. 1343. DOI: [10.1103/PhysRevLett.30.1343](https://doi.org/10.1103/PhysRevLett.30.1343).
- [5] H. David Politzer. “Reliable Perturbative Results for Strong Interactions?” In: *Phys. Rev. Lett.* 30 (1973), p. 1346. DOI: [10.1103/PhysRevLett.30.1346](https://doi.org/10.1103/PhysRevLett.30.1346).
- [6] P. W. Anderson. “Plasmons, Gauge Invariance, and Mass”. In: *Phys. Rev.* 130 (1 1963), pp. 439–442. DOI: [10.1103/PhysRev.130.439](https://doi.org/10.1103/PhysRev.130.439). URL: <https://link.aps.org/doi/10.1103/PhysRev.130.439>.
- [7] F. Englert and R. Brout. “Broken Symmetry and the Mass of Gauge Vector Mesons”. In: *Phys. Rev. Lett.* 13 (1964), p. 321. DOI: [10.1103/PhysRevLett.13.321](https://doi.org/10.1103/PhysRevLett.13.321).
- [8] Peter W. Higgs. “Broken symmetries, massless particles and gauge fields”. In: *Phys. Lett.* 12 (1964), p. 132. DOI: [10.1016/0031-9163\(64\)91136-9](https://doi.org/10.1016/0031-9163(64)91136-9).
- [9] Peter W. Higgs. “Broken Symmetries and the Masses of Gauge Bosons”. In: *Phys. Rev. Lett.* 13 (1964), p. 508. DOI: [10.1103/PhysRevLett.13.508](https://doi.org/10.1103/PhysRevLett.13.508).

- [10] G. S. Guralnik, C. R. Hagen, and T. W. B. Kibble. “Global Conservation Laws and Massless Particles”. In: *Phys. Rev. Lett.* 13 (1964), p. 585. DOI: [10.1103/PhysRevLett.13.585](https://doi.org/10.1103/PhysRevLett.13.585).
- [11] Peter W. Higgs. “Spontaneous Symmetry Breakdown without Massless Bosons”. In: *Phys. Rev.* 145 (1966), p. 1156. DOI: [10.1103/PhysRev.145.1156](https://doi.org/10.1103/PhysRev.145.1156).
- [12] T. W. B. Kibble. “Symmetry breaking in non-Abelian gauge theories”. In: *Phys. Rev.* 155 (1967), p. 1554. DOI: [10.1103/PhysRev.155.1554](https://doi.org/10.1103/PhysRev.155.1554).
- [13] Y. Nambu and G. Jona-Lasinio. “Dynamical Model of Elementary Particles Based on an Analogy with Superconductivity. I”. In: *Phys. Rev.* 122 (1961), p. 345. DOI: [10.1103/PhysRev.122.345](https://doi.org/10.1103/PhysRev.122.345).
- [14] Murray Gell-Mann and M Levy. “The axial vector current in beta decay”. In: *Nuovo Cim.* 16 (1960), p. 705. DOI: [10.1007/BF02859738](https://doi.org/10.1007/BF02859738).
- [15] M. Goldhaber, L. Grodzins, and A. W. Sunyar. “Helicity of Neutrinos”. In: *Phys. Rev.* 109 (3 1958), pp. 1015–1017. DOI: [10.1103/PhysRev.109.1015](https://doi.org/10.1103/PhysRev.109.1015). URL: <https://link.aps.org/doi/10.1103/PhysRev.109.1015>.
- [16] C. Patrignani and Particle Data Group. “Review of Particle Physics”. In: *Chinese Physics C* 40.10 (2016), p. 100001. URL: <http://stacks.iop.org/1674-1137/40/i=10/a=100001>.
- [17] Nicola Cabibbo. “Unitary Symmetry and Leptonic Decays”. In: *Phys. Rev. Lett.* 10 (12 1963), pp. 531–533. DOI: [10.1103/PhysRevLett.10.531](https://doi.org/10.1103/PhysRevLett.10.531). URL: <https://link.aps.org/doi/10.1103/PhysRevLett.10.531>.
- [18] Makoto Kobayashi and Toshihide Maskawa. “CP Violation in the Renormalizable Theory of Weak Interaction”. In: *Prog. Theor. Phys.* 49 (1973), pp. 652–657. DOI: [10.1143/PTP.49.652](https://doi.org/10.1143/PTP.49.652).
- [19] Ling-Lie Chau and Wai-Yee Keung. “Comments on the Parametrization of the Kobayashi-Maskawa Matrix”. In: *Phys. Rev. Lett.* 53 (19 1984), pp. 1802–1805. DOI: [10.1103/PhysRevLett.53.1802](https://doi.org/10.1103/PhysRevLett.53.1802). URL: <https://link.aps.org/doi/10.1103/PhysRevLett.53.1802>.
- [20] C. A. Baker et al. “Improved Experimental Limit on the Electric Dipole Moment of the Neutron”. In: *Phys. Rev. Lett.* 97 (13 2006), p. 131801. DOI: [10.1103/PhysRevLett.97.131801](https://doi.org/10.1103/PhysRevLett.97.131801). URL: <https://link.aps.org/doi/10.1103/PhysRevLett.97.131801>.

- [21] Yoichiro Nambu. “Quasi-Particles and Gauge Invariance in the Theory of Superconductivity”. In: *Phys. Rev.* 117 (3 1960), pp. 648–663. DOI: [10.1103/PhysRev.117.648](https://doi.org/10.1103/PhysRev.117.648). URL: <https://link.aps.org/doi/10.1103/PhysRev.117.648>.
- [22] J. Goldstone. “Field theories with \hat{A}^n Superconductor \hat{A}^z solutions”. In: *Il Nuovo Cimento (1955-1965)* 19.1 (1961), pp. 154–164. ISSN: 1827-6121. DOI: [10.1007/BF02812722](https://doi.org/10.1007/BF02812722). URL: <https://doi.org/10.1007/BF02812722>.
- [23] Jeffrey Goldstone, Abdus Salam, and Steven Weinberg. “Broken Symmetries”. In: *Phys. Rev.* 127 (3 1962), pp. 965–970. DOI: [10.1103/PhysRev.127.965](https://doi.org/10.1103/PhysRev.127.965). URL: <https://link.aps.org/doi/10.1103/PhysRev.127.965>.
- [24] Georges Aad et al. “Combined Measurement of the Higgs Boson Mass in pp Collisions at $\sqrt{s} = 7$ and 8 TeV with the ATLAS and CMS Experiments”. In: *Phys. Rev. Lett.* 114 (2015), p. 191803. DOI: [10.1103/PhysRevLett.114.191803](https://doi.org/10.1103/PhysRevLett.114.191803). arXiv: [1503.07589](https://arxiv.org/abs/1503.07589) [hep-ex].
- [25] John M. Cornwall, David N. Levin, and George Tiktopoulos. “Uniqueness of spontaneously broken gauge theories”. In: *Phys. Rev. Lett.* 30 (1973). [Erratum: *Phys. Rev. Lett.* 31, 572 (1973)], pp. 1268–1270. DOI: [10.1103/PhysRevLett.31.572](https://doi.org/10.1103/PhysRevLett.31.572), [10.1103/PhysRevLett.30.1268](https://doi.org/10.1103/PhysRevLett.30.1268).
- [26] John M. Cornwall, David N. Levin, and George Tiktopoulos. “Derivation of Gauge Invariance from High-Energy Unitarity Bounds on the s Matrix”. In: *Phys. Rev. D* 10 (1974). Erratum, doi:[10.1103/PhysRevD.11.972](https://doi.org/10.1103/PhysRevD.11.972), p. 1145. DOI: [10.1103/PhysRevD.10.1145](https://doi.org/10.1103/PhysRevD.10.1145).
- [27] J. R. Espinosa and M. Quiros. “Improved metastability bounds on the standard model Higgs mass”. In: *Phys. Lett.* B353 (1995), pp. 257–266. DOI: [10.1016/0370-2693\(95\)00572-3](https://doi.org/10.1016/0370-2693(95)00572-3). arXiv: [hep-ph/9504241](https://arxiv.org/abs/hep-ph/9504241) [hep-ph].
- [28] Gino Isidori, Giovanni Ridolfi, and Alessandro Strumia. “On the metastability of the standard model vacuum”. In: *Nucl. Phys.* B609 (2001), pp. 387–409. DOI: [10.1016/S0550-3213\(01\)00302-9](https://doi.org/10.1016/S0550-3213(01)00302-9). arXiv: [hep-ph/0104016](https://arxiv.org/abs/hep-ph/0104016) [hep-ph].
- [29] B. Pontecorvo. “Mesonium and anti-mesonium”. In: *Sov. Phys. JETP* 6 (1957). [*Zh. Eksp. Teor. Fiz.* 33, 549 (1957)], p. 429.

- [30] Ziro Maki, Masami Nakagawa, and Shoichi Sakata. “Remarks on the unified model of elementary particles”. In: *Prog. Theor. Phys.* 28 (1962). [34(1962)], pp. 870–880. DOI: [10.1143/PTP.28.870](https://doi.org/10.1143/PTP.28.870).
- [31] Q. R. Ahmad et al. “Measurement of the Rate of $\nu_e + d \rightarrow p + p + e^-$ Interactions Produced by ^8B Solar Neutrinos at the Sudbury Neutrino Observatory”. In: *Phys. Rev. Lett.* 87 (7 2001), p. 071301. DOI: [10.1103/PhysRevLett.87.071301](https://doi.org/10.1103/PhysRevLett.87.071301). URL: <https://link.aps.org/doi/10.1103/PhysRevLett.87.071301>.
- [32] Y. Fukuda et al. “Evidence for oscillation of atmospheric neutrinos”. In: *Phys. Rev. Lett.* 81 (1998), pp. 1562–1567. DOI: [10.1103/PhysRevLett.81.1562](https://doi.org/10.1103/PhysRevLett.81.1562). arXiv: [hep-ex/9807003](https://arxiv.org/abs/hep-ex/9807003) [hep-ex].
- [33] Y. Abe et al. “Indication of Reactor $\bar{\nu}_e$ Disappearance in the Double Chooz Experiment”. In: *Phys. Rev. Lett.* 108 (2012), p. 131801. DOI: [10.1103/PhysRevLett.108.131801](https://doi.org/10.1103/PhysRevLett.108.131801). arXiv: [1112.6353](https://arxiv.org/abs/1112.6353) [hep-ex].
- [34] F. P. An et al. “Observation of electron-antineutrino disappearance at Daya Bay”. In: *Phys. Rev. Lett.* 108 (2012), p. 171803. DOI: [10.1103/PhysRevLett.108.171803](https://doi.org/10.1103/PhysRevLett.108.171803). arXiv: [1203.1669](https://arxiv.org/abs/1203.1669) [hep-ex].
- [35] J. K. Ahn et al. “Observation of Reactor Electron Antineutrino Disappearance in the RENO Experiment”. In: *Phys. Rev. Lett.* 108 (2012), p. 191802. DOI: [10.1103/PhysRevLett.108.191802](https://doi.org/10.1103/PhysRevLett.108.191802). arXiv: [1204.0626](https://arxiv.org/abs/1204.0626) [hep-ex].
- [36] N. Agafonova et al. “Observation of a first ν_τ candidate in the OPERA experiment in the CNGS beam”. In: *Phys. Lett.* B691 (2010), pp. 138–145. DOI: [10.1016/j.physletb.2010.06.022](https://doi.org/10.1016/j.physletb.2010.06.022). arXiv: [1006.1623](https://arxiv.org/abs/1006.1623) [hep-ex].
- [37] K. Abe et al. “Evidence of Electron Neutrino Appearance in a Muon Neutrino Beam”. In: *Phys. Rev.* D88.3 (2013), p. 032002. DOI: [10.1103/PhysRevD.88.032002](https://doi.org/10.1103/PhysRevD.88.032002). arXiv: [1304.0841](https://arxiv.org/abs/1304.0841) [hep-ex].
- [38] *LHC machine outreach: LHC images*. Accessed: 2018-06-30. URL: https://lhc-machine-outreach.web.cern.ch/lhc-machine-outreach/lhc_in_pictures.htm.
- [39] CMS Collaboration. *Technical proposal for the Phase-II upgrade of the Compact Muon Solenoid*. CMS Technical proposal CERN-LHCC-2015-010, CMS-TDR-15-02. CERN, 2015. URL: <http://cds.cern.ch/record/2020886>.
- [40] S. Chatrchyan et al. “The CMS experiment at the CERN LHC”. In: *JINST* 3 (2008), S08004. DOI: [10.1088/1748-0221/3/08/S08004](https://doi.org/10.1088/1748-0221/3/08/S08004).

- [41] V. Karimäki. “The CMS tracker system project”. In: (1997). Ed. by M. Mannelli et al.
- [42] CERN. Geneva. LHC Experiments Committee. “The CMS tracker”. In: (2000).
- [43] David Aaron Matzner Dominguez et al. “CMS Technical Design Report for the Pixel Detector Upgrade”. In: (2012). DOI: [10.2172/1151650](https://doi.org/10.2172/1151650).
- [44] Laura Borrello et al. *Sensor Design for the CMS Silicon Strip Tracker*. Tech. rep. CMS-NOTE-2003-020. Geneva: CERN, 2003. URL: <http://cds.cern.ch/record/687861>.
- [45] J. L. Agram et al. “The silicon sensors for the Compact Muon Solenoid tracker: Design and qualification procedure”. In: *Nucl. Instrum. Meth.* A517 (2004), pp. 77–93. DOI: [10.1016/j.nima.2003.08.175](https://doi.org/10.1016/j.nima.2003.08.175).
- [46] “CMS Tracker Alignment Performance Results Start-Up 2017”. In: (2017). URL: <http://cds.cern.ch/record/2297528>.
- [47] Volker Blobel and Claus Kleinwort. “A New method for the high precision alignment of track detectors”. In: *Advanced Statistical Techniques in Particle Physics. Proceedings, Conference, Durham, UK, March 18-22, 2002*. 2002, URL-STR(9). arXiv: [hep-ex/0208021](https://arxiv.org/abs/hep-ex/0208021) [hep-ex]. URL: <http://www.ippp.dur.ac.uk/Workshops/02/statistics/proceedings/blobel1.pdf>.
- [48] V. Blobel. “Software alignment for tracking detectors”. In: *Nucl. Instrum. Meth.* A566 (2006), pp. 5–13. DOI: [10.1016/j.nima.2006.05.157](https://doi.org/10.1016/j.nima.2006.05.157).
- [49] Serguei Chatrchyan et al. “Alignment of the CMS tracker with LHC and cosmic ray data”. In: *JINST* 9 (2014), P06009. DOI: [10.1088/1748-0221/9/06/P06009](https://doi.org/10.1088/1748-0221/9/06/P06009). arXiv: [1403.2286](https://arxiv.org/abs/1403.2286) [physics.ins-det].
- [50] V. Karimaki et al. “Sensor alignment by tracks”. In: *eConf* C0303241 (2003), TULT008. arXiv: [physics/0306034](https://arxiv.org/abs/physics/0306034) [physics].
- [51] “CMS Tracker Alignment Performance Results 2016”. In: (2017). URL: <https://cds.cern.ch/record/2273267>.
- [52] S Chatrchyan et al. “Alignment of the CMS Silicon Tracker during Commissioning with Cosmic Rays”. In: *JINST* 5 (2010), T03009. DOI: [10.1088/1748-0221/5/03/T03009](https://doi.org/10.1088/1748-0221/5/03/T03009). arXiv: [0910.2505](https://arxiv.org/abs/0910.2505) [physics.ins-det].
- [53] Matteo Cacciari, Gavin P. Salam, and Gregory Soyez. “The anti- k_t jet clustering algorithm”. In: *JHEP* 04 (2008), p. 063. DOI: [10.1088/1126-6708/2008/04/063](https://doi.org/10.1088/1126-6708/2008/04/063). arXiv: [0802.1189](https://arxiv.org/abs/0802.1189) [hep-ex].

- [54] Matteo Cacciari, Gavin P. Salam, and Gregory Soyez. “FastJet user manual”. In: *Eur. Phys. J. C* 72 (2012), p. 1896. DOI: [10.1140/epjc/s10052-012-1896-2](https://doi.org/10.1140/epjc/s10052-012-1896-2). arXiv: 1111.6097 [hep-ph].
- [55] “Tracker Alignment Performance Plots after Commissioning”. In: (2017). URL: <https://cds.cern.ch/record/2297526>.
- [56] M. Anfreville et al. “Laser monitoring system for the CMS lead tungstate crystal calorimeter”. In: *Nucl. Instrum. Meth. A* 594 (2008), pp. 292–320. DOI: [10.1016/j.nima.2008.01.104](https://doi.org/10.1016/j.nima.2008.01.104).
- [57] Serguei Chatrchyan et al. “Energy Calibration and Resolution of the CMS Electromagnetic Calorimeter in pp Collisions at $\sqrt{s} = 7$ TeV”. In: *JINST* 8 (2013). [JINST8,9009(2013)], P09009. DOI: [10.1088/1748-0221/8/09/P09009](https://doi.org/10.1088/1748-0221/8/09/P09009). arXiv: 1306.2016 [hep-ex].
- [58] “ECAL Laser monitoring till end of 2016 and ECAL phi-symmetry”. In: (2017). URL: <https://cds.cern.ch/record/2252725>.
- [59] J. Mans et al. “CMS Technical Design Report for the Phase 1 Upgrade of the Hadron Calorimeter”. In: (2012). DOI: [10.2172/1151651](https://doi.org/10.2172/1151651).
- [60] Vardan Khachatryan et al. “The CMS trigger system”. In: *JINST* 12 (2017), P01020. DOI: [10.1088/1748-0221/12/01/P01020](https://doi.org/10.1088/1748-0221/12/01/P01020). arXiv: 1609.02366 [physics.ins-det].
- [61] P. Sphicas. “CMS: The TriDAS project. Technical design report, Vol. 2: Data acquisition and high-level trigger”. In: (2002).
- [62] A. M. Sirunyan et al. “Particle-flow reconstruction and global event description with the CMS detector”. In: *JINST* 12 (2017), P10003. DOI: [10.1088/1748-0221/12/10/P10003](https://doi.org/10.1088/1748-0221/12/10/P10003). arXiv: 1706.04965 [physics.ins-det].
- [63] CMS Collaboration. *Commissioning of the particle-flow event reconstruction with the first LHC collisions recorded in the CMS detector*. CMS Physics Analysis Summary CMS-PAS-PFT-10-001. 2010. URL: <http://cdsweb.cern.ch/record/1247373>.
- [64] CMS Collaboration. *Particle-flow event reconstruction in CMS and performance for jets, taus, and E_T^{miss}* . CMS Physics Analysis Summary CMS-PAS-PFT-09-001. 2009. URL: <http://cdsweb.cern.ch/record/1194487>.
- [65] W. Adam et al. “Track reconstruction in the CMS tracker”. In: (2005).

- [66] Serguei Chatrchyan et al. “Description and performance of track and primary-vertex reconstruction with the CMS tracker”. In: *JINST* 9 (2014), P10009. DOI: [10.1088/1748-0221/9/10/P10009](https://doi.org/10.1088/1748-0221/9/10/P10009). arXiv: [1405.6569](https://arxiv.org/abs/1405.6569) [physics.ins-det].
- [67] Pierre Billoir. “Progressive track recognition with a Kalman like fitting procedure”. In: *Comput. Phys. Commun.* 57 (1989), pp. 390–394. DOI: [10.1016/0010-4655\(89\)90249-X](https://doi.org/10.1016/0010-4655(89)90249-X).
- [68] Pierre Billoir and S. Qian. “Simultaneous pattern recognition and track fitting by the Kalman filtering method”. In: *Nucl. Instrum. Meth.* A294 (1990), pp. 219–228. DOI: [10.1016/0168-9002\(90\)91835-Y](https://doi.org/10.1016/0168-9002(90)91835-Y).
- [69] R. Mankel. “A Concurrent track evolution algorithm for pattern recognition in the HERA-B main tracking system”. In: *Nucl. Instrum. Meth.* A395 (1997), pp. 169–184. DOI: [10.1016/S0168-9002\(97\)00705-5](https://doi.org/10.1016/S0168-9002(97)00705-5).
- [70] R. Frühwirth. “Application of Kalman filtering to track and vertex fitting”. In: *Nucl. Instrum. Meth.* A262 (1987), pp. 444–450. DOI: [10.1016/0168-9002\(87\)90887-4](https://doi.org/10.1016/0168-9002(87)90887-4).
- [71] Wolfgang Adam et al. “Reconstruction of Electrons with the Gaussian-Sum Filter in the CMS Tracker at the LHC”. In: (2005).
- [72] Serguei Chatrchyan et al. “Measurement of the properties of a Higgs boson in the four-lepton final state”. In: *Phys. Rev.* D89.9 (2014), p. 092007. DOI: [10.1103/PhysRevD.89.092007](https://doi.org/10.1103/PhysRevD.89.092007). arXiv: [1312.5353](https://arxiv.org/abs/1312.5353) [hep-ex].
- [73] *Measurements of properties of the Higgs boson and search for an additional resonance in the four-lepton final state at $\sqrt{s} = 13$ TeV*. Tech. rep. CMS-PAS-HIG-16-033. Geneva: CERN, 2016. URL: <https://cds.cern.ch/record/2204926>.
- [74] Albert M Sirunyan et al. “Measurements of properties of the Higgs boson decaying into the four-lepton final state in pp collisions at $\sqrt{s} = 13$ TeV”. In: *JHEP* 11 (2017), p. 047. DOI: [10.1007/JHEP11\(2017\)047](https://doi.org/10.1007/JHEP11(2017)047). arXiv: [1706.09936](https://arxiv.org/abs/1706.09936) [hep-ex].
- [75] *Measurements of properties of the Higgs boson in the four-lepton final state at $\sqrt{s} = 13$ TeV*. Tech. rep. CMS-PAS-HIG-18-001. Geneva: CERN, 2018. URL: <https://cds.cern.ch/record/2621419>.
- [76] Serguei Chatrchyan et al. “Determination of Jet Energy Calibration and Transverse Momentum Resolution in CMS”. In: *JINST* 6 (2011), P11002. DOI: [10.1088/1748-0221/6/11/P11002](https://doi.org/10.1088/1748-0221/6/11/P11002). arXiv: [1107.4277](https://arxiv.org/abs/1107.4277) [physics.ins-det].

- [77] Vardan Khachatryan et al. “Jet energy scale and resolution in the CMS experiment in pp collisions at 8 TeV”. In: *JINST* 12 (2017), P02014. DOI: [10.1088/1748-0221/12/02/P02014](https://doi.org/10.1088/1748-0221/12/02/P02014). arXiv: [1607.03663](https://arxiv.org/abs/1607.03663) [hep-ex].
- [78] Serguei Chatrchyan et al. “Identification of b-quark jets with the CMS experiment”. In: *JINST* 8 (2013), P04013. DOI: [10.1088/1748-0221/8/04/P04013](https://doi.org/10.1088/1748-0221/8/04/P04013). arXiv: [1211.4462](https://arxiv.org/abs/1211.4462) [hep-ex].
- [79] CMS Collaboration. *Identification of b quark jets at the CMS Experiment in the LHC Run 2*. CMS Physics Analysis Summary CMS-PAS-BTV-15-001. 2016. URL: <https://cds.cern.ch/record/2138504>.
- [80] Albert M Sirunyan et al. “Identification of heavy-flavour jets with the CMS detector in pp collisions at 13 TeV”. In: *JINST* 13 (2018), P05011. DOI: [10.1088/1748-0221/13/05/P05011](https://doi.org/10.1088/1748-0221/13/05/P05011). arXiv: [1712.07158](https://arxiv.org/abs/1712.07158) [physics.ins-det].
- [81] Georges Aad et al. “Observation of a new particle in the search for the Standard Model Higgs boson with the ATLAS detector at the LHC”. In: *Phys. Lett. B* 716 (2012), p. 1. DOI: [10.1016/j.physletb.2012.08.020](https://doi.org/10.1016/j.physletb.2012.08.020). arXiv: [1207.7214](https://arxiv.org/abs/1207.7214) [hep-ex].
- [82] Serguei Chatrchyan et al. “Observation of a new boson at a mass of 125 GeV with the CMS experiment at the LHC”. In: *Phys. Lett. B* 716 (2012), pp. 30–61. DOI: [10.1016/j.physletb.2012.08.021](https://doi.org/10.1016/j.physletb.2012.08.021). arXiv: [1207.7235](https://arxiv.org/abs/1207.7235) [hep-ex].
- [83] Serguei Chatrchyan et al. “Observation of a new boson with mass near 125 GeV in pp collisions at $\sqrt{s} = 7$ and 8 TeV”. In: *JHEP* 06 (2013), p. 081. DOI: [10.1007/JHEP06\(2013\)081](https://doi.org/10.1007/JHEP06(2013)081). arXiv: [1303.4571](https://arxiv.org/abs/1303.4571) [hep-ex].
- [84] Georges Aad et al. “Measurement of Higgs boson production in the diphoton decay channel in pp collisions at center-of-mass energies of 7 and 8 TeV with the ATLAS detector”. In: *Phys. Rev. D* 90.11 (2014), p. 112015. DOI: [10.1103/PhysRevD.90.112015](https://doi.org/10.1103/PhysRevD.90.112015). arXiv: [1408.7084](https://arxiv.org/abs/1408.7084) [hep-ex].
- [85] Vardan Khachatryan et al. “Observation of the diphoton decay of the Higgs boson and measurement of its properties”. In: *Eur. Phys. J. C* 74.10 (2014), p. 3076. DOI: [10.1140/epjc/s10052-014-3076-z](https://doi.org/10.1140/epjc/s10052-014-3076-z). arXiv: [1407.0558](https://arxiv.org/abs/1407.0558) [hep-ex].
- [86] L. D. Landau. “On the angular momentum of a system of two photons”. In: *Dokl. Akad. Nauk Ser. Fiz.* 60.2 (1948), pp. 207–209. DOI: [10.1016/B978-0-08-010586-4.50070-5](https://doi.org/10.1016/B978-0-08-010586-4.50070-5).

- [87] Chen-Ning Yang. “Selection Rules for the Dematerialization of a Particle Into Two Photons”. In: *Phys. Rev.* 77 (1950), pp. 242–245. DOI: [10.1103/PhysRev.77.242](https://doi.org/10.1103/PhysRev.77.242).
- [88] Serguei Chatrchyan et al. “Study of the Mass and Spin-Parity of the Higgs Boson Candidate Via Its Decays to Z Boson Pairs”. In: *Phys. Rev. Lett.* 110.8 (2013), p. 081803. DOI: [10.1103/PhysRevLett.110.081803](https://doi.org/10.1103/PhysRevLett.110.081803). arXiv: [1212.6639](https://arxiv.org/abs/1212.6639) [hep-ex].
- [89] Serguei Chatrchyan et al. “Measurement of Higgs boson production and properties in the WW decay channel with leptonic final states”. In: *JHEP* 01 (2014), p. 096. DOI: [10.1007/JHEP01\(2014\)096](https://doi.org/10.1007/JHEP01(2014)096). arXiv: [1312.1129](https://arxiv.org/abs/1312.1129) [hep-ex].
- [90] Georges Aad et al. “Measurements of Higgs boson production and couplings in diboson final states with the ATLAS detector at the LHC”. In: *Phys. Lett.* B726 (2013). [Erratum: *Phys. Lett.* B734,406(2014)], pp. 88–119. DOI: [10.1016/j.physletb.2014.05.011](https://doi.org/10.1016/j.physletb.2014.05.011), [10.1016/j.physletb.2013.08.010](https://doi.org/10.1016/j.physletb.2013.08.010). arXiv: [1307.1427](https://arxiv.org/abs/1307.1427) [hep-ex].
- [91] Georges Aad et al. “Evidence for the spin-0 nature of the Higgs boson using ATLAS data”. In: *Phys. Lett.* B726 (2013), pp. 120–144. DOI: [10.1016/j.physletb.2013.08.026](https://doi.org/10.1016/j.physletb.2013.08.026). arXiv: [1307.1432](https://arxiv.org/abs/1307.1432) [hep-ex].
- [92] Nikolas Kauer and Giampiero Passarino. “Inadequacy of zero-width approximation for a light Higgs boson signal”. In: *JHEP* 08 (2012), p. 116. DOI: [10.1007/JHEP08\(2012\)116](https://doi.org/10.1007/JHEP08(2012)116). arXiv: [1206.4803](https://arxiv.org/abs/1206.4803) [hep-ph].
- [93] Nikolas Kauer. “Inadequacy of zero-width approximation for a light Higgs boson signal”. In: *Mod. Phys. Lett.* A28 (2013), p. 1330015. DOI: [10.1142/S0217732313300152](https://doi.org/10.1142/S0217732313300152). arXiv: [1305.2092](https://arxiv.org/abs/1305.2092) [hep-ph].
- [94] John M. Campbell, R. Keith Ellis, and Ciaran Williams. “Bounding the Higgs width at the LHC using full analytic results for $gg \rightarrow e^-e^+\mu^-\mu^+$ ”. In: *JHEP* 04 (2014), p. 060. DOI: [10.1007/JHEP04\(2014\)060](https://doi.org/10.1007/JHEP04(2014)060). arXiv: [1311.3589](https://arxiv.org/abs/1311.3589) [hep-ph].
- [95] Fabrizio Caola and Kirill Melnikov. “Constraining the Higgs boson width with ZZ production at the LHC”. In: *Phys. Rev.* D88 (2013), p. 054024. DOI: [10.1103/PhysRevD.88.054024](https://doi.org/10.1103/PhysRevD.88.054024). arXiv: [1307.4935](https://arxiv.org/abs/1307.4935) [hep-ph].
- [96] Giampiero Passarino. “Higgs CAT”. In: *Eur. Phys. J.* C74 (2014), p. 2866. DOI: [10.1140/epjc/s10052-014-2866-7](https://doi.org/10.1140/epjc/s10052-014-2866-7). arXiv: [1312.2397](https://arxiv.org/abs/1312.2397) [hep-ph].

- [97] James S. Gainer et al. “Beyond Geolocating: Constraining Higher Dimensional Operators in $H \rightarrow 4\ell$ with Off-Shell Production and More”. In: *Phys. Rev. D* 91.3 (2015), p. 035011. DOI: [10.1103/PhysRevD.91.035011](https://doi.org/10.1103/PhysRevD.91.035011). arXiv: [1403.4951](https://arxiv.org/abs/1403.4951) [hep-ph].
- [98] Vardan Khachatryan et al. “Limits on the Higgs boson lifetime and width from its decay to four charged leptons”. In: *Phys. Rev. D* 92.7 (2015), p. 072010. DOI: [10.1103/PhysRevD.92.072010](https://doi.org/10.1103/PhysRevD.92.072010). arXiv: [1507.06656](https://arxiv.org/abs/1507.06656) [hep-ex].
- [99] D. de Florian et al. “Handbook of LHC Higgs Cross Sections: 4. Deciphering the Nature of the Higgs Sector”. In: (2016). DOI: [10.23731/CYRM-2017-002](https://doi.org/10.23731/CYRM-2017-002). arXiv: [1610.07922](https://arxiv.org/abs/1610.07922) [hep-ph].
- [100] Yanyan Gao et al. “Spin determination of single-produced resonances at hadron colliders”. In: *Phys. Rev. D* 81 (2010), p. 075022. DOI: [10.1103/PhysRevD.81.075022](https://doi.org/10.1103/PhysRevD.81.075022). arXiv: [1001.3396](https://arxiv.org/abs/1001.3396) [hep-ph].
- [101] Sara Bolognesi et al. “On the spin and parity of a single-produced resonance at the LHC”. In: *Phys. Rev. D* 86 (2012), p. 095031. DOI: [10.1103/PhysRevD.86.095031](https://doi.org/10.1103/PhysRevD.86.095031). arXiv: [1208.4018](https://arxiv.org/abs/1208.4018) [hep-ph].
- [102] Ian Anderson et al. “Constraining anomalous HVV interactions at proton and lepton colliders”. In: *Phys. Rev. D* 89.3 (2014), p. 035007. DOI: [10.1103/PhysRevD.89.035007](https://doi.org/10.1103/PhysRevD.89.035007). arXiv: [1309.4819](https://arxiv.org/abs/1309.4819) [hep-ph].
- [103] Andrei V. Gritsan et al. “Constraining anomalous Higgs boson couplings to the heavy flavor fermions using matrix element techniques”. In: *Phys. Rev. D* 94.5 (2016), p. 055023. DOI: [10.1103/PhysRevD.94.055023](https://doi.org/10.1103/PhysRevD.94.055023). arXiv: [1606.03107](https://arxiv.org/abs/1606.03107) [hep-ph].
- [104] J R Andersen et al. “Handbook of LHC Higgs Cross Sections: 3. Higgs Properties”. In: (2013). Ed. by S Heinemeyer et al. DOI: [10.5170/CERN-2013-004](https://doi.org/10.5170/CERN-2013-004). arXiv: [1307.1347](https://arxiv.org/abs/1307.1347) [hep-ph].
- [105] Stefano Catani and Massimiliano Grazzini. “An NNLO subtraction formalism in hadron collisions and its application to Higgs boson production at the LHC”. In: *Phys. Rev. Lett.* 98 (2007), p. 222002. DOI: [10.1103/PhysRevLett.98.222002](https://doi.org/10.1103/PhysRevLett.98.222002). arXiv: [hep-ph/0703012](https://arxiv.org/abs/hep-ph/0703012) [hep-ph].
- [106] Massimiliano Grazzini. “NNLO predictions for the Higgs boson signal in the $H \rightarrow WW \rightarrow l\nu l\nu$ and $H \rightarrow ZZ \rightarrow 4l$ decay channels”. In: *JHEP* 02 (2008), p. 043. DOI: [10.1088/1126-6708/2008/02/043](https://doi.org/10.1088/1126-6708/2008/02/043). arXiv: [0801.3232](https://arxiv.org/abs/0801.3232) [hep-ph].

- [107] Massimiliano Grazzini and Hayk Sargsyan. “Heavy-quark mass effects in Higgs boson production at the LHC”. In: *JHEP* 09 (2013), p. 129. DOI: [10.1007/JHEP09\(2013\)129](https://doi.org/10.1007/JHEP09(2013)129). arXiv: [1306.4581](https://arxiv.org/abs/1306.4581) [hep-ph].
- [108] E. Bagnaschi et al. “Higgs production via gluon fusion in the POWHEG approach in the SM and in the MSSM”. In: *JHEP* 02 (2012), p. 088. DOI: [10.1007/JHEP02\(2012\)088](https://doi.org/10.1007/JHEP02(2012)088). arXiv: [1111.2854](https://arxiv.org/abs/1111.2854) [hep-ph].
- [109] Paolo Nason and Carlo Oleari. “NLO Higgs boson production via vector-boson fusion matched with shower in POWHEG”. In: *JHEP* 02 (2010), p. 037. DOI: [10.1007/JHEP02\(2010\)037](https://doi.org/10.1007/JHEP02(2010)037). arXiv: [0911.5299](https://arxiv.org/abs/0911.5299) [hep-ph].
- [110] S. Alioli et al. “NLO vector-boson production matched with shower in POWHEG”. In: *JHEP* 07 (2008), p. 060. DOI: [10.1088/1126-6708/2008/07/060](https://doi.org/10.1088/1126-6708/2008/07/060). arXiv: [0805.4802](https://arxiv.org/abs/0805.4802) [hep-ph].
- [111] Paolo Nason. “A new method for combining NLO QCD with shower Monte Carlo algorithms”. In: *JHEP* 11 (2004), p. 040. DOI: [10.1088/1126-6708/2004/11/040](https://doi.org/10.1088/1126-6708/2004/11/040). arXiv: [hep-ph/0409146](https://arxiv.org/abs/hep-ph/0409146).
- [112] Stefano Frixione, Paolo Nason, and Carlo Oleari. “Matching NLO QCD computations with Parton Shower simulations: the POWHEG method”. In: *JHEP* 11 (2007), p. 070. DOI: [10.1088/1126-6708/2007/11/070](https://doi.org/10.1088/1126-6708/2007/11/070). arXiv: [0709.2092](https://arxiv.org/abs/0709.2092) [hep-ph].
- [113] G. Bozzia et al. “The $q(T)$ spectrum of the Higgs boson at the LHC in QCD perturbation theory”. In: *Phys. Lett. B* 564 (2003), p. 65. DOI: [10.1016/S0370-2693\(03\)00656-7](https://doi.org/10.1016/S0370-2693(03)00656-7). arXiv: [hep-ph/0302104](https://arxiv.org/abs/hep-ph/0302104) [hep-ph].
- [114] Giuseppe Bozzi et al. “Transverse-momentum resummation and the spectrum of the Higgs boson at the LHC”. In: *Nucl. Phys. B* 737 (2006), p. 73. DOI: [10.1016/j.nuclphysb.2005.12.022](https://doi.org/10.1016/j.nuclphysb.2005.12.022). arXiv: [hep-ph/0508068](https://arxiv.org/abs/hep-ph/0508068) [hep-ph].
- [115] Daniel de Florian et al. “Transverse-momentum resummation: Higgs boson production at the Tevatron and the LHC”. In: *JHEP* 11 (2011), p. 064. DOI: [10.1007/JHEP11\(2011\)064](https://doi.org/10.1007/JHEP11(2011)064). arXiv: [1109.2109](https://arxiv.org/abs/1109.2109) [hep-ph].
- [116] D. de Florian et al. “Higgs boson production at the LHC: transverse momentum resummation effects in the $H \rightarrow \gamma\gamma$, $H \rightarrow WW \rightarrow \ell\nu\ell\nu$ and $H \rightarrow ZZ \rightarrow 4\ell$ decay modes”. In: *JHEP* 06 (2012), p. 132. DOI: [10.1007/JHEP06\(2012\)132](https://doi.org/10.1007/JHEP06(2012)132). arXiv: [1203.6321](https://arxiv.org/abs/1203.6321) [hep-ph].

- [117] Gionata Luisoni et al. “ $HW^\pm/HZ + 0$ and 1 jet at NLO with the POWHEG BOX interfaced to GoSam and their merging within MiNLO”. In: *JHEP* 10 (2013), p. 083. DOI: [10.1007/JHEP10\(2013\)083](https://doi.org/10.1007/JHEP10(2013)083). arXiv: [1306.2542](https://arxiv.org/abs/1306.2542) [hep-ph].
- [118] John M. Campbell and R. K. Ellis. “MCFM for the Tevatron and the LHC”. In: *Nucl. Phys. Proc. Suppl.* 205-206 (2010), pp. 10–15. DOI: [10.1016/j.nuclphysbps.2010.08.011](https://doi.org/10.1016/j.nuclphysbps.2010.08.011). arXiv: [1007.3492](https://arxiv.org/abs/1007.3492) [hep-ph].
- [119] John M. Campbell, R. Keith Ellis, and Ciaran Williams. “Vector boson pair production at the LHC”. In: *JHEP* 07 (2011), p. 018. DOI: [10.1007/JHEP07\(2011\)018](https://doi.org/10.1007/JHEP07(2011)018). arXiv: [1105.0020](https://arxiv.org/abs/1105.0020) [hep-ph].
- [120] Alessandro Ballestrero et al. “PHANTOM: a Monte Carlo event generator for six parton final states at high energy colliders”. In: *Comput. Phys. Commun.* 180 (2009), p. 401. DOI: [10.1016/j.cpc.2008.10.005](https://doi.org/10.1016/j.cpc.2008.10.005). arXiv: [0801.3359](https://arxiv.org/abs/0801.3359) [hep-ph].
- [121] Tom Melia et al. “ W^+W^- , WZ and ZZ production in the POWHEG BOX”. In: *JHEP* 11 (2011), p. 078. DOI: [10.1007/JHEP11\(2011\)078](https://doi.org/10.1007/JHEP11(2011)078). arXiv: [1107.5051](https://arxiv.org/abs/1107.5051) [hep-ph].
- [122] Paolo Nason and Giulia Zanderighi. “ W^+W^- , WZ and ZZ production in the POWHEG-BOX-V2”. In: *Eur. Phys. J. C* 74.1 (2014), p. 2702. DOI: [10.1140/epjc/s10052-013-2702-5](https://doi.org/10.1140/epjc/s10052-013-2702-5). arXiv: [1311.1365](https://arxiv.org/abs/1311.1365) [hep-ph].
- [123] Massimiliano Grazzini, Stefan Kallweit, and Dirk Rathlev. “ZZ production at the LHC: fiducial cross sections and distributions in NNLO QCD”. In: *Phys. Lett. B* 750 (2015), pp. 407–410. DOI: [10.1016/j.physletb.2015.09.055](https://doi.org/10.1016/j.physletb.2015.09.055). arXiv: [1507.06257](https://arxiv.org/abs/1507.06257) [hep-ph].
- [124] Julien Baglio, Le Duc Ninh, and Marcus M. Weber. “Massive gauge boson pair production at the LHC: a next-to-leading order story”. In: *Phys. Rev. D* 88 (2013). [Erratum: doi:[10.1103/PhysRevD.94.099902](https://doi.org/10.1103/PhysRevD.94.099902)], p. 113005. DOI: [10.1103/PhysRevD.88.113005](https://doi.org/10.1103/PhysRevD.88.113005). arXiv: [1307.4331](https://arxiv.org/abs/1307.4331) [hep-ph].
- [125] Stefan Gieseke, Tobias Kasprzik, and Johann H. K  ijhn. “Vector-boson pair production and electroweak corrections in HERWIG++”. In: *Eur. Phys. J. C* 74.8 (2014), p. 2988. DOI: [10.1140/epjc/s10052-014-2988-y](https://doi.org/10.1140/epjc/s10052-014-2988-y). arXiv: [1401.3964](https://arxiv.org/abs/1401.3964) [hep-ph].
- [126] Torbj  rn Sj  strand, Stephen Mrenna, and Peter Z. Skands. “PYTHIA 6.4 Physics and Manual”. In: *JHEP* 05 (2006), p. 026. DOI: [10.1088/1126-6708/2006/05/026](https://doi.org/10.1088/1126-6708/2006/05/026). arXiv: [hep-ph/0603175](https://arxiv.org/abs/hep-ph/0603175).

- [127] Torbjörn Sjöstrand et al. “An Introduction to PYTHIA 8.2”. In: *Comput. Phys. Commun.* 191 (2015), pp. 159–177. DOI: [10.1016/j.cpc.2015.01.024](https://doi.org/10.1016/j.cpc.2015.01.024). arXiv: [1410.3012](https://arxiv.org/abs/1410.3012) [hep-ph].
- [128] Serguei Chatrchyan et al. “Measurement of the Underlying Event Activity at the LHC with $\sqrt{s} = 7$ TeV and Comparison with $\sqrt{s} = 0.9$ TeV”. In: *JHEP* 09 (2011), p. 109. DOI: [10.1007/JHEP09\(2011\)109](https://doi.org/10.1007/JHEP09(2011)109). arXiv: [1107.0330](https://arxiv.org/abs/1107.0330) [hep-ex].
- [129] Vardan Khachatryan et al. “Event generator tunes obtained from underlying event and multiparton scattering measurements”. In: *Eur. Phys. J. C* 76 (2016), p. 155. DOI: [10.1140/epjc/s10052-016-3988-x](https://doi.org/10.1140/epjc/s10052-016-3988-x). arXiv: [1512.00815](https://arxiv.org/abs/1512.00815) [hep-ex].
- [130] S. Agostinelli et al. “GEANT4: a simulation toolkit”. In: *Nucl. Instrum. Meth. A* 506 (2003), p. 250. DOI: [10.1016/S0168-9002\(03\)01368-8](https://doi.org/10.1016/S0168-9002(03)01368-8).
- [131] John Allison et al. “Geant4 developments and applications”. In: *IEEE Trans. Nucl. Sci.* 53 (2006), p. 270. DOI: [10.1109/TNS.2006.869826](https://doi.org/10.1109/TNS.2006.869826).
- [132] J. Neyman and E. S. Pearson. “On the Problem of the Most Efficient Tests of Statistical Hypotheses”. In: *Philosophical Transactions of the Royal Society of London A: Mathematical, Physical and Engineering Sciences* 231.694-706 (1933), p. 289. ISSN: 0264-3952. DOI: [10.1098/rsta.1933.0009](https://doi.org/10.1098/rsta.1933.0009).
- [133] C. H. Llewellyn Smith. “High-Energy Behavior and Gauge Symmetry”. In: *Phys. Lett. B* 46 (1973), p. 233. DOI: [10.1016/0370-2693\(73\)90692-8](https://doi.org/10.1016/0370-2693(73)90692-8). URL: [http://dx.doi.org/10.1016/0370-2693\(73\)90692-8](http://dx.doi.org/10.1016/0370-2693(73)90692-8).
- [134] Benjamin W. Lee, C. Quigg, and H. B. Thacker. “Weak Interactions at Very High-Energies: The Role of the Higgs Boson Mass”. In: *Phys. Rev. D* 16 (1977), p. 1519. DOI: [10.1103/PhysRevD.16.1519](https://doi.org/10.1103/PhysRevD.16.1519).
- [135] Vardan Khachatryan et al. “Constraints on the spin-parity and anomalous HVV couplings of the Higgs boson in proton collisions at 7 and 8 TeV”. In: *Phys. Rev. D* 92.1 (2015), p. 012004. DOI: [10.1103/PhysRevD.92.012004](https://doi.org/10.1103/PhysRevD.92.012004). arXiv: [1411.3441](https://arxiv.org/abs/1411.3441) [hep-ex].
- [136] *Measurements of Higgs boson properties from on-shell and off-shell production in the four-lepton final state*. Tech. rep. CMS-PAS-HIG-18-002. Geneva: CERN, 2018. URL: <https://cds.cern.ch/record/2638605>.
- [137] S. S. Wilks. “The Large-Sample Distribution of the Likelihood Ratio for Testing Composite Hypotheses”. In: *Annals Math. Statist.* 9.1 (1938), pp. 60–62. DOI: [10.1214/aoms/1177732360](https://doi.org/10.1214/aoms/1177732360).

- [138] M. Oreglia. “A Study of the Reactions $\psi' \rightarrow \gamma\gamma\psi$ ”. PhD thesis. SLAC, 1980. URL: <http://www-public.slac.stanford.edu/sciDoc/docMeta.aspx?slacPubNumber=slac-r-236.html>.
- [139] John Erthal Gaiser. “Charmonium Spectroscopy From Radiative Decays of the J/ψ and ψ' ”. PhD thesis. SLAC, 1982. URL: <http://www-public.slac.stanford.edu/sciDoc/docMeta.aspx?slacPubNumber=slac-r-255.html>.
- [140] Tomasz Skwarnicki. “A study of the radiative CASCADE transitions between the Upsilon-Prime and Upsilon resonances”. PhD thesis. Cracow, INP, 1986. URL: <http://www-library.desy.de/cgi-bin/showprep.pl?DESY-F31-86-02>.
- [141] Vardan Khachatryan et al. “Constraints on the Higgs boson width from off-shell production and decay to Z-boson pairs”. In: *Phys. Lett. B* 736 (2014), pp. 64–85. DOI: [10.1016/j.physletb.2014.06.077](https://doi.org/10.1016/j.physletb.2014.06.077). arXiv: [1405.3455](https://arxiv.org/abs/1405.3455) [hep-ex].

CURRICULUM VITAE

BIOGRAPHICAL AND CONTACT INFORMATION

Date and place of birth

05/15/1990

Istanbul, Turkey

Contact information

Johns Hopkins University

3701 San Martin Drive

Baltimore, MD 21218

Phone: +1 (585) 2058382

Email: ulascan90@gmail.com

EDUCATION

Degrees

Johns Hopkins University: 2013 – 2018

Physics M.A. (2015), Ph.D. (present)

→ Advisor:

Prof. Andrei V. Gritsan

University of Rochester: 2009 – 2013

Physics, Molecular Genetics B.S., Mathematics Minor (2013)

→ Research advisors:

Prof. Arie Bodek (Physics)

Prof. Douglas H. Turner and Prof. Ilyas Yildirim (Biochemistry)

Summer Courses

CERN-Fermilab HCP Summer School 2017, CERN (28 August – 6 September 2017).

RESEARCH EXPERIENCE

Projects

- Higgs boson properties and phenomenology (2013 – present):
 - Higgs properties measurements using MELA techniques (Matrix Element Likelihood Approach)
 - CMS ZZMatrixElement package development and maintenance
 - JHUGenerator event simulator contact person
 - Higgs properties phenomenology as part of the LHC Higgs Cross Working Group WG 1 and WG 2 activities
 - Mass-dependent NLO and NNLO K factors for Higgs boson gluon fusion production at $\sqrt{s} = 13$ TeV within the LHC Higgs Cross Section Working Group, WG 1 Off-shell Subgroup

- LHC run II Higgs properties (2015 – present):
 - Joint constraints on Higgs width and anomalous HVV couplings using decay and production information
 - Studies of associated production in off-shell Higgs production region in the four-lepton final state and joint treatment with on-shell Higgs production
 - Joint Higgs mass and width measurements in $H \rightarrow 4l$ using per-event mass errors and associated production
 - Constraints on anomalous Higgs boson couplings using VBF production with a Higgs boson decay to a tau lepton pair
 - Constraints on Higgs spin-parity properties using studies of associated production
 - Searches for high mass resonances in $4l$ and ZZ or $WW \rightarrow 2l2\nu$ decays using MELA techniques and simulation with interference $H(125)$, high mass resonance and continuum background
- CERN CMS tracker alignment (2015 – present):
 - Alignment of the strip and Phase-I pixel detectors
 - Alignment framework readiness for the Phase-I pixel detector installed early 2017
 - Alignment selection and data reweighting in the HipPy alignment algorithm
 - Dimuon ($Z, Y(1S), J/\psi \rightarrow \mu\mu$) mass/vertex constraints in the HipPy algorithm
 - Dimuon resonances in alignment validation
- LHC run I Higgs properties (2013 – 2016):
 - Lifetime of the Higgs boson from on-shell measurements
 - Constraints on the spin-parity and anomalous HVV couplings in $H \rightarrow 4l$, $H \rightarrow WW \rightarrow 2l2\nu$, and $VH \rightarrow b\bar{b}$
 - Constraints on the Higgs width using off-shell Higgs decay into Z or W boson pairs
 - Phenomenological Snowmass study on anomalous HVV couplings
- Fermilab MINERvA, NuMI Muon Neutrino Flux (2011 – 2013)
 - Determining muon neutrino flux from the NuMI beamline in the MINERvA experiment using the low ν method
 - Phenomenological studies on charged-current neutrino scattering events with low energy transfer (low ν method)
- RNA secondary structure prediction (2010 – 2012)
 - Studies on effective RNA free energy models for various RNA structural features such as hairpin loops
 - Analysis of 2x2 RNA tandem mismatches from nuclear magnetic resonance data, and the use of this data for the prediction of the free energy of tandem mismatches in the RNA secondary structure to target improvements in the

Selected Papers

CMS Collaboration, *Search for a new scalar resonance decaying to a pair of Z bosons in proton-proton collisions at $\sqrt{s} = 13$ TeV*, JHEP **6** 127 (2018).

CMS physics analysis CMS- HIG-17-012

[http://dx.doi.org/10.1007/JHEP06\(2018\)127](http://dx.doi.org/10.1007/JHEP06(2018)127), <https://arxiv.org/abs/1804.01939>

CMS Collaboration, *Measurements of properties of the Higgs boson in the four-lepton final state at $\sqrt{s} = 13$ TeV*, pre-print (Jun. 2018).

CMS physics analysis summary CMS-PAS-HIG-18-001

<http://cms-results.web.cern.ch/cms-results/public-results/preliminary-results/HIG-18-001/index.html>

CMS Collaboration, *Constraints on anomalous Higgs boson couplings using production and decay information in the four-lepton final state*, Phys. Lett. B **775** 1 (2017). (Editor)

CMS physics analysis CMS-HIG-17-011

<https://dx.doi.org/10.1016/j.physletb.2017.10.021>, <https://arxiv.org/abs/1707.00541>

CMS Collaboration, *Measurements of properties of the Higgs boson decaying into the four-lepton final state in pp collisions at $\sqrt{s} = 13$ TeV*, JHEP **11** 047 (2017).

CMS physics analysis CMS- HIG-16-041

[https://dx.doi.org/10.1007/JHEP11\(2017\)047](https://dx.doi.org/10.1007/JHEP11(2017)047), <https://arxiv.org/abs/1706.09936>

CMS Collaboration, *CMS Tracker Alignment Performance Results 2016*, pre-print (Jun. 2017).

CMS detector performance summary CMS-DP-2017-021

<https://cds.cern.ch/record/2273267>

LHC Higgs Cross Section Working Group, *Handbook of LHC Higgs Cross Sections: 4. Deciphering the Nature of the Higgs Sector*, CERN--2017--002-M, CERN Yellow Reports: Monographs vol. 2 (2017).

<https://doi.org/10.23731/CYRM-2017-002>, <https://arxiv.org/abs/1610.07922>

CMS Collaboration, *CMS Tracker Alignment Performance Results Summer 2016*, pre-print (Sep. 2016).

CMS detector performance summary CMS-DP-2016-063

<https://cds.cern.ch/record/2221746>

CMS Collaboration, *Search for Higgs boson off-shell production in proton-proton collisions at 7 and 8 TeV and derivation of constraints on its total decay width*, JHEP **09** 051 (2016).

CMS physics analysis CMS-HIG-14-032

[https://doi.org/10.1007/JHEP09\(2016\)051](https://doi.org/10.1007/JHEP09(2016)051), <http://arxiv.org/abs/1605.02329>

CMS Collaboration, *Combined search for anomalous pseudoscalar HVV couplings in VH production and H to VV decay*, Phys. Lett. B **759** 672 (2016).
CMS physics analysis CMS-HIG-16-035
<http://dx.doi.org/10.1016/j.physletb.2016.06.004>, <https://arxiv.org/abs/1602.04305>

CMS Collaboration, *Measurements of properties of the Higgs boson and search for an additional resonance in the four-lepton final state at $\sqrt{s} = 13$ TeV*, pre-print (Aug. 2016).
CMS physics analysis summary CMS-PAS-HIG-16-033
<http://cms-results.web.cern.ch/cms-results/public-results/preliminary-results/HIG-16-033/index.html>

CMS Collaboration, *Search for high mass Higgs to WW with fully leptonic decays using 2015 data*, pre-print, (Aug. 2016).
CMS physics analysis summary CMS-PAS-HIG-16-023
<http://cms-results.web.cern.ch/cms-results/public-results/preliminary-results/HIG-16-023/index.html>

CMS Collaboration, *Studies of Higgs boson production in the four-lepton final state at $\sqrt{s} = 13$ TeV*, pre-print (Mar. 2016).
CMS physics analysis summary CMS-PAS-HIG-15-004
<http://cms-results.web.cern.ch/cms-results/public-results/preliminary-results/HIG-15-004/index.html>

CMS Collaboration, *Tracker Alignment Plots for LHCC*, pre-print (Dec. 2015).
CMS detector performance summary CMS-DP-2015-059
<https://cds.cern.ch/record/2115430>

CMS Collaboration, *Limits on the Higgs boson lifetime and width from its decay to four charged leptons*, Phys. Rev. D **92** 7, 072010 (2015), (Editor)
CMS physics analysis CMS-HIG-14-036
<https://doi.org/10.1103/PhysRevD.92.072010>, <http://arxiv.org/abs/1507.06656>

CMS Collaboration, *Alignment of the CMS Tracking-Detector with First 2015 Cosmic-Ray and Collision Data*, pre-print (Aug. 2015).
CMS detector performance summary CMS-DP-2015-029
<http://cds.cern.ch/record/2041841>

CMS Collaboration, *Constraints on the spin-parity and anomalous HVV couplings of the Higgs boson in proton collisions at 7 and 8 TeV*, Phys. Rev. D **92** 1, 012004 (2015).
CMS physics analysis CMS-HIG-14-018
<http://dx.doi.org/10.1103/PhysRevD.92.012004>, <http://arxiv.org/abs/1411.3441>

CMS Collaboration, *Constraints on the Higgs boson width from off-shell production and decay to Z-boson pairs*, Phys. Lett. B **736** 64 (2014).
 CMS physics analysis CMS-HIG-14-002
<http://dx.doi.org/10.1016/j.physletb.2014.06.077>, <http://arxiv.org/abs/1405.3455>

U. Sarica, B.S. Thesis, University of Rochester, Rochester (2013).
http://www.pas.rochester.edu/~usarica/Revised%20Thesis/usarica_thesis_archive.zip

A. Bodek, U. Sarica, K. S. Kuzmin, V. A. Naumov. *Extraction of neutrino flux with the low ν method at MiniBooNE energies*. AIP Conf. Proc. **1560**, 193 (2013).
<http://dx.doi.org/10.1063/1.4826751>

A. Bodek, U. Sarica, D. Naples, L. Ren. *Methods to Determine Neutrino Flux at Low Energies: Investigation of the Low ν Method*. Eur. Phys. J. C **72**, 1973 (2012).
<http://dx.doi.org/10.1140/epjc/s10052-012-1973-6> <http://arxiv.org/abs/1201.3025>

Conferences

- International Workshop on the CKM Unitarity Triangle 2018 (17-21 September 2018):
Higgs anomalous couplings, FCNC and LFV decays.
- Phenomenology Symposium 2017 (Pheno 2017) (8-10 May 2017):
Tools for Higgs boson properties with the JHUGen / MELA framework.
- ICHEP 2016 (3-10 August 2016):
CMS H(125) mass, width, tensor structure, and couplings measurements.
- Higgs Hunting 2016 (31 August – 2 September 2016):
(YSF) CMS H(125) width and lifetime measurements in the 4l final state.
- APS April Meeting 2014, Baltimore, Maryland (11– 14 April 2015):
Limits on the Higgs boson lifetime and width from its decay to four charged leptons.
- Rochester Academy of Sciences 39th Annual Fall Scientific Paper Session, St. John Fisher College, Rochester, New York (10 November 2012):
Measuring Neutrino Flux at Low Energies: The Low ν Method.
- Fermilab Graduate Student Association, New Perspectives 2012, FNAL, Batavia, IL (14 June 2012): Methods to Determine Neutrino Flux at Low Energies: The Low ν Method.
- APS April Meeting 2012, Atlanta, Georgia (31 March – 3 April 2012):

Methods to Determine Neutrino Flux at Low Energies: The Low ν Method.

- National Conference for Undergraduate Research 2012, Weber State University, Ogden, Utah (29 – 31 March 2012):
Methods to Determine Neutrino Flux at Low Energies: The Low ν Method.

Selected Presentations

CMS Higgs Physics Analysis Group pre-approval of HIG-18-002, *Measurements of the Higgs boson properties from on-shell and off-shell production in the four-lepton final state* (29 May 2018)

LHC Higgs Cross Section WG 1, Off-shell subgroup, *CMS analysis approaches to gluon fusion K factors* (22 Feb. 2018)

LBNL Research Progress Meeting (invited talk), *Measurements of mass, width, lifetime and anomalous couplings of the $H(125)$ boson* (16 Nov. 2017)

CMS Tracker Detector Performance Group, *Updates from tracker alignment* (25 Jul. 2017)

CMS Tracker Detector Performance Group, *Recent tracker alignment activities* (18 Jul. 2017)

CMS Higgs Physics Analysis Group HIG-17-011 combination approval, *Constraints on anomalous Higgs couplings in production and decay $H \rightarrow 4l$: Combination of HIG-14-018, HIG-16-033, and HIG-17-011* (11 Apr. 2017)

CMS Central Physics Approvals Moriond EWK approval of HIG-17-011, *Constraints on anomalous Higgs couplings in production and decay $H \rightarrow 4l$* (13 Mar. 2017)

CMS Higgs Combination Group presentation on HIG-17-011 combination pre-approval, *Run I and Run II combination of anomalous couplings of the Higgs boson using onshell $H \rightarrow 4l$ events* (8 Mar. 2017)

CMS Higgs Combination Group, *Theory Uncertainties in $H \rightarrow ZZ$* (17 Jan. 2017)

CMS Alignment Calibration and Database, *2016 Legacy Tracker Alignment: Final candidates* (12 Dec. 2016)

CMS Tracker Alignment public performance plots approval, *EOY Alignment Plots for the $Z \rightarrow \mu\mu$ Validation* (20 Jan. 2016)

CMS Higgs Physics Analysis Group approval of HIG-16-033, *New results on the study of Higgs boson production in the four-lepton final state at $\sqrt{s} = 13$ TeV* (7 Apr. 2015)

CMS Higgs Physics Analysis Group approval of HIG-14-036, *Limits on the Higgs boson lifetime and width from its decay to four charged leptons* (7 Apr. 2015)

CMS Higgs Physics Analysis Group pre-approval of HIG-14-036, *Bounds on the Higgs boson lifetime with $H \rightarrow 4l$ events* (12 Dec. 2014)

CMS Higgs Physics Analysis Group status report on HIG-14-002, *Updates on the Higgs Width in $H \rightarrow ZZ$* (22 Apr. 2014)

AWARDS AND AFFILIATIONS

Awards, Scholarships and Honors

Phenomenology Symposium 2017 PITT-PAC Travel Award (May 2017)
Johns Hopkins University Gardner Fellowship (Spring, Summer 2015)
Johns Hopkins University Owen Scholars Award (2013-2016)
Magna cum laude from the University of Rochester (May 2013)
University of Rochester Biological Physics Certificate (May 2013)
Stoddard Thesis Prize Honorary Mention (May 2013)
University of Rochester Rush Rhees Scholarship (2009-2013)
University of Rochester Dean's Scholarship (2009-2013)
SPS Undergraduate Presentation Certificate, APS April 2012 Meeting (April 2012)
University of Rochester Undergraduate Research Travel Grant (March 2012)
DPF Travel Grant for APS April 2012 Meeting (March 2012)
FPD Undergraduate Basic Travel Award for APS April 2012 Meeting (March 2012)
Phi Beta Kappa Iota Chapter 2010 Iota Book Award (November 2010)
CRC Press 2010 Freshman Chemistry Achievement Award (September 2010)

Organization Memberships

The American Physical Society, DPF student member (USA, 2009)
Phi Beta Kappa Society (USA, 2013)
Sigma Pi Sigma Physics Honor Society (USA, 2011)
Golden Key Honor Society (USA, 2011)
National Society of Collegiate Scholars (USA, 2010)
National Society of Physics Students (USA, 2009 – 2013)
Society of Physics Students University of Rochester Chapter (USA, 2009 – 2013)

TEACHING EXPERIENCE

Johns Hopkins University, USA

General Physics I for Physical Science Majors Conference (Spring 2018)
Electromagnetic Theory II (Fall 2015)
General Physics II for Physical Science Majors Conference (Fall 2014)
General Physics Laboratory II (Fall 2014)
General Physics II for Biological Science Majors Conference (Spring 2014)
Electricity and Magnetism Laboratory (Spring 2014)

General Physics I for Biological Science Majors Conference (Fall 2013)
General Physics Laboratory I (Fall 2013)

University of Rochester, USA

University of Rochester SPS tutor, PHY 122/142 Intro. E&M (Fall 2009)

Bosphorus University, Turkey

Augmented Physics, Feza Gursey Institute (12-23 July 2009)

LITERACY

Programming: C++/C, Fortran, Python, Perl, Unix, Ubuntu, HTTP

Software: ROOT, Mathematica, Microsoft Office

Literary Languages: Turkish (Native), English, German